



**Politecnico
di Torino**

POLITECNICO DI TORINO

Master's degree in Communications and Computer Networks
Engineering

A.y. 2022/2023

April 2023 Graduation Session

Vibration detection using low cost optical sensing systems for geological applications

Supervisor

Roberto Gaudino

Co-supervisors

Giuseppe Rizzelli Martella

Saverio Pellegrini

Candidate

Marco Lacidogna

Abstract

The master Thesis deals with Optical Fiber Sensing for early warning of life-threatening events such as avalanches and debris flows in mountain scenarios. In addition, the developed algorithm aims to improve the detection of dangerous geotechnical events by means of reliable and spatially continuous monitoring operations of the mechanical vibrations in the proximity of the optical sensors. In the developed system (Fig. 1), the probe light was conveyed by an optical source, the sensors were represented by the optical fibers, and their polarization state was continuously acquired by a polarimeter device.

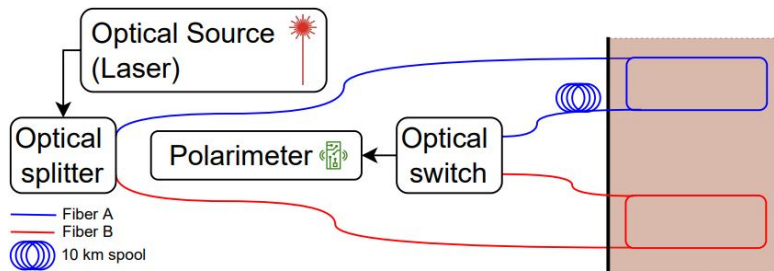


Figure 1: 2-fiber sensors experimental setup

The intensity of the sensed vibrations was monitored by analyzing the incoming light polarization state variations on the Poincaré space through the Stokes parameters. In particular, the angular speed of the State Of Polarization (SOP) inside the fibers was actually evaluated and monitored to estimate the mechanical vibrations along the optical paths. Consequently, the higher the angular speed, the more the SOP changed inside the fiber and the more intense the sensed event was. In order to achieve the desired sensing results, due to the unfeasible events generated in a real mountain environment, a reduced scale downhill gully model was built (Fig. 2), where very reliable and in scale events were generated and studied.

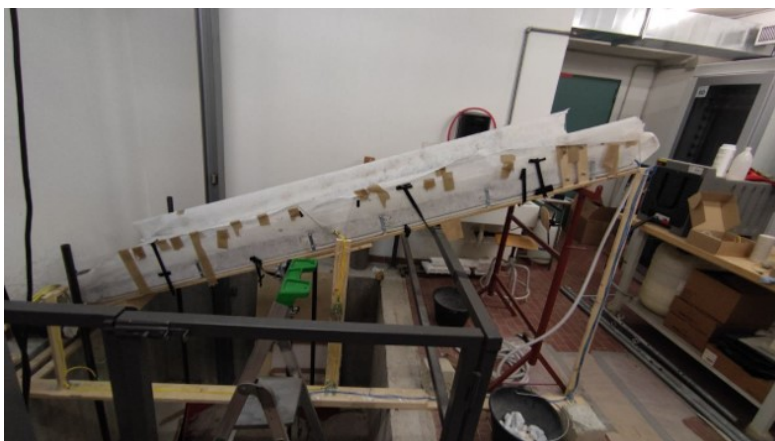


Figure 2: Mountain gully model

The main target of the work is to acquire the light information coming from multiple fibers at the same time, and to keep the costs of the monitoring system feasibly low. To reach this target, an inexpensive optical switch was implemented in the experimental setup.

The device, inserted after the optical source, allowed to monitor different measurements by periodically switching the optical paths and it aimed to minimize the probability of false alarms provoked by non-dangerous vibrations (e.g: animals walking in the area, tree falling, etc.). During the Thesis, two working fields were proposed. The first dealt with the post-processing of the acquired data, pointing to optimize the processing parameters and to best characterize the measured polarization traces. After that, a real-time algorithm was developed following the results obtained from the offline method (post-processing). In particular, a threatening event was detected when at least two fibers sensed the same strong vibrations, and a resulting alarm message was displayed. The target of the real-time algorithm was to monitor a threatened mountain gully and, in case of dangerous detection, to generate an extremely rapid warning message in order to allow a prompt reaction of the users. In addition, thanks to the displacement of two or more sensors, when an alert message was returned, the algorithm was able to assess a rapid evaluation of the ongoing event dynamics, enabling a roughly spatial mapping of the monitored area state along the fiber length. This operation was performed by computing the cross correlation between the fibers polarization traces and the outcomes returned a rough estimation of the time taken by the event to roll down between the two fibers and its resulting velocity. In Figure 3 a first example of the algorithm outcomes is illustrated.

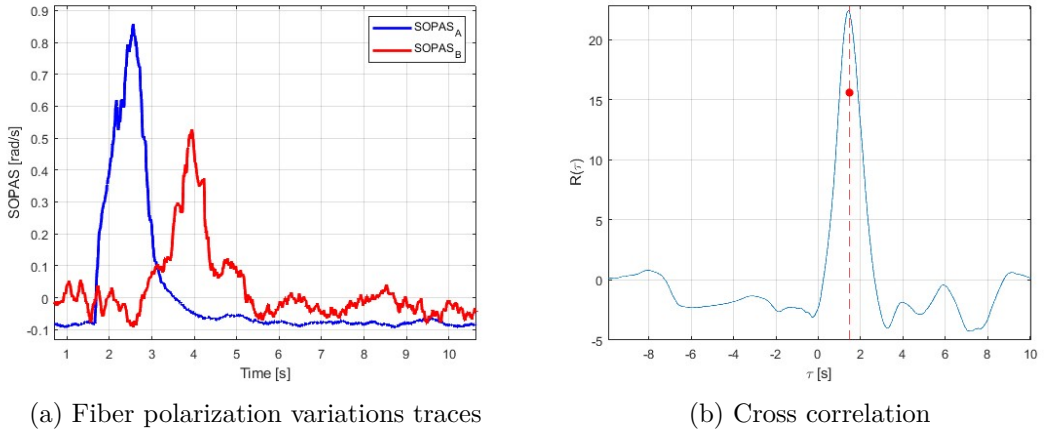


Figure 3: Real-time Matlab outcomes

In particular, in Figure 3 (a) are reported the traces of the SOP angular speeds along the fibers, while in Figure 3 (b) is pictured their cross correlation curve. The red dot in the latter represents the centroid (or center of mass) of the correlation main peak, which defines the event rolling delay sensed on the probe fiber.

To conclude, the developed Thesis achieved both the desired targets of:

- cost-effectiveness, since the implementation of the optical switch allowed to share the same hardware components between the different sensors;
- reliability and sensibility, since the employed system was able to minimize the false alarm probability and to sense with accuracy any kind of vibrations induced on the

reduced scale structure.

Acknowledgements

Contents

List of Figures	VII
1 Introduction	1
1.1 Application targets of this Thesis and previous works	3
1.2 Fiber Polarization	6
1.3 Stokes parameters and SOPAS	9
1.4 SMF Birefringence	11
1.5 Organization of the Thesis	13
2 Experimental Setup based on an Optical Switch	15
2.1 Employed equipment and mountain model	15
2.2 Description of the used Optical Switch	23
2.3 First Experiments with the Optical Switch	25
2.4 Optical Switch Impairments	28
2.5 Solutions employed in post-processing	31
2.5.1 NI 9269 breadboard	32
2.5.2 Arbitrary Function Generator	32
2.6 Solutions employed in Real-Time	35
2.6.1 Programmable Function Generator	35
2.6.2 Electrical Operational Amplifiers	36
2.7 Summary: post-processing and real-time setup	37
3 Initial Measurements with elaboration in post-processing	41
3.1 Digital Signal Processing and selection of the parameters	41
3.2 Two-Fiber Detection System	52
3.2.1 New Downhill Model and obtained results	54
3.3 4-Fibers Implementation	60
3.4 Summary and conclusions	62
4 Real-Time implementation and related Measurements	63
4.1 Algorithm employed and differences with the offline method	63
4.2 4-fibers experiments	70
4.3 RT evaluations with the developed GUI	71

5	Conclusions and future developments	77
A	PP SOPAS evaluation	81
B	RT SOPAS evaluation	83
C	Real Time Algorithm: Matlab Script	85

List of Figures

1	2-fiber sensors experimental setup	I
2	Mountain gully model	I
3	Real-time Matlab outcomes	II
1.1	General OFSs architecture	1
1.2	Possible OFSs topology	2
1.3	Rovina di Cancia, example of a risky mountain gully (Picture taken from [1])	4
1.4	Events detection map (Picture taken from [13])	5
1.5	Electric field components of a linear polarization along \hat{z}	7
1.6	Linear polarization	8
1.7	Circular polarization	8
1.8	Elliptical polarization	9
1.9	a) Elliptical polarization; b) Poincaré Sphere; (Picture taken from [18]) . .	11
1.10	Differential group delay induced by the birefringence (Picture taken from [7])	12
2.1	System block scheme	15
2.2	Optical Laser Source	16
2.3	Mountain downhill model	18
2.4	General fibers arrangement	18
2.5	Simulated Dangerous Events	20
2.6	PM1000	21
2.7	PM1000 user interface	22
2.8	User interface plots	22
2.9	Optical Switch ports	23
2.10	Optical Switch block scheme	24
2.12	Poincaré sphere, only one fiber stressed	26
2.12	Poincaré sphere, only one fiber stressed	27
2.13	SOPAS and power, oscilloscope view	28
2.14	Single rock spectrogram (Picture taken from [13])	29
2.15	First optical switch impairments	30
2.16	NI 9401 connector and driving Pins	31
2.17	Front view of a Power Supply single channel (figure taken from [])	31
2.18	NI-9269	32
2.19	Square waves working principle	33

2.20	Parameters set to generate the square waves	34
2.21	New optical switch setup	34
2.22	The Arbitrary Function Generator (figure taken from [])	35
2.23	Instrument Control user interface	36
2.24	Voltage follower operational amplifier	36
2.25	Optical switch op.amp.block diagram	37
2.26	Operational Amplifiers	38
2.27	Final Post Processing in Setup	38
2.28	Final Real Time Setup	39
2.29	4-fibers experimental setup	40
3.1	Post processing block scheme	42
3.2	Stokes extrapolation	43
3.3	Derivative of the power and correct measurements periods	44
3.4	Stokes parameters after peaks removal	44
3.5	Processing steps	45
3.5	Processing steps	46
3.6	Evolution of the Stokes parameters S_1, S_2 and S_3	46
3.7	FIR filter Scheme	48
3.8	T_{mov} impact on the normalized SOPAS evolution	49
3.9	Example of a non-dangerous event, $T_{mov}=0.1 s$	50
3.10	Post processing results, $T_{mov} = 0.1 s$	50
3.11	T3 events detection maps (Pictures taken from [13])	52
3.12	Events SOPAS: Z1s and Z1i, $T_{mov}=0.5 s$	53
3.13	SOPAS evolution on single fibers: $T_{mov}=0.5 s$	54
3.14	New downhill Model	55
3.15	SOPAS trends, $T_{mov}=1 s$	56
3.16	SOPAS evolution, $T_{mov}=0.5 s$	57
3.17	SOPAS evolution, $T_{mov}=0.5 s$	57
3.18	Fibers noise floor, $T_{mov}=0.5 s$	58
3.19	Simplified setup of the two-fibers system	58
3.20	Offline experiments: $\omega_{th}=0.08 rad/s$, $T_{mov}=0.5 s$	59
3.21	4-fibers SOPAS evolution $T_{mov}=0.2 s$	60
3.22	Normalized cross correlations, $T_{mov}=0.2 s$	61
3.22	Normalized cross correlations, $T_{mov}=0.2 s$	61
4.1	Real-time block scheme	64
4.2	Experiment on Tm and $Z3i$ fibers, $T_{mov}=0.2 s$	65
4.3	Experiment on $Z3s$ and $Z3i$ fibers, $T_{mov}=0.2 s$	65
4.4	T_{sw} with and without RT plots	66
4.5	Final memory employment	67
4.6	Stokes parameters memory management	69
4.7	A - RT 4-fibers SOPAS plot, $T_{sw}=10 ms$	70
4.8	B - RT 4-fibers SOPAS plot, $T_{sw}=10 ms$	71
4.9	Graphic user interface	72

4.10	Experiment A - GUI and RT plots	74
4.11	Experiment B - GUI and RT plots	75
4.12	Experiment C - GUI and RT plots	75
5.1	GUI and RT plots	77
5.2	Cross correlation curves and centroids between SOPAS on Tm and $Z3i$ for five SR events	78
5.3	Assumed real SOPAS trends	79

Chapter 1

Introduction

In the last decades, optical fibers established as an essential component in the telecommunication industry, becoming the backbone of the wired communication environment. This technology achieves features (like electromagnetic (EM) immunity, high data transfer speeds and low loss, to name a very few) that the previous copper wired systems were not able to provide. For those reasons, in recent years, optical fibers have been considered with growing interest as suitable also for environmental sensing, to detect mechanical stresses or vibrations happening in metropolitan or submarine scenarios, where they are already displaced, as well as in a mountain one ([10]). Being this the main topic of the Thesis, a brief description of the Optical Fiber Sensors (OFSs) state of art is reported, by highlighting the main advantages of the new technology and the similarities with the actual system applied in the following work. By definition, an *optical fiber sensor* is a device that make use of light to convey the information that it senses [8]. A typical OFSs architecture is illustrated in Figure 1.1.

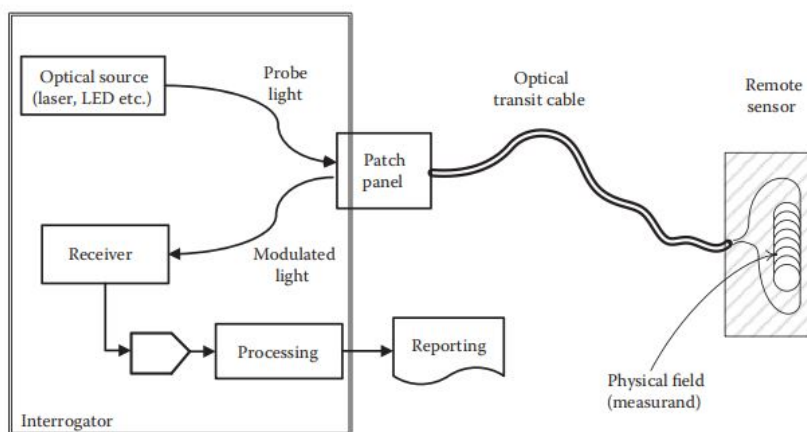


Figure 1.1: General OFSs architecture

The illustrated system consists in an interrogator, which conveyed the probe light into the optical transit cable and processed the modulated information returned back from the monitored site, and in a remote sensor, which modulates the input signal accordingly to the observed measurand. The interrogator is the intelligent part of the setup and it consisted of an optical source which generates the probe light and of a receiver that acquires the information modulated by the sensor, and transforms the optical signal into an electrical one in order to process the results. Moreover, also a patch panel is reported, it is just a connection block which separates the conveyed light from the modulated one. Given the wide variety of light measurands (or attributes) present in nature, including intensity, polarization, phase, optical spectrum and more, OFSs are highly versatile systems and have been employed in many applications, from industrial sensing to the military or biomedical fields. Indeed, the ability to control and monitor distributed optical sensors working in hostile locations from a harmless and distant site, allows to perform sensing operations also in dangerous conditions (e.g. high temperatures sites or submarine sensing). Furthermore, one other research field of the OFSs technology is the possibility of complementing regular telecommunication Network with the new sensing capabilities [3], allowing to share the fibers to multiple purposes and enabling huge benefits in terms of sensing employment and costs. The reported OFSs structure is not the only available, but rather different topology has been developed in order to make use of multiple sensors sharing the same interrogator and to enhance the cost-effectiveness of the setup. Consequently, Figure 1.2 describes the employed OFSs topology.

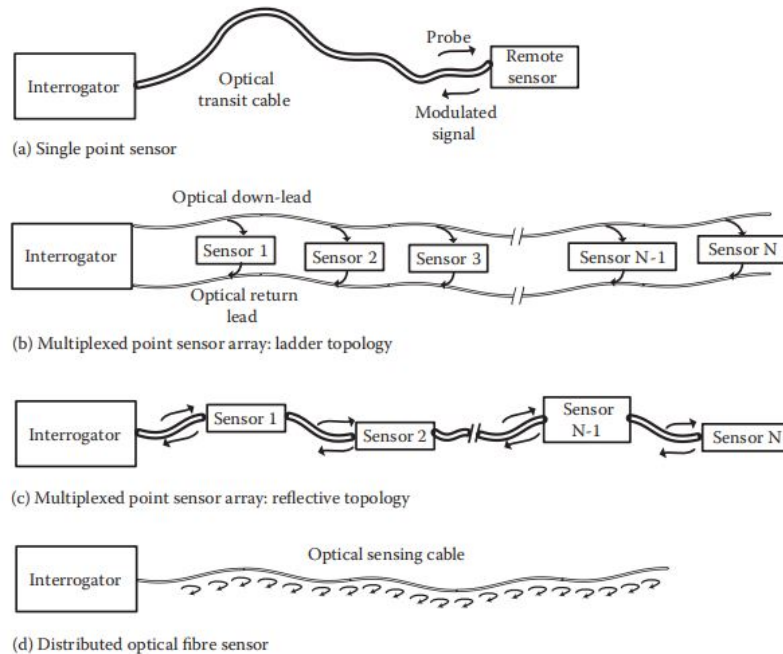


Figure 1.2: Possible OFSs topology

- Single point sensor (Fig.1.2 (a)): this arrangement is the same described in Figure 1.1 and it based on one sensor only. The configuration share one fiber to convey and return back the information between the interrogator and the sensor, therefore it is not able to determine the spatial distribution of the measurand along the monitored fiber, but it is able only to detect if some unwanted or dangerous events are happening.
- Multiplexed point sensor array (Fig.1.2 (b,c)): the system is based on the employment of multiple sensors on a single transit cable. In particular, the multiplexed topology can be arranged in a ladder (Fig.1.2 (b)) or in a reflective (Fig.1.2 (c)) patterns. The ladder topology is characterized by a fiber that transmits the probe light past each of the sensors in turn, and by a return fiber that collects the signal modulated from each of them. While, in the latter, the probe light passes the sensors and a small portion of it is reflected back towards the interrogator with the measurand information. The advantage of this pattern is the possibility to use multiple sensors, therefore it allows to determine a discrete spatial profile of the measurand along the transit cable and its accuracy strongly depends on the amount of sensors employed. For this reason, unless a huge amount of sensors is used, they are less effective than the distributed topology.
- Distributed optical fiber sensor (Fig.1.1 (d)): this arrangement turns out to be the best solution to map a spatial profile of the measurand, because it is like having a multiplexed topology with an infinite number of sensors. In other words, it allows to obtain through a one-dimensional medium a continuous mapping of the measurands along the entire probe fiber. The main advantage of this pattern is the possibility to sense each point of the optical wire, therefore it's able to construct a spatial profile of the sensed parameter as a function of the distance and to localise events positions. However this patter is highly cost-demanding, condition that goes in contrast with the Thesis purposes.

In the developed work, the OFSs setup architecture aimed to reproduce an enhanced version of the single point topology (Fig.1.2 (a)), with the difference that multiple sensors have been employed and that the sensors does not have a common down-lead and return-lead fibers. Therefore, the conveyed light was distributed independently to the different sensors, and an optical switch was inserted after the optical source to selectively connect the modulated light back to the interrogator. Nevertheless, a more detailed analysis of the system setup is provided in Chapter 2.

1.1 Application targets of this Thesis and previous works

Previous studies on the OFSs theme [2] demonstrated that, in recent years, the optical sensing operations turned out to be highly suitable for the detection of mechanical stresses as seismic events and earthquakes over terrestrial or submarine links. Following this influence, the developed Thesis aimed to employ optical fibers to monitor mechanical

vibrations and strains in a mountain scenarios. The presented environment is highly subjected to dangerous events like landslides, avalanches and debris flows, which represent a constant and unpredictable danger for people and infrastructure, jeopardizing many lives.

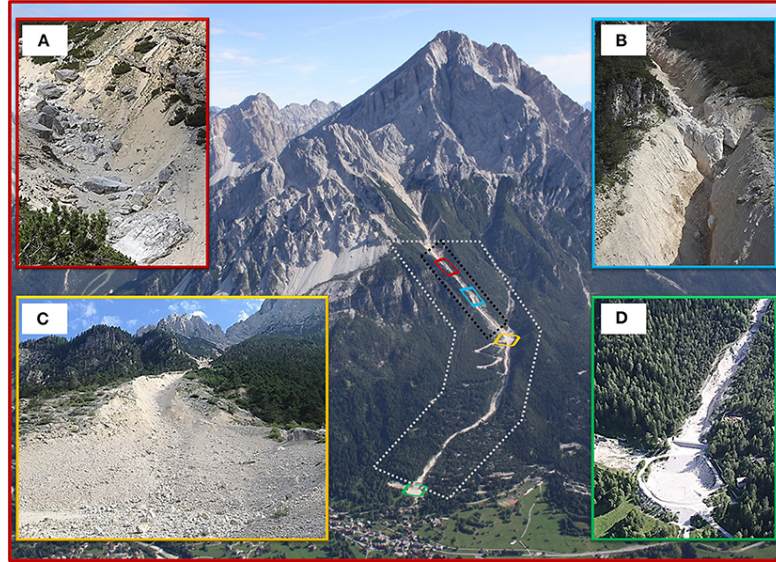


Figure 1.3: Rovina di Cancia, example of a risky mountain gully (Picture taken from [1])

For sake of clarity, in Figure 1.3 is illustrated a 2 *km* length debris-flow channel in the North-eastern Alps (Venetian Dolomites), which dangerously ended near a small village. This type of scenarios perfectly represents the sites that the Thesis purposes aimed to monitor. It is also visible that some preventive actions were already present, like the basin at the end of the slide (Fig.1.3 (d)), however, these solutions (as the rockfalls barrier) are displaced in fixed positions of the gully and do not allow information about the ongoing events because employed for protection rather than sensing.

Therefore, the main purpose of the work was to present a real-time early warning system based on OFSs able to capture life-threatening events and to signal them through an acoustic or a visible alarm (e.g. a semaphore) in order to allow a prompt action on the in danger sites. In this way, for instance, a village can be in a tamey manner evacuated as well as a road can be closed to the traffic. Indeed, due to the destructive events high velocities, forces and runout distances, the developed system had to acquire and process the measurements obtained from the optical sensors as fast as possible in order to dispatch quickly a warning message. To achieve the desired results, the target of the performed analysis was to sense the state of polarization (SOP) inside the optical transit cable and to monitor its variations along the fibers in order to estimate the ongoing mechanical vibrations intensity. In addition, one big advantage of the presented sensing system is the possibility to monitor vast mountain areas by easy-reach locations situated several *km* from the processed location.

As matter of fact, a Thesis about the OFSs based on polarization sensing and applied in a mountain scenario was already published by the Politecnico di Torino [13]. In particular, in the work, it was tested a solution highly similar with the single point sensor topology illustrated in Figure 1.2 (a), indeed, the system employed was based on a Laser source, on optical transit cables and on one Polarimeter. The latter is a device able to receive the incoming light and to monitor continuously its polarization state. Moreover, by converting the acquired optical signal into an electrical one, the instrument allows also to apply further post processing operations on the measurements obtained. Finally, the experimental simulations were tested on different fibers, buried at various depths on a reduced scale model of a mountain gully, due to unfeasible tests on real mountain scenario. In particular, to evaluate the system performances, multiple events of different intensities were tested on the just reported experimental slide model. The main operation of the developed algorithm was to characterize the generated events, therefore, an occurrence was classified as dangerous or not depending on a threshold value, which depended as well on the incurred ground vibrations and on some algorithm parameters. Consequently, the goal of the previous work was to propose a solution based on the optical fiber sensing technology, with the intention of developing an algorithm able to guarantee a correct and quick generation of an alarm message when a dangerous event was detected. Therefore, an in depth study of the different detection conditions with respect to the algorithm parameters was performed and reported in Figure 1.4.

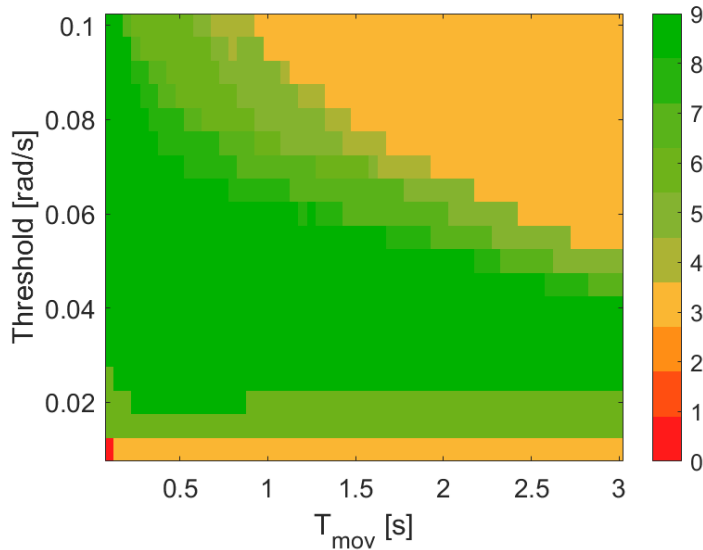


Figure 1.4: Events detection map (Picture taken from [13])

More in details, in the Figure is reported a colored map that characterizes the detection performances of the developed system on the reduced scale model previously cited. The colorbar on the right shows the amount of correct detection obtained after the experiments and defines the algorithm performances from the most reliable (top) to the most unsafe

(bottom). The green area represents the algorithm conditions that always returned a correct detection of the dangerous events, independently from their intensity. Instead, in the faded areas, only the events with the highest energy were detected, therefore some misses occurred and the algorithm reliability decreases too. Overall, due to the large size of the green area in the reported map, the analysis done in the previous work proved the good functioning of the OFSs technology in the mountain scenario with good performances and low costs. Finally, the employment of a low sampling frequencies in the evaluation of the results allowed to greatly reduce the data processed and stored, which is a key feature of endless monitoring systems that runs 24/7.

Thus, following this results, the goal of this Thesis was to enhance them by introducing in the just described system an optical switch able to selectively monitor different probe fibers and to reproduce a quasi-distributed sensors architecture. This kind of solution tried to reach the same simplicity of use of the previous configuration but with reduced costs with respect to the totally distributed sensing pattern. The employment of a limited number of sensors had the purpose of generating a discrete rough spatial profile of the events. In particular, it was demonstrated that, with just two fibers arranged at different section of the model, the developed algorithm was able to provide an approximated estimate of the ongoing occurrence velocity. Consequently, the system enhancement aimed to increase the dangerous events correct detection reliability and to improve the cost-effectiveness of the OFSs architecture by reusing the same hardware technology of the initial work. Lastly, a Graphic User Interface (GUI) was produced in order to provide to the future users an application able to easily manage and control the performed detection algorithm and the resulting performances.

1.2 Fiber Polarization

As it was previously described, in this Thesis, and in many other researches [2], polarization sensing through OFSs had a key role in the observation and classification of geotechnical events. Indeed, the polarization state of the light travelling in optical cables is strongly influenced by external disturbances due to the birefringence effects. Consequently, in this introductory sections, a brief description of waves polarization and of birefringence phenomenon are provided.

The electromagnetic waves such as visible light and microwaves consist of an Electric (\vec{E}) and a Magnetic (\vec{H}) fields oscillating perpendicular each other along a propagation direction (\hat{z}) orthogonal to both.

Polarization is a natural property of the electromagnetic waves and it represents the plane figure described by the tip of the Electric field vector in time [15]. In other words, it describes the way the Electric field is oriented in time, and consequently, Figure 1.5 shows a clear representation of the \vec{E} field components along the propagation direction. In particular, given the phasor representation of the Electric and Magnetic fields Equations in 1.1 and 1.2 it was possible to describe any polarization state inside a SMF:

$$\vec{E} = (\hat{x}E_1 + \hat{y}E_2e^{j\phi})e^{-jkz} \quad (1.1)$$

and

$$\vec{H} = \frac{1}{\eta}(-\hat{x}E_2e^{j\phi} + \hat{y}E_1)e^{-jkz} \quad (1.2)$$

where E_1 and E_2 are the amplitude of the Electric field components on the xy plane, identified as E_x and E_y , k is the wavenumber, η is the intrinsic impedance of the medium and ω is the waves angular frequency. In particular, the phase difference between the

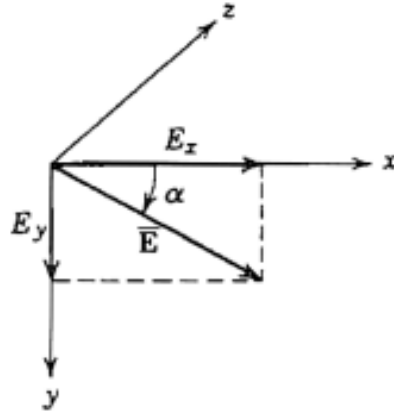


Figure 1.5: Electric field components of a linear polarization along \hat{z}

Electric fields components (called ϕ) and their relative amplitudes define the type of figure described by the instantaneous field.

Accordingly, three different types of polarization are defined:

1. Linear polarization;

This kind of polarization is obtained when one of the two fields components is zero ($E_x=0$ or $E_y=0$) or when $\phi=0$, therefore when the x-direction and the y-direction Electric fields share the same phases. The resulting polarization trends are illustrated in Figure 1.6 (all the Pictures inserted in this section have been taken from [9]).

In particular, the Electric field position oscillates with angular frequency ω on a fixed straight line (in the xy plane) along the propagation direction, and since \vec{E} maintains its direction in space, this polarization is called *linear*. Moreover, in the latter configuration (in-phase fields), the angle of the linear oscillation towards the x-axis is that of Equation 1.3:

$$\alpha = \tan^{-1} \left(\frac{E_y}{E_x} \right) = \tan^{-1} \left(\frac{E_2}{E_1} \right) \quad (1.3)$$

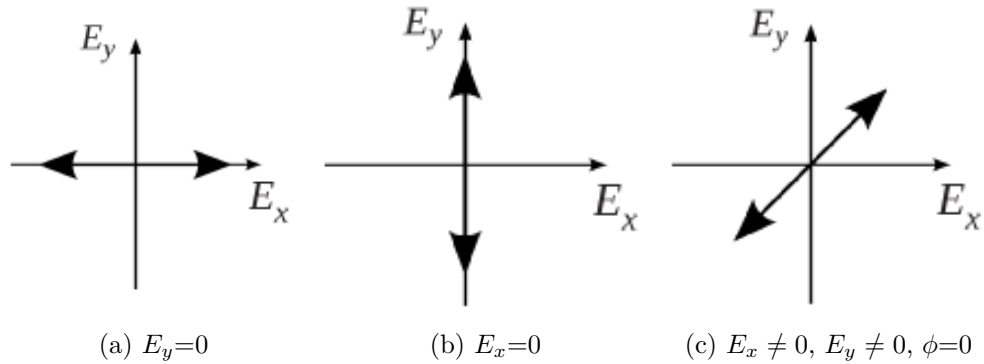


Figure 1.6: Linear polarization

2. Circular polarization;

This configuration is a special elliptical polarization state because obtained when the fields phase difference ϕ is equal to $\pm \pi/2$ and when the amplitudes E_1 and E_2 are equal. In particular, by referring to Equation 1.1, the \vec{E} vector then becomes:

$$\vec{E} = (\hat{x} \pm j\hat{y})E_1 e^{-jkz} \quad (1.4)$$

Notice that, in this case, the instantaneous angle α with respect to the x-axis is defined as:

$$\alpha = \tan^{-1} \left(\frac{E_y(z,t)}{E_x(z,t)} \right) = \tan^{-1} \left(\mp \frac{\sin(\omega t - kz)}{\cos(\omega t - kz)} \right) = \mp (\omega t - kz) \quad (1.5)$$

the \vec{E} vector thus is not fixed as in the linear case and rotates in space with angular velocity $\alpha = \mp \omega t$. The obtained polarization plane figures are illustrated in Figure 1.7.

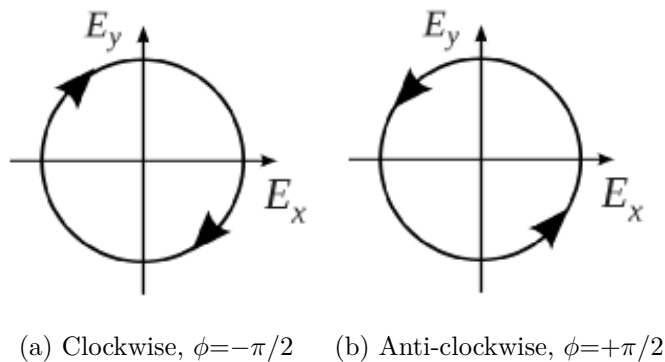


Figure 1.7: Circular polarization

3. Elliptical polarization;

In general, an electromagnetic wave is described by this type of polarization, because the elliptical configuration allows to depict any polarization state. This pattern is obtained when $E_1 \neq E_2$ or when $E_1 = E_2$ but ϕ different from 0 or $\pm \pi/2$. Indeed, all the polarization that are not linear or circular are as a consequence elliptical. Finally, the electric fields instantaneous components can be described (assuming $z=0$) as:

$$E_x = E_1 \cos \omega t \tag{1.6}$$

$$E_y = E_2 \cos (\omega t + \phi) \tag{1.7}$$

and the plane figure described by this last configuration is an ellipse and it is observed in figure 1.8

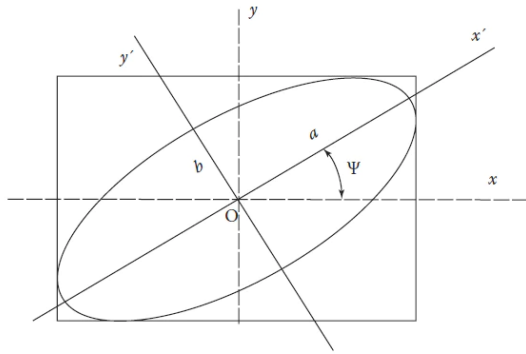


Figure 1.8: Elliptical polarization

where ψ is the angle between the ellipse major axis and the x-axis and represents the ellipse orientation angle.

To conclude, any polarization state can be expressed as a linear combination of two orthogonal polarization, with linear or circular bases.

1.3 Stokes parameters and SOPAS

Following the notations described in Section 1.2, the elliptical polarization could be used to describe any kind of polarization state, including the linear and the circular ones. However, the State Of Polarization (SOP) of a lightwave cannot be directly measured [14], due to both the light high frequency nature and to the partially polarized state in most of the waves [6]. For this reason, the SOP of a light beam was described in an easily accessible way and by means of the vector \vec{S} [4], which consists of four measurable quantities called Stokes parameters. Consequently, the \vec{S} vector of a completely polarized

wave is illustrated in Equation 1.8.

$$\vec{S} = \begin{bmatrix} S_0 \\ S_1 \\ S_2 \\ S_3 \end{bmatrix} = \begin{bmatrix} |E_x|^2 + |E_y|^2 \\ |E_x|^2 - |E_y|^2 \\ 2E_x E_y \cos \phi \\ 2E_x E_y \sin \phi \end{bmatrix} \quad (1.8)$$

Notice that, differently from Equations 1.1 and 1.2, the just introduced quantities are time-averaged estimates of the light intensities. Moreover, given the parameters in Equation 1.8, the Degree Of Polarization (DOP, ρ in Equation 1.9) definition can be introduced as well. This quantity defines the amount of polarized part present in a plane wave, in particular:

$$\rho = \frac{\sqrt{S_1^2 + S_2^2 + S_3^2}}{S_0} \quad (1.9)$$

where S_0 describes the total light intensity, and $S_0\rho$ represents the intensity of the polarized part in the monitored beam. Indeed, the total intensity of a light beam consists of both the contribution of the polarized and unpolarized parts in a wave. For sake of clarity, an unpolarized wave does not have a specific pattern orientation of the Electric field, that accordingly moves randomly along the propagation direction. Therefore following Equation 1.8, an unpolarized waves is described as:

$$\vec{S} = S_0 \begin{bmatrix} 1 \\ 0 \\ 0 \\ 0 \end{bmatrix} \quad (1.10)$$

Consequently, given the Equations 1.8 and 1.9, a lightwave can be described as:

- completely polarized: if $S_0^2 = S_1^2 + S_2^2 + S_3^2$;
- partial or unpolarized: if $S_0^2 \geq S_1^2 + S_2^2 + S_3^2$

Therefore, a completely polarized electromagnetic wave has a DOP equal to 1, an unpolarized one has a DOP of 0 while a partially polarized has a DOP in between 0 and 1. Furthermore, considering that, inside the SMF, the S_0 parameter is constant, the \vec{S} vector can be also defined by means of just S_1 , S_2 and S_3 . This new definition of \vec{S} is the one employed in the Thesis and allows to describe a 3D mathematical space, called Poincaré Sphere (Fig.1.9 (b) and 2.8a), which returns a new definition of polarization state based on Equation 1.11

$$\vec{S} = \begin{bmatrix} S_1 \\ S_2 \\ S_3 \end{bmatrix} = \begin{bmatrix} \rho S_0 \cos(2\chi) \cos(2\psi) \\ \rho S_0 \cos(2\chi) \sin(2\psi) \\ \rho S_0 \sin(2\chi) \end{bmatrix} \quad (1.11)$$

where S_0 is the lightwave intensity and ρ is the beam DOP, whereas χ ($-\pi/4 < \chi < \pi/4$) and ψ ($0 < \psi < \pi$) describe respectively the ellipticity angle and the ellipse orientation of

an elliptical polarization shown in Figure 1.9 (a). Consequently, the mathematical space, based on the Stokes parameters, allows to represent any SOP on the Poincaré sphere by means of the quantities in Equation 1.11. In particular, the radius of the sphere is described by the S_0 parameter, the sphere geometry is defined by the $\vec{S}=(S_1, S_2, S_3)^T$ vector and the light beam SOP is described by the remaining S_0, ρ, χ and ψ parameters.

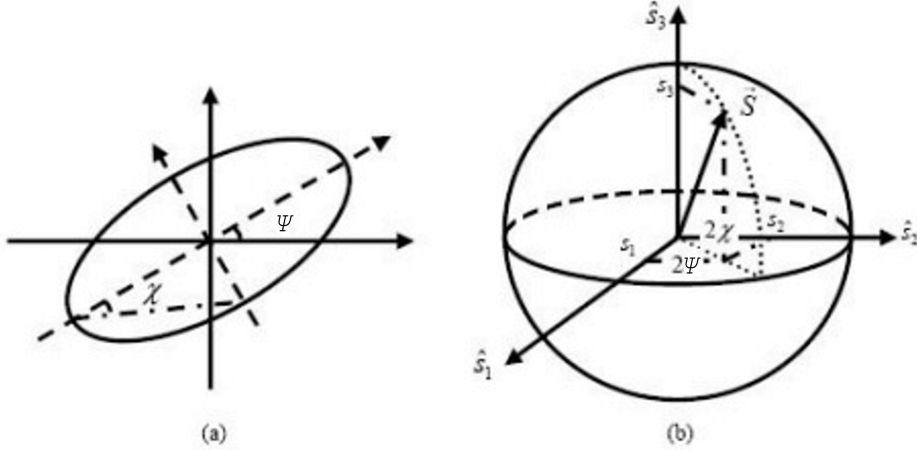


Figure 1.9: a) Elliptical polarization; b) Poincaré Sphere; (Picture taken from [18])

Moreover, due to the DOP (ρ) contribution in Equation 1.11, the pointing vector \vec{S} length is defined by the $S_0\rho$ quantity. Indeed, at the center of the sphere are represented the non polarized waves, on the circumference are represented the completely polarized ones and in between are represented the partially polarized beams.

In the Thesis, the fibers SOP was continuously described by extrapolating the Stokes parameters from the incoming modulated waves, and vibration sensing was applied by estimating the polarization state variations in time. However, during the work, it will be demonstrated that the mechanical motions sensed were not so accurate and it was meaningful to characterize the light SOP variations inside the fibers in a more suitable manner. Consequently, the SOP Angular Speed (SOPAS) was computed and employed for the entire work for the sensing purposes. The SOPAS parameter defines the speed that the tip of the \vec{S} vector achieves to cover a specific angle in a specific time on the Poincaré Sphere. Therefore, the higher is the angle covered in a certain time by the vector, the higher is the variation speed of the sensed SOP inside the probe fiber. The new parameter consist of the Stokes parameters, but it turned out to be much more sensible to the SOP variations with respect to the singular Stokes elements.

1.4 SMF Birefringence

Birefringence is an important property in SMFs analysis and it is the phenomenon that alters the light SOP inside the probe optical path. Assuming ideal conditions, the conveyed beam inside the optical fiber can be decomposed as two orthogonally-polarized

lightwaves on the xy plane which are characterized by the presence of equal refractive indexes ($n_x=n_y$). However, the real scenario inside the fiber is not equal to the one just reported. Most of the times, SMFs are characterized by multiple factors that breaks the symmetry of the fiber core cross-section [16]. This can be induced by the not perfectly circular perimeter of the core, or by imperfections in the cable or by external environment vibrations and strains. The resulting scenario is a system characterized by distinct refractive indexes for two orthogonally-polarized lightwaves ($n_x \neq n_y$) which are strongly subjected to the polarization orientation, inducing birefringence. This effect leads to two different group velocities of the polarized beams, resulting in a phase shift between the two orthogonal lightwaves. In particular, the birefringence can be described by a parameter β obtained in Equation 1.12:

$$\Delta\beta = |\beta_x - \beta_y| = \frac{2\pi}{\lambda} |n_x - n_y| = \frac{\omega}{c} \Delta n \quad (1.12)$$

where c is the light speed, β_x and β_y are the beams propagation constants and Δn is the waves refractive indexes difference. In addition, given the just reported Equation and assuming $\Delta\beta$ as fixed along the fiber, it is possible to extract the orthogonal waves absolute phase delay, which is illustrated in Equation 1.13.

$$\Delta\phi = |\beta_x - \beta_y|L = \Delta\beta L \quad (1.13)$$

The obtained phase delay defines the two beam components group velocities, consequently they will experiment a different group delay $\Delta\tau$ between them (Fig. 1.10), inducing a strong variation of the SOP inside the fiber. However, birefringence effects are usually not constant along the optical cable length. Birefringence can be accidentally or intentionally introduced in the fibers, indeed, for instance, in the polarization maintaining fibers a strong and stable level of it is inserted in the fibers in order to maintain its polarization state steady along the SMF.

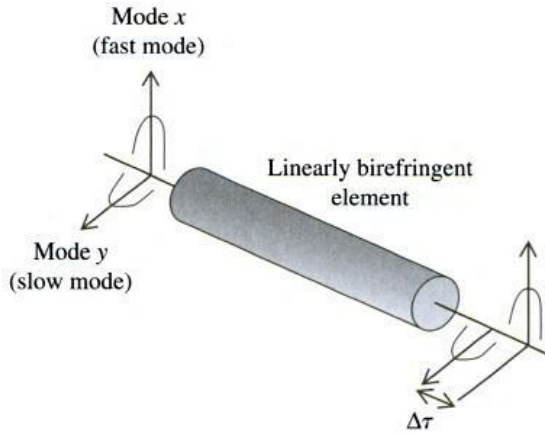


Figure 1.10: Differential group delay induced by the birefringence (Picture taken from [7])

Most of the time, birefringence is an unwanted effect, because it changes the conveyed light beam SOP inside the fiber and limits its data rate, therefore should be kept as low as possible. In addition, external vibrations contribute to increase the birefringence effects inside the fiber and the resulting SOP variation speeds as well. However, because of their low level of intrinsic birefringence, SMFs hold a key role in the Thesis vibration sensing purposes because they are significantly sensitive to external perturbations [5].

1.5 Organization of the Thesis

Chapter 2

Experimental Setup based on an Optical Switch

Now that it has been cleared the importance of polarization state variations in the fiber for sensing purposes, an in depth examination of the setup can be provided. The goal of the system configuration is to acquire and monitor the previously described Stokes parameters from the monitored fiber and to enhance the detection of potential dangerous events with the insertion of an optical switch .

2.1 Employed equipment and mountain model

The block scheme of the proposed experimental setup is shown in Figure 2.1 in the 2-fibers configuration. The green arrows refers to the optical fiber connections, while the black edge represent a USB electrical link.

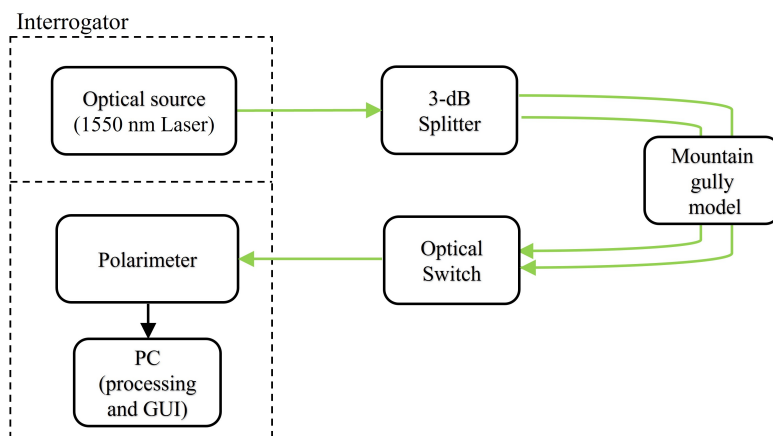


Figure 2.1: System block scheme

The interrogator included a 1550 nm emitting light laser, a polarimeter that extrapolated the Stokes parameter inside the sensed optical signal and returned the SOP evolution in time, and the user PC, needed to display and process the computed outcomes through an evaluated MATLAB script. The scheme illustrated in Figure 2.1 clearly recalls the multiplexed structure in the ladder topology reported in Figure 1.2 (b), indeed the conveyed optical source is portioned on each of the sensors, with the difference that the return fibers were collected into a unique cable through an optical switch, which allowed to alternatively monitor the modulated light coming from the different optical paths. The generated optical signal propagated inside a reduce scale mountain model on which simulations of rockfalls or other dangerous events has been done with the purpose of altering the polarization state of the monitored probes. The introduced risky occurrence will be finally sensed from the polarimeter and displayed on the user laptop through a provided GUI (Graphic User Interface). In addition, an optical splitter and an optical switch have been introduced in the equipment in order to achieve the goal of monitoring at least 2 sections of the mountain/model simultaneously.

Now that is was cleared the optical signal path, a detailed description of the employed devices in the system is provided:

- Optical Source:

It is a CW (Continuous Wave) laser emitting single mode light at 1550nm in the IM-DD (Intensity Modulation Direct Detection) configuration, therefore it does not use an external modulator and the optical attenuation inside the fiber is minimum; The source hardware is shown in Figure 2.2.

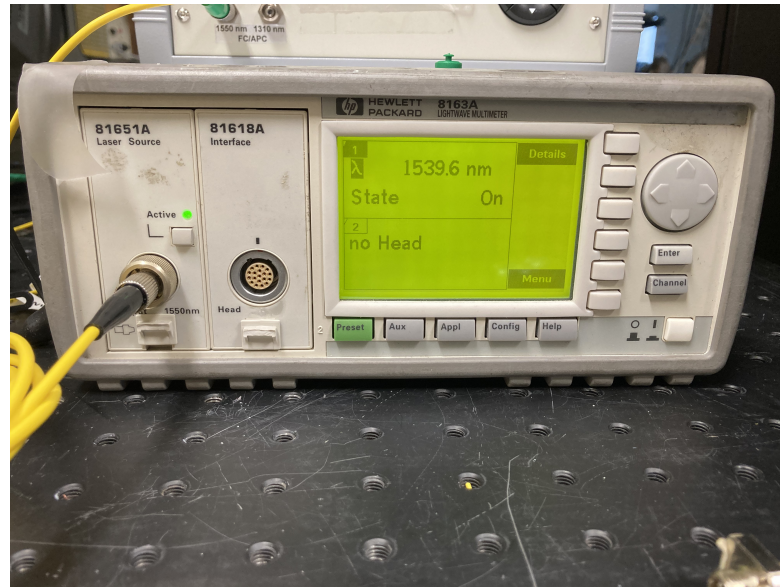


Figure 2.2: Optical Laser Source

- Non-PM-fibers:

They were the actual sensors of the setup, indeed they were continuously monitored to capture the variations of the SOP inside the system. To do it, they had to be non-polarization maintaining, more precisely, this type of fibers do not introduce a predefined strong level of birefringence as the Polarization Maintaining (PM) do, therefore the polarization state inside the monitored optical paths is not preserved and the SOP variations due to birefringence inside them are better detected [12]. Consequently, as showed in the Poincaré display on the polarimeter user interface (Fig.1.9), the DOP (Degree of Polarization) inside the optical signal had to be approximately one.

- 3-dB Splitter:

It is a symmetric passive device that halve the input signal into two outputs introducing a small Insertion Loss (IL), therefore a power amplitude attenuation. Notice that the instruments IL was not a problem in proposed the system, because the monitored optical gain amplitude did not interfere with the SOP evaluations, with the exception that oncoming the signal must had a power level higher than the minimum sensed by the polarimeter, i.e. -35dBm. The purpose of the splitter was to generate two independent light probes to be inserted in different position of the model, in this way the monitoring of two sections of a mountain side can be properly simulated.

- Mountain side model:

Then, the optical signals (at least two) propagated along a reduced scale wood structure (benevolently provided from the Politecnico di Torino and the Geosolving s.r.l) that aimed to simulate a real mountain side, on which potential dangerous event can occur. In order to made the experiments as real as possible, the side model has been filled with a 10 *cm* thick mixture of soil and sand, and multiple SMFs (Single Mode Fibers) have been buried inside it. As shown in Figure 2.3, the structure was 3 meters long and 0.7 *m* large, with an inclination of 30° with respect to the horizontal plane.

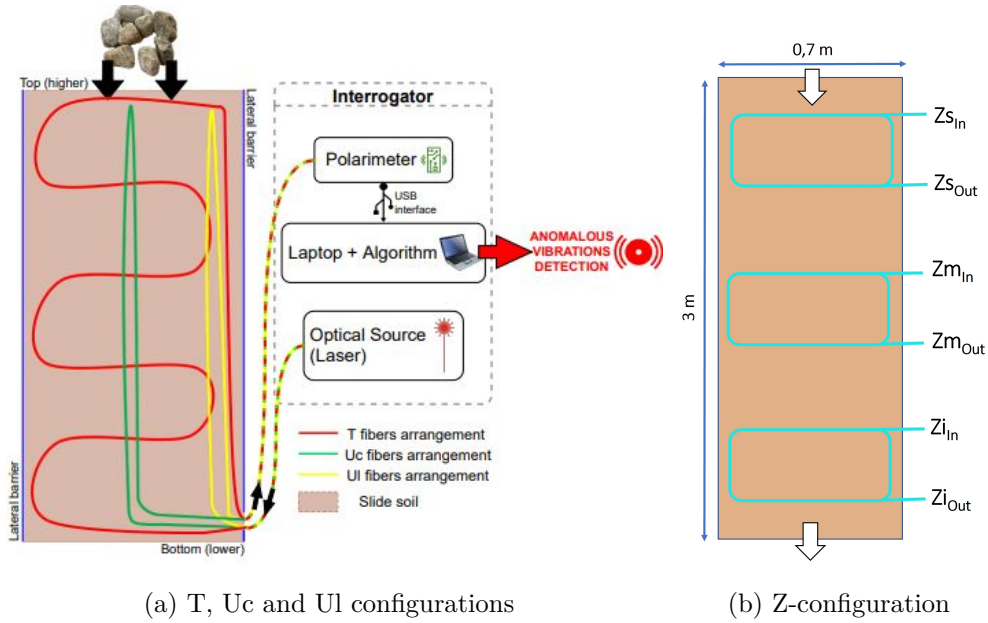
The system has been covered by a geotextile, a very common fabric in geological applications that maintains the ground regular and equally distributed on the system when mechanical motions are tested on the soil. Moreover, the fibers on the slide have been buried with different patterns and depths. This is the most critical point, because aimed to study which path returned the most reliable and accurate variations of the SOP when a dangerous occurrence was rolled down on the probes. As a consequence, the fibers have been arranged on the slide in three different configurations: transversal (T), longitudinal (U) and sectioned (Z). Taking as reference Figure 2.4 (a) and 2.4 (b) a detailed explanation on the fibers arrangement pictures is provided. The red lines represents the T pattern and it consisted on a serpentine layout that crosses the entire model, in this way, three equally spaced (1 *m*) sections of the slope have been covered. The expected performances should be the most reliable because allowed a regular sensing along the entire model due to the extended detection area. On the contrary, the longitudinal traces are separated in Uc (green)



(a) Side view of the Model

(b) Top view of the Slide

Figure 2.3: Mountain downhill model



(a) T, Uc and Ul configurations

(b) Z-configuration

Figure 2.4: General fibers arrangement

and Ul (yellow), and cover respectively the central and the lateral sections along the soil. The main impairment of those arrangements should be lack of reliability due to the thin area monitored, therefore the sensing operation will be more accurate or not depending on how far the occurrence come down. Finally, the latter displacement was the actually used in the Thesis (Fig.2.4b) and it is called Z-configuration. Differently from the T and from the U patterns, it does not cover the entire slide but

only small portions of it. The purpose of this arrangement was to sense the dangerous event from different regions of the model and consequently to understand where the occurrence started and where is happening. Thus, it allows a sort of real-time localization of the rockfall, feature that the previous configurations cannot exploit. The Z-fibers have been arranged in three ring configurations and disposed on the top, on the middle and on the bottom of the model, in order to cover entirely the slope but with independent paths. Consequently, they have been called Zs (stays for 'superiore'), Zm (stays for 'in mezzo'), and Zi (stays for 'inferiore'). The analysis performed during the work will focus mainly on the top and on the bottom sections of the Z-configuration, because they covered separate areas 2 *m* apart, and their evaluations were expected to be almost independent. Furthermore, for each pattern, the probes have been buried at different depth: 1cm (Z3), 5cm (Z2) and 9cm (Z1), for a total of 18 fibers interred in the soil (Tab. 2.1). This allowed to study how the ground level above the probes impacted the sensing performances. Obviously, deeper was the probe, lower was the amplitude of the sensed event.

<i>Fiber name</i>	<i>Depth</i>	<i>Configuration</i>	<i>Fiber name</i>	<i>Depth</i>	<i>Configuration</i>
T1	9 cm	Transversal	Z1s	9 cm	Sectioned, top
T2	5 cm		Z2s	5 cm	
T3	1 cm		Z3s	1 cm	
U1c	9 cm	Longitudinal, central	Z1m	9 cm	Sectioned, middle
U2c	5 cm		Z2m	5 cm	
U3c	1 cm		Z3m	1 cm	
U1l	9 cm	Longitudinal, lateral	Z1i	9 cm	Sectioned, bottom
U2l	5 cm		Z2i	5 cm	
U3l	1 cm		Z3i	1 cm	

Table 2.1: Fibers configuration

During the experiments, the dangerous occurrence have been simulated by letting fall on the slide different objects as a a 5 *cm* single Rock (SR), a 15 *cm* ceramic Cylinder (C) and a Debris Flow (DF) made of 25 single rocks (Fig. 2.5). Most of the times the object have been rolled down from the top of the slide and caught in a basin at the bottom of the model, however, to validate the sections SOP independence, in some simulations the events have been started from the middle or stopped before they reached the bottom section.

Also in this case, the simulated risky occurrence have been chosen with different size and weight in order to produce various effects on the monitoring system. Clearly, the Debris flow will be the most dangerous in terms of variation of the SOP and it will be easily detected also from the deepest fibers in the model, while, on the contrary, the single rock may be almost not sensed from the 9 *cm* optical paths and the Z2 or the Z3 will be employed.

- Optical Switch:



(a) Single Rock And Ceramic Cylinder

(b) Debris Flow

Figure 2.5: Simulated Dangerous Events

Before the polarimeter, an optical switch was inserted to alternatively select one of the oncoming probe fibers and to monitor them as fast as possible. Moreover, due to the instruments highly cost, it was employed with the purpose of reuse the already present equipment. This condition verified the multiplexing sensor array scheme described in Chapter 1 and in Figure 1.2 (b), on which multiple sensors sharing the same interrogator block were employed to make the analysed technology more affordable. In particular, a detailed and dedicated part of the work on the optical switch is provided in Section 2.2.

- Polarimeter:

The main instrument of the setup, it was used to extract the 4 Stokes parameter from the probe fiber and to reproduce its SOPs variations over time. In other words, it extrapolates the real word information about the polarization state carried out by the optical signals buried in the soil and converts it in SOPAS evaluations. The instrument model was the PM1000 provided by Novoptel and reported in Figure 2.6 (notice that all the inserted images about the PM1000 are taken from the device datasheet [11]).

A key feature of the instrument is its sampling rate of 100 MS/s , therefore it was an extremely accurate device, with a SOP accuracy $\leq 0.01 \text{ rad}$. Furthermore, it provides a specific parameters configuration that allows to set the employed instrument memory, acquisition time and sampling speed as desired. Below are reported some of them:



(a) Polarimeter front view



(b) Polarimeter back view

Figure 2.6: PM1000

1. Averaging Time Exponent (ATE): it defines the internal averaging operation performed by the polarimeter on the acquired Stokes. It is needed to increase the SOP measurements accuracy at low optical input power. More in details, after the 100 MS/s AD conversion, 2^{ATE} samples are averaged, generating a new acquisition sampling speed of:

$$f_s = \frac{100 \text{ MS/s}}{2^{ATE}} \quad (2.1)$$

The ATE parameter ranges from 0 (i.e: not averaging and $f_s=100 \text{ MS/s}$) to 20 (i.e: min $f_s = 95 \text{ S/s}$), therefore it allows to control the average rate of the acquired Stokes parameters and consequently the SOP evaluations sampling speed.

2. Memory Exponent (ME): it defines the size of the internal memory that will store the acquisition. It ranges from 10 to 20, therefore it can achieve blocks of 2^{ME} measurements (for instance the max memory size is of 64 MSamples). If combined, the ME, the ATE and the original sampling time of 10 ns define the actual recording time of the polarimeter, so the period in seconds on which the instrument continuously stores the information provided by the input fiber. Therefore:

$$t_{tot} = 10 \cdot (2^{ME} \cdot 2^{ATE}) \text{ ns} \quad (2.2)$$

3. Normalization mode: It defines the normalization factor applied to the Stokes

parameters. The instrument provides different modes, but in the work, the standard one was used, therefore the measurements are normalized on the Poincaré space to the unit length, regardless on other parameters. Consequently, the \vec{S} vector will point to the surface of the Poincaré Sphere.

All the above described parameters can be manually controlled through an easy user-interface provided by the producers 2.7 or by the reading and writing to the instrument internal registers. Of course, to communicate, the device and the user PC have been connected through a USB cable.

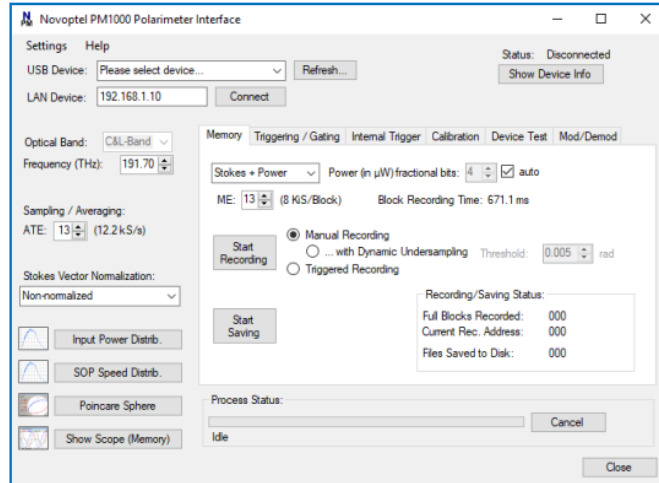
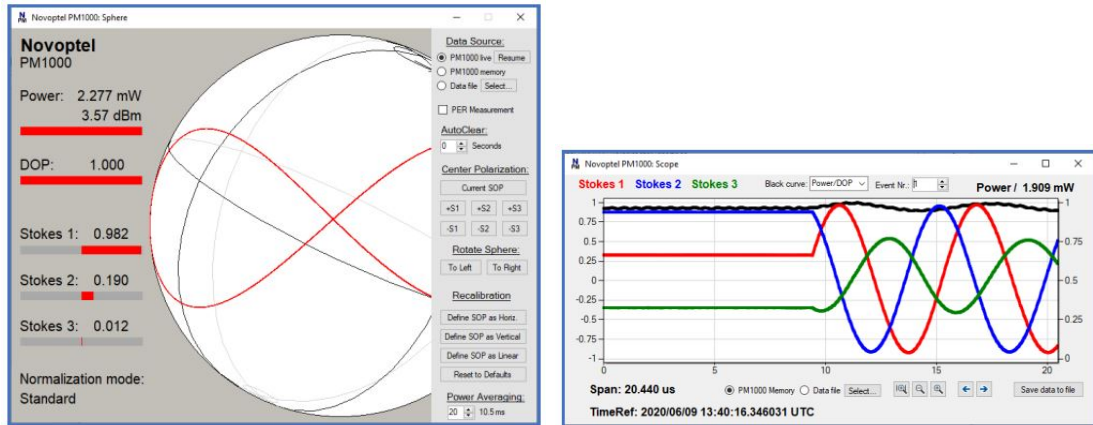


Figure 2.7: PM1000 user interface



(a) Poincaré Sphere

(b) Oscilloscope view

Figure 2.8: User interface plots

The instrument evaluations can be real-time displayed on the user interface through the Poincaré Sphere (Fig.2.8a), which continuously computes the power level, the

Stokes parameters and the SOP of the monitored fiber. The latter, therefore the tip of the \vec{S} vector, is represented as a red dot on the sphere surface. Moreover, the instrument allows also to store for t_{tot} seconds the Stokes parameters evolution over time and then to display them through the provided oscilloscope view (Image 2.8b). As a consequence, the four traces of the S_1 (red), S_2 (blue), S_3 (green) parameters plus either the power (actually computed) or the SOPAS can be stored and sent to the user PC as a .bin file allowing post processing operations on the evaluations.

2.2 Description of the used Optical Switch

Now that the setup block scheme has been introduced, the next section will deal with a detailed description of the optical switch device, focusing on its main features and impairments. In particular, to achieve the goal of an almost multiplexed sensing system that monitors multiple fibers at the same moment, an 1x4 optical switch was introduced in the experimental equipment. The employed optical switch is used to selectively connect one fiber to one of a set of multiple channels [8] and controls the routing operation between inputs and outputs ports. In other words, it is a device able to alternate the optical input¹ port whenever an electrical command is received. It is composed by 5 optical cables, as shown in Figure 2.9, that represent the four inputs ports and the output one, called *common*.

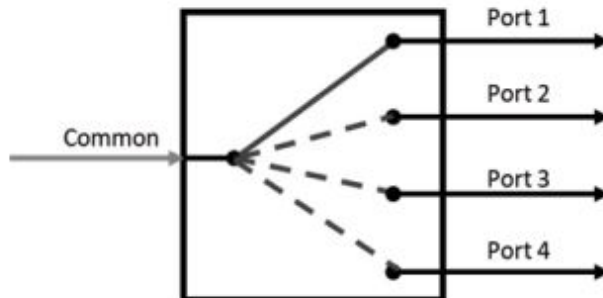


Figure 2.9: Optical Switch ports

When the device is working, only two ports are actually active and contribute to the communication, the common (always open) and one of the four exits. The others are closed and do not bring any data, until an external electrical modulation modifies the connection ends. In the simulation, the switch was intentionally chosen in order to not insert electrical conversions to the probe light, therefore the information that passes through the device remains all in the optical domain. In this way the instrument does not introduce any latency, data corruption or timing jitter [17]. Furthermore, it guarantees the requested

¹The device is symmetric, therefore the data does not have a direction.

conditions: low cost, low insertion loss, channel isolation, transparency with respect to the optical system and a high speed commutation of the output port, that is $\leq 5ms$ [8]. In the telecommunication background, the optical switch is mainly used in WDM (Wavelength Division Multiplexing) networks and for protection in case of link failures. In particular, the latter is employed when a malfunction on the transmission occurs, therefore, to not lose the communication, the device routes with high speed the incoming light into a secondary optical path and the communication can continue. Furthermore, the optical switch can be applied in monitoring systems, on which different fibers can be monitored by switching each different channel of the $1 \times N$ device. This last application is very similar to the environment in which the device has been implemented in the Thesis.

Consequently, in the work, the goal of the switch was to commute periodically the oncoming fiber, so that the polarimeter could continuously monitor multiple probes coming from different sections of the reduced scale downhill model. In this way, the sensed outcomes will give more accurate information about the ongoing landslide with respect of using one optical path only. In addition, the device had to iterate the channels as fast as possible in order to get more reliable SOP computations, therefore the measurements time on each channel had to be very small. As a consequence, a deterioration of the device due to an extremely higher number of commutations with respect to the actual real usage (e.g. link failures) could limit the Thesis purpose (this problem was not emerged in the simulations, but it is convenient to highlight it).

More in the details, the optical switch is divided into three main sections:

- Mechanical: the needle that commutes the input ports.
- Optical: the input and outputs cables.
- Electrical: eight wires being the logical pins which control the needle.

To understand the working principle of the latter, Figure 2.10 shows the actual blocks scheme that drives the switch:

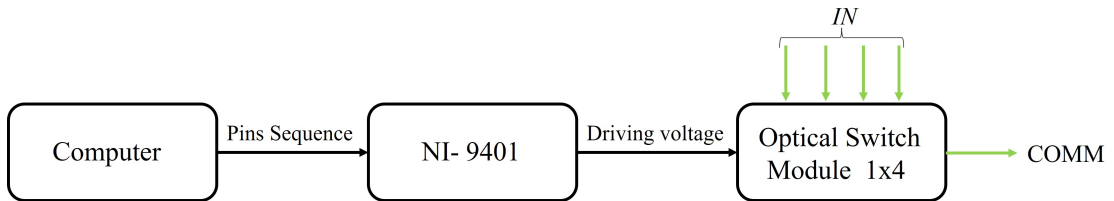


Figure 2.10: Optical Switch block scheme

First step was started from the user computer, called also *controller*, which had to generate through MATLAB a sequence of eight bits to directly control the pins on the NI-9401 board and to establish which port of the switch will be open. Each channel of the switch is controlled by a specific bit sequence, that is defined in the instrument data-sheet and reported in Table 2.2. Between the bits and the board pins there is a one-to-one mapping, therefore the i -th bit control the respective pin.

IN PORT	P1	P2	P3	P4	P5	P6	P7	P8
PORT 1	0	1	1	0	0	0	0	0
PORT 2	1	0	0	1	0	0	0	0
PORT 3	0	1	0	1	0	0	0	0
PORT 4	1	0	1	0	0	0	0	0

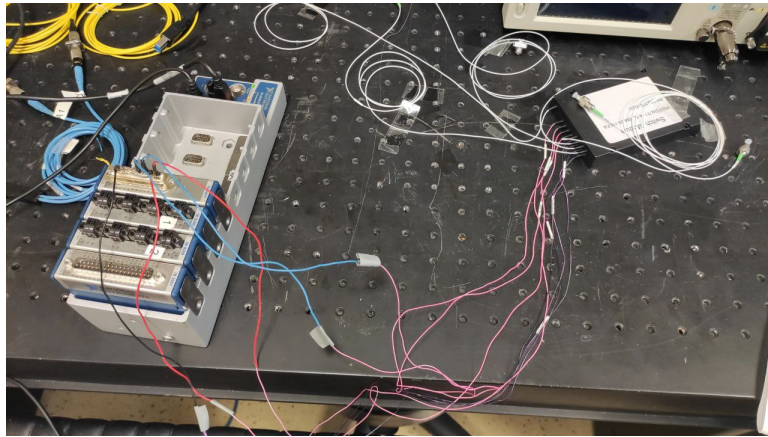
Table 2.2: Ports pins sequence

The NI-9401 (National Instrument) is a digital I/O interface and has a 25-pin connector that provides connections for eight digital input/output channels [1]. It is inserted in a *chassis* (an electronic supporting structure) and it is connected to the controller through a USB cable. The main goal of the NI-9401 is to generate a 5 V/*TTL* signal on active pins, therefore on those that are defined as 1 in the received bits sequence generated by the computer (Fig. 2.16). The TTL acronym stands for Transistor-Transistor Logic and has the purpose to represent a digital bit sequence as an analog domain wave. Finally, interconnecting the electrical copper wires of the NI board connector with the ones of the switch, the latter receives the transmitted bits sequence from the pins of the NI in the form of a voltage and can control the mechanical needle inside. This is why it was previously declared that the connection path inside the optical switch was driven by an external electrical modulation.

Figures 2.11a and 2.11b illustrate the devices that composed the just described model.



(a) NI-9401 board (Picture taken from [1])



(b) Optical switch complete view

2.3 First Experiments with the Optical Switch

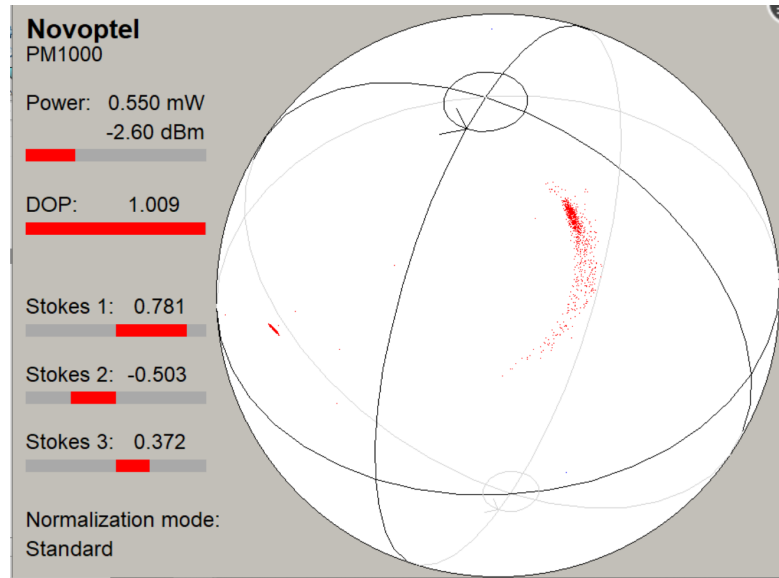
After the instrument working conditions have been declared, some first easy simulations have been performed in the Photon Laboratory, in order to test if the switch actually worked and if it returned the expected results. Consequently, the landslide model was not

used for these experiments, and the vibrations were simulated by simply touching one of the two fibers. The goal of the analysis was to understand how the switching operation affects the SOP. Outcomes has been analysed looking at the polarimeter GUI (Graphic User Interface), showing the Poincaré Sphere and the Oscilloscope plot.

From now on the term switching time (t_s) is referred to the time needed by the switch to commute the input port ($\leq 3ms$), while the term switching period (T_{sw}) states the time between two commutations, therefore it is the measurement period per fiber.

The first tests have been performed with a 2-fiber detection system and with a very simple MATLAB code by sending every T_{sw} seconds a new pins sequence to the National Instrument board. In this way it was possible to alternate the two input ports of the optical switch with a fixed period, and to monitor as fast as possible the two fibers state. Meanwhile, the polarimeter acquisition was triggered and the SOP of the oncoming fiber was saved for about 10 seconds, with a sampling frequency of 6.103 kSamples/s (therefore looking at Equation 2.2, the ATE was set equal to 14 and the ME equal to 16). The outcomes didn't need any processing, their time evolution has been monitored by the instrument user interface.

Figure 2.12 shows the obtained Poincaré Sphere.



(a) Global view

Figure 2.12: Poincaré sphere, only one fiber stressed

From the images, it was clear that the fibers tested have two different SOPs, therefore the \vec{S} vector heads towards two different points on the surface of the sphere. Furthermore, it was likewise visible that only one of the two fibers was subjected to a manually generated source of stress or vibrations and different clouds of measurements were generated. The first, illustrated in a zoomed version in Figure 2.12b, correspond to the fiber that was

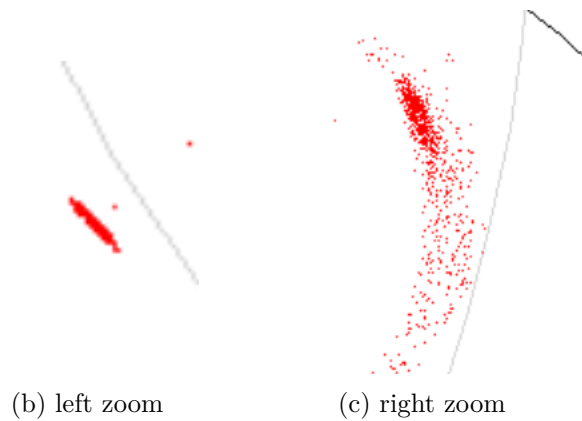


Figure 2.12: Poincaré sphere, only one fiber stressed

kept quiet and no specific motions of the SOP in the plot have been detected, unless the intrinsic noise of the instrument. On the contrary, Picture 2.12c shows the stressed fiber, indeed the measurements in this case are not fixed and cover a larger area due to the polarization state oscillations.

Stokes parameters and SOPAS time evaluations were analysed in order to monitor how they changed if submitted to a stress source. Also in this test, only one out of the two probes was subjected to vibrations.

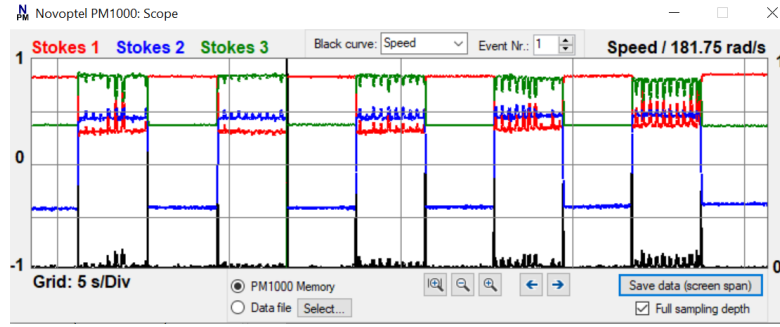
In particular, Figure 2.13 shows the variation of the parameters S_1, S_2 and S_3 inside both the fibers.

Observation 1 The plots illustrated in Figure 2.13 don't have same x-axis time reference.

Notice that, in the figures, the black line refers to:

- In image 2.13a it represents the SOPAS evolution in time of the fiber that reaches the polarimeter. The expected trend should be constant if no events are detected, while it should oscillates when a mechanical vibration will occur. However, a huge and narrow peak of the SOPAS is generated when the switch commuted, because the oncoming channel, and consequently the sensed SOP, changed very rapidly and a sharp variation of the polarization state is detected. Notice that, the true variations of the SOP are a bit visible between the spikes and they behave as expected, even if they are almost neglected by the peaks generated by the switch.
- In Figure 2.13b the black trace is the S_0 parameters, so the optical power inside the fibers and normalized to the maximum value in the data set. As expected, it is constant except during the commutations, when it goes to zero due to the absence of power crossing the device. It then moves to the other constant measured value.

From the Poincaré and the oscilloscope plots it was possible to notice that the four parameters and therefore also the SOPs followed different trends inside each sensed fiber, therefore jumps in the traces are present when the switch iterates, exactly as in Figure


 (a) $T_{sw} = 2\text{ s}$, $f_s = 6.1\text{ kS/s}$

 (b) $T_{sw} = 50\text{ ms}$, $f_s = 6.1\text{ kS/s}$

Figure 2.13: SOPAS and power, oscilloscope view

2.12. Finally, the stressed fiber is again easily recognizable, indeed the plots alternates periods of constant trends with periods of oscillating ones. Moreover, the optical switch behaved as expected and its employment allowed correctly to monitor with fixed and periodic measurements time multiple fibers in different motion states .

2.4 Optical Switch Impairments

Until now the experiments have been performed only to understand if the optical device worked correctly and to investigate the first achieved results. Next steps actually started the true research.

As reported in the first sections of the Thesis, the initial simulations on the optical switch aimed to minimize the time between each iteration of the device (T_{sw}) and therefore to make the detection system as reliable as possible. Indeed, a high monitoring speed allowed to sense the switch channels very fast and to capture also the most critical motions inside the fibers. To do it, let's focus on Picture 2.14. The Figure represents a spectrogram and it analyses an experiment on which the same SR event reported in Figure 2.5a was simulated and the same model reported in Figure 2.3 was employed, therefore the outcomes obtained in the plot will be valid also for the developed work. Moreover, it has to be noticed that to have a better visualization of the results, the illustrated plot was represented in linear

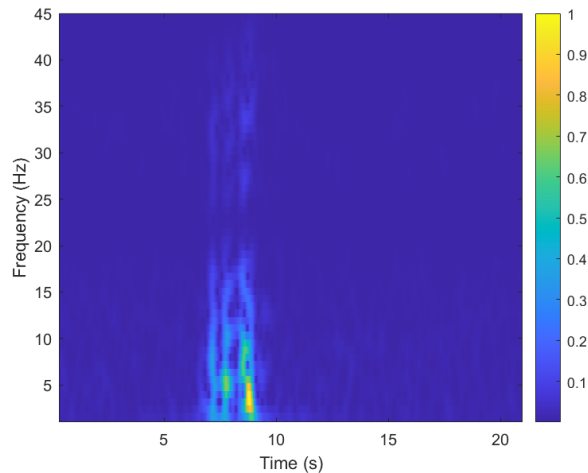


Figure 2.14: Single rock spectrogram (Picture taken from [13])

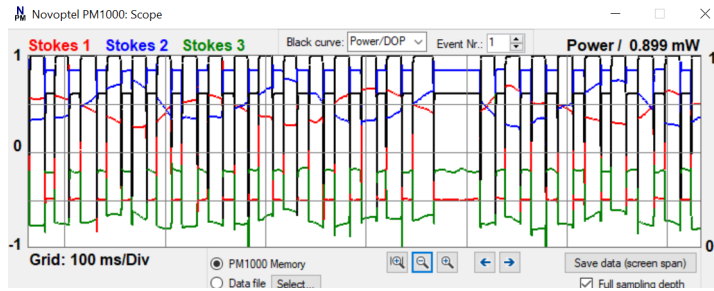
scale and its power level was normalized. The main visible outcome is that the occurrence showed the relevant spectral information at very small frequencies, for the sake of clarity at around 5 Hz . Consequently, it was possible to sample the signal subjected to the SR vibrations also at very low rates without losing information about the event. Therefore, in the before mentioned work, a sampling frequency of 95.4 Hz was used, because equal to the minimum f_s that the polarimeter hardware could achieve. This choice allowed to greatly reduce the amount of data processed and stored in the detection algorithm, key feature in the monitoring systems because they can run also for consecutive days and the amount of acquired information may not be manageable if the sampling rate was high. However, the reported results have been obtained from a single-fiber detection system, consequently in this Thesis, the optical switch had to iterate (at least) at twice the above f_s if two optical path are sensed. In this way, if one measurement per switch commutation was acquired, the same sampling rate per fiber of the previous configuration was achieved. For this reason the desired T_{sw} was set to 5 ms (i.e. switching speed of 200 Hz).

Then, same simulations of the previous section has been performed, in order to study if the devices could work properly at the requested rate. As a consequence, first impairments started to emerge. Figure 2.15 illustrates them.

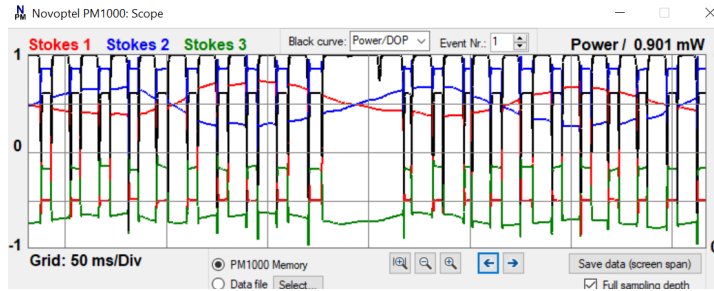
In the plots and in the simulations was clearly visible that, when the switch commutations were spaced by a time lower then 15ms , sometimes the device skipped one or more iterations and the measurements periodicity was totally cancelled. Moreover, it has been noticed that the disruptions of the switch were not constant or predictable, and their repeatability increased with the decreasing of the parameter T_{sw} .

This wrong and not expected behaviour introduced two main problems:

- a rise of the DSP (Digital Signal Processing) operations complexity;



(a) $T_{sw} = 10ms$



(b) $T_{sw} = 5ms$

Figure 2.15: First optical switch impairments

- unbalanced measurements periods, therefore the outcomes were no more particularly accurate and reliable.

Therefore a debug session on the electrical components of the optical switch has been performed to find out where the problem was. The NI 9401 board 2.11a and the electrical wires connected to the instruments 2.11b were analysed in detail, in particular:

1. To validate the correct operation of the board, one of the bits stream sequence contained in Table 2.2 was sent through Matlab. Then, with a multimeter, the National Instrument device has been tested and its correctness was validated if active pins were actually generating +5 V. To better understand the debugging, Figure 2.16 shows which elements of the table have been referred to the NI connectors and an example of how they have been monitored. The first solution returned the expected results, therefore the board actually was generating +5 V where and when requested.

Observation 2 Last four bits of the generated sequence were always zero, therefore in the connector they have been electrically grounded together.

2. To validate correct behaviour of the switch module, the electrical wires of the device, the pink ones showed in Figure 2.11b, have been connected to a power supply (Picture 2.17). The instrument was used to generate two constant voltage levels of +5 V and 0 V on the wires that should be respectively '1' or '0' based on the desired bits sequence. In this case too, it was discovered that the switch commuted properly the

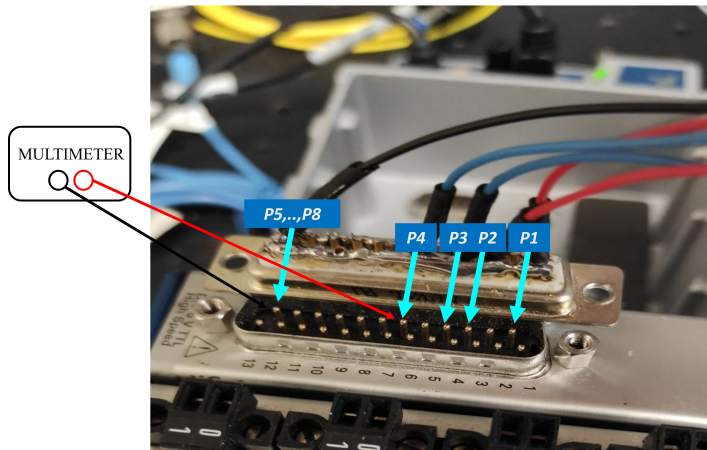


Figure 2.16: NI 9401 connector and driving Pins

output port when it received the correct level of voltage.



Figure 2.17: Front view of a Power Supply single channel (figure taken from [1])

To recap, if analysed individually, the two elements worked correctly. Another debug session was performed, but this time with the the NI-9401 and the switch module connected. Finally, it was noticed that the problem actually took place in this configuration, because the voltage generated by the board and measured with a multimeter was no more $+5\text{ V}$, but $+2,6\text{ V}$. Therefore, it was not enough to move the mechanical needle inside the switch. It was firstly thought that the switch absorbed too many current from the NI connectors, and as a consequence the voltage generated decreases, but then, after deeper analysis of the components, it came out that one of the major disadvantages of the TTL technology used by the NI-9401 is its high current demand [1]. The heavy current utilization could be the cause that led to an incorrect functioning due to switching of output states.

2.5 Solutions employed in post-processing

Now that the issues of the setup have been found, next sections will deal with the solutions employed to fix it. Two different solutions have been tested.

2.5.1 NI 9269 breadboard

The first employed solution was to change the National Instrument board on the chassis and to perform same tests performed in the debug session. The new NI-9269 board is a four independent channels device able to provide up to +10 V for each of them. The availability of two equal boards allowed to simulate the 8 channels/pins as desired.

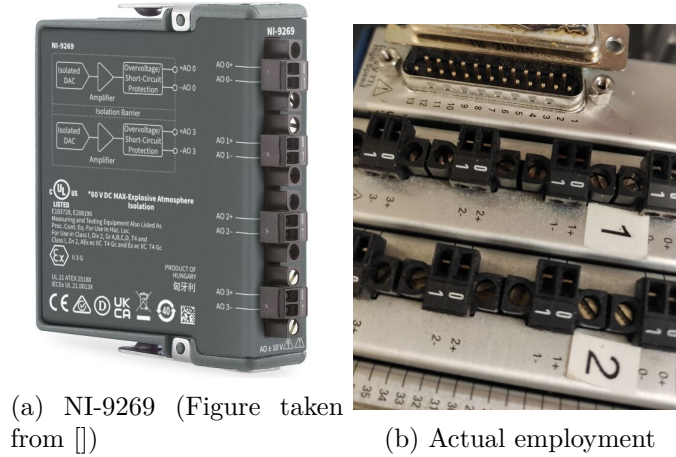


Figure 2.18: NI-9269

The two identical devices have been linked together by connecting to the same ground level all the logical slots indicating the '0' as in Figure 2.18. As a consequence, the slots indicating the '1' have been connected to the eight electrical wires that drove the optical switch module. In this way, the previous configuration was achieved and its working principle remained unchanged (with the exception of the different NI boards).

Expected outcomes had to compensate the high current demand thank to the higher level of voltage generated. Unluckily, the new setup didn't return the desired output, because the measured voltage when the NI component and the switch module were connected was again below the requested +5 V.

2.5.2 Arbitrary Function Generator

A new solution was formulated focusing on the bits sequences in the Table 2.2 on Section 2.2. Assuming a monitoring system composed by two fibers, the switch had to commute between two output ports, therefore the PC, through Matlab, had to send alternately two sequences of eight bits every T_{sw} seconds. Considering port 1 and port 3 only, the bit sequences needed to open the channels are:

- Port 1: 0 1 1 0 0 0 0 0
- Port 3: 0 1 0 1 0 0 0 0

and comparing them, it was noticed that:

1. first two bits are equal;
2. third and fourth bits alternates, therefore when the third bit of port 1 is high, the third bit of port 3 is low, and vice versa. The same for the fourth bit;
3. last 4 bits of every sequence are always zeros (not only in port 1 and 3, but in all the channels);

Consequently, the two sequences can be represented as six fixed elements plus two synchronized square waves shifted in phase by 180° , which corresponded to the third and the fourth bit of the given pattern. Figure 2.19 explains the purpose of generating two square waves.

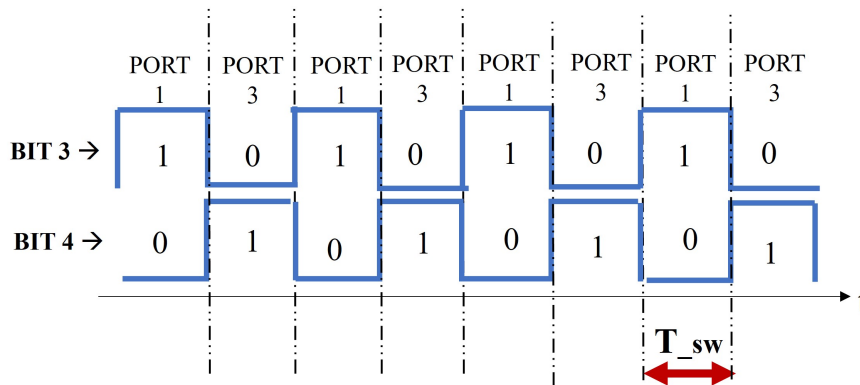


Figure 2.19: Square waves working principle

As the figure clearly illustrates, the traces, if synchronized, reproduced perfectly the two bits behaviour in a continuous time. Therefore, every half of the waves period, the output port was expected to commute correctly.

The square signals have been independently generated by an Arbitrary Function Generator (AFG) with two channels and had an amplitude of $+6 V$ when a '1' should be generated and of $0 V$ otherwise (Fig. 2.20).

The amplitude of the voltage level was higher with respect to the one generated from the NI board, because it was required to compensate the high current demand from the optical switch. To connect the devices, the wires representing pins 3 and 4 of the switch model have been connected to the waves generator, while the remaining constant elements have been connected to a power supply, which reproduced the requested fixed voltage ($+5 V$ on ones and $0 V$ on zeros). The new setup is reported in Figure 2.21 and the actual connections inside the optical switch block scheme are reproduced.

This new configuration allowed to change the output port of the optical switch by simply alternating the status of the third and of the fourth bit of the generated driving sequence. Moreover, the switching period (T_{sw}) has been controlled as desired by generating two square waves of period $2 \cdot T_{sw}$ and a Duty Cycle (DC) of 50%.

Then, the pro and the cons of the new configurations have been below reported.



Figure 2.20: Parameters set to generate the square waves

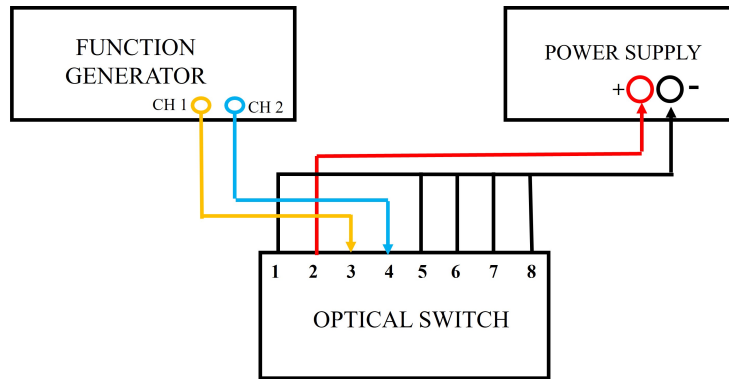


Figure 2.21: New optical switch setup

- Cons:
 1. The previously considerations have been evaluated assuming to work with two ports only. Moreover, they are neither correct for all the possible couple of ports. For example channels 1 and 2 have the first four bits different in the sequences reported in Table 2.2. This implies the requirements of two synchronized function generator, therefore four arbitrary channels. The solution in this case become highly complex and expensive. Same problem emerged with the four fibers monitoring. To sum up, the new configuration limited the simulations to a system based on 2-fibers only;
 2. Real time simulations can be complex, because the function generator may not be programmable;
 3. Phase difference between the square waves must be verified with the oscilloscope. Unfortunately just fixing it to 180° was not always optimal;
- Pros:
 1. The optical switch worked perfectly. The requested switching period ($T_{sw}=5$

$m.s$) has been reached, because the communication latency introduced between the instruments has been erased.

2. The function generator (Fig. 2.22) controls the switch and defines its switching frequency (as half of the waves period), therefore with this configuration the computer and the NI board were no more used.



Figure 2.22: The Arbitrary Function Generator (figure taken from [1])

2.6 Solutions employed in Real-Time

The goal of the real-time simulations was to provide results as soon as the single measurements have been acquired, so that the detection of a dangerous event could provide extremely fast alarms. Consequently, a continuous and accurate control on the instruments was needed, in order to manage them at each instant of the simulation. Unfortunately, the previously described solutions were no more exploitable for these new purposes, so new solving processing have been used.

2.6.1 Programmable Function Generator

The first solution that was tested was to control the Arbitrary Function Generator employed in the post-processing solution. The advantage was to reuse the setup already configured, hoping to maintain the same performances.

Therefore, from the instrument data-sheet [1], it was discovered the possibility to remotely program the instrument behaviour through the SCPI protocol. The SCPI (Standard Commands for Programmable Instruments) is a command language expressly used to control and test instruments with an ASCII based code.

Luckily, Matlab provides to the users an already defined app called Instrument Control that allows to control the instrument without writing any lines of code. In other words, it helps the consumer with an easy user interface (2.23) that converts the desired actions in a SCPI Matlab code. Then, the parameters set in Figure 2.20 have been inserted in the new program, in order to generate the same square waves, with the difference that the DC must be of 100%. This operation was needed to match the waves period with T_{sw} , allowing a complete control on each iteration of the optical switch. Finally, the new

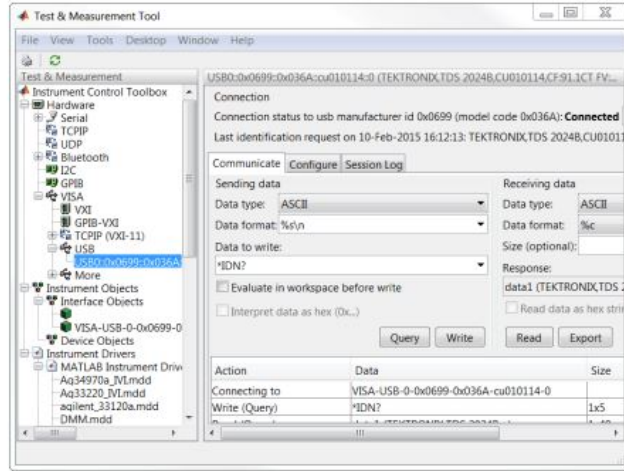


Figure 2.23: Instrument Control user interface

method was simulated and the waves behaviour was monitored with an oscilloscope. The displayed signals correctly followed the expected trends. In other words, due to the 100% DC employed, two horizontal lines were alternating between the set low and high levels, and the output optical port of the switch properly iterated as a consequence. However, again, decreasing the switching period (T_{sw}) the latency introduced by the communication between the controller (the PC) and the instrument became significant with respect to the Thesis time purposes and a new solution was tested.

2.6.2 Electrical Operational Amplifiers

Because of the loss of voltage reported when the switch and the National Instrument board (the 9401) have been connected, an electrical amplifier was inserted between them. Therefore, the last and best solution was obtained using an operational amplifier in the voltage follower.

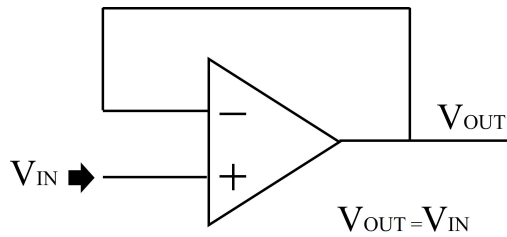


Figure 2.24: Voltage follower operational amplifier

The voltage follower is the simpler between the op. amp. configurations (2.24). It is an amplifier with unitary gain, therefore the output voltage is maintained equal to the input

one and no amplifications or loss are introduced in the system. Moreover, due to the circuit high input impedance, it provides isolation between the input and output signals. The unwanted absorption of current should be compensated from the $\pm 15 V$ power supply and, as a consequence, its presence in the optical switch setup was extremely helpful.

Taking again as reference Table 2.2, four operational amplifier have been employed, accordingly to the first bits of each sequence, that alternate between 1 and 0 in the reported sequences, while the remaining pins have been grounded because always equal to 0.

Experiments have been firstly performed on a breadboard, then, after checking that everything has gone correctly, a permanent circuit has been weld. The new setup of the optical switch obtained (Fig.2.25) was the same as the one illustrated in Figures 2.10 and 2.11b, with the exception of the electrical amplifiers and of a double channel power supply. The first was inserted between the NI board and the switch module, in order to maintain constant the generated voltage; while the latter was needed to generate the electrical power needed to supply the new components.

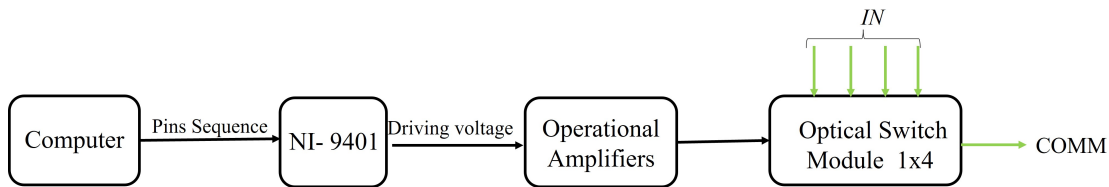


Figure 2.25: Optical switch op.amp.block diagram

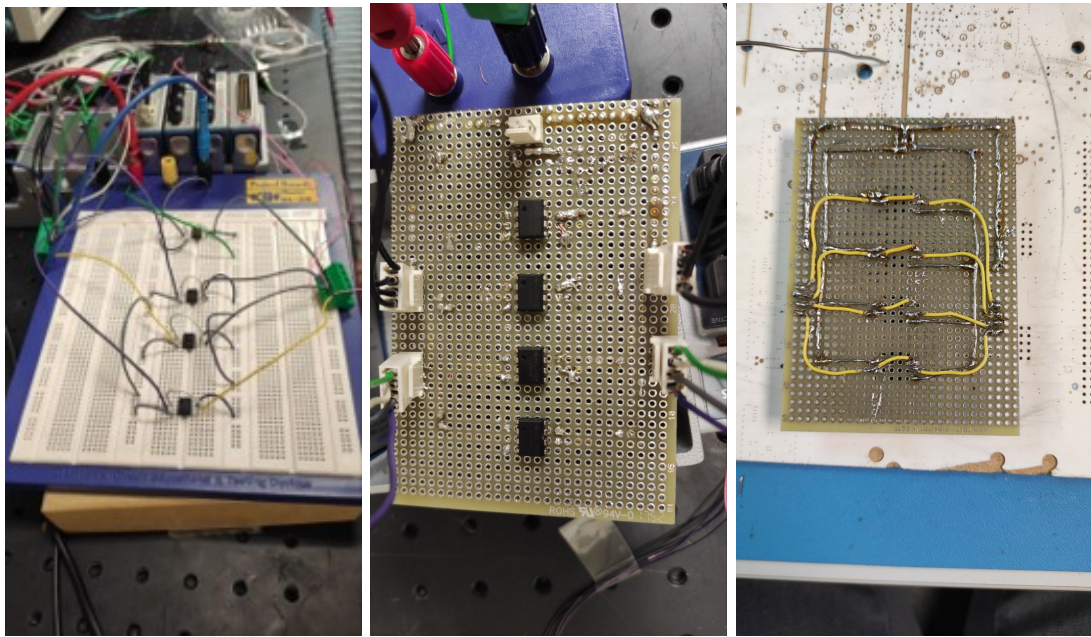
Figures 2.26a, 2.26b and 2.26c illustrate the generated circuit on the breadboard and the welded one.

The new system succeeded, the NI 9401 board, when connected to the optical switch module, correctly generated $+4,9 V$ and the current absorption was compensated.

The advantage of the new pattern with respect to the one employed in post processing was the lack of the function generator, therefore less instruments were needed (the power supply was still present) and the system cost has been reduced. As a consequence, all the small impairments introduced by the generated square waves are avoided, for instance the not perfectly synchronized signals and the required phase alignment operations. However, the MATLAB platform was again needed to control the optical switch, therefore the electrical part still remained the main limitation in terms of switching speed, because at high velocities ($T_{sw} \leq 8 ms$), some errors on the switching periods occurred.

2.7 Summary: post-processing and real-time setup

To conclude, the configuration with the function generator and the single channel power supply was perfect for the post-processing simulations, because it allowed to switch the input fiber at very high speeds without using the MATLAB platform, and it achieved the goal of measuring the alternating fibers for a period of $5 ms$ each. A picture of the final



(a) 4 op.amp breadboard (b) Welded circuit front (c) Welded circuit back

Figure 2.26: Operational Amplifiers

post processing setup is illustrated in Figure 2.27. In the image are present the following instruments: laser source, splitter, optical switch, function generator, power supply and polarimeter.

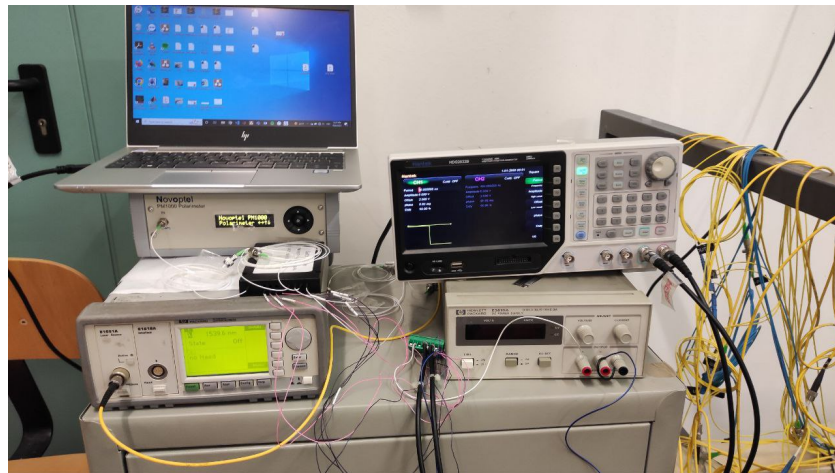


Figure 2.27: Final Post Processing in Setup

However, the setup with the NI 9401 board and the operational amplifiers (and the two channels power supply) was more suitable for the real time operations, because allowed a

remote control on the instruments (polarimeter and switch) and reached speeds that were not too far from the expected targets, therefore still valid (Fig.2.28).

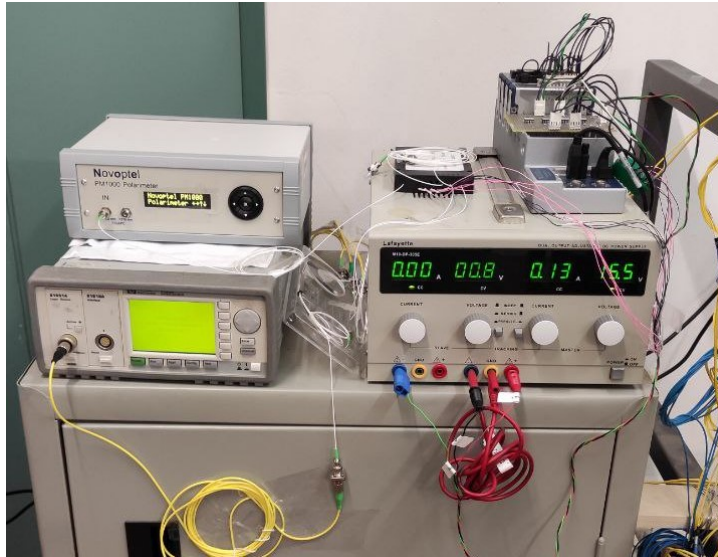


Figure 2.28: Final Real Time Setup

Moreover, the arrangement with the operational amplifiers could be used also for the post processing operations (even if it didn't reach the desired speed) and turned to be the best solution between all the simulated. Notice that the above described experimental arrangements were defined to employ a detection system based on two fibers, therefore the optical switch was actually working in the 1x2 configuration and half of the provided ports were not actually used. Thus, to increase the number of monitored fibers and to properly use the 1x4 switch module, two parallel 3-dB optical splitter have been inserted in cascade of the already present. In this way, the single laser beam was halved and each of the outputs produced two new signals, for a total of four independent optical paths. Therefore, the 4-fibers setup is illustrated in Figure 2.29.

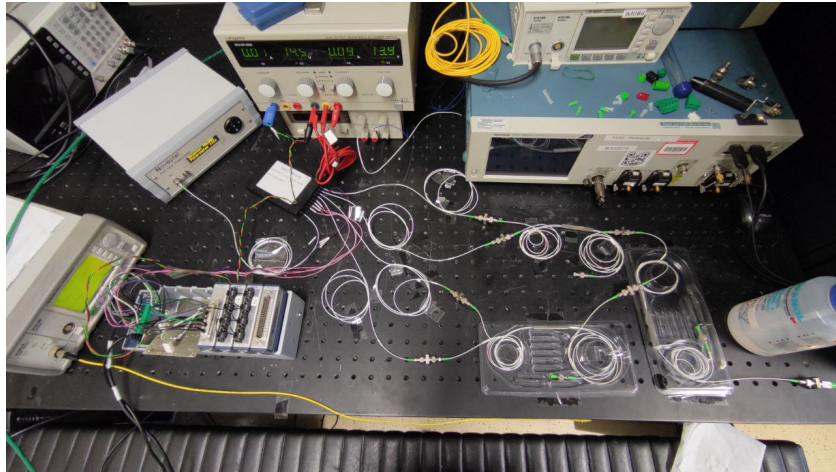


Figure 2.29: 4-fibers experimental setup

Chapter 3

Initial Measurements with elaboration in post-processing

To sum up, Chapter 2 has introduced the basis to understand the main topics of the Thesis and have reported a detailed description of the instruments arrangement. Therefore, the next sections will be focused on the performed experiments and on the obtained outcomes. In particular, before analysing the final real-time alarm generation algorithm, post processing experiments have been extremely useful to validate the system correct functioning and to enhance as much as possible the accuracy of the performances through a devoted study on the employed parameters.

3.1 Digital Signal Processing and selection of the parameters

As reported in Section 2.5.2, the post processing (PP) setup was based on the arbitrary function generator to create the square waves needed to make the optical switch properly work. Therefore the PC was not needed in the simulation, and it was only used to acquire the Stokes parameters from the polarimeter and to process them. Before applying the DSP, an entire experiment has been executed following the next steps:

1. Start the signals generation through the AFG and the consequent optical switch iterations;
2. Launch the polarimeter acquisition through the provided user interface, it will last for an amount of time set by the ATE and the ME parameters;
3. Generate the dangerous events;
4. Stop the switch when the polarimeter has finished;
5. Save the measurements in a .bin file and process them through Matlab.

In addition, Table 3.1 reports the parameters that were set on the provided GUI to perform the desired acquisitions:

ATE	ME	f_s [kHz]	t_{tot} [s]
14	16	6.103	10.73

Table 3.1: Set parameters of the polarimeter

The purpose of the next DSP operations was to enhance as much as possible the experiments performances and to lay the foundation for an efficient real-time algorithm to be applied in an authentic monitoring system. Indeed, the main feature of the PP method was its offline nature, meaning that:

1. the outcomes of a simulation were displayed and analysed only when the experiment ended (included the signal processing);
2. it allowed to replicate the saved measurements on the user PC as many times as needed and to work with them to enhance the results.

On the contrary, the real time method returned the evaluations as soon as they have been processed, but didn't allow the possibility to process them more than once, and therefore, to reach better results. More precisely, the performed PP operations focused on the detection problem, which, in general, produces three different results:

1. Correct Detection (CD): when an event is correctly detected from the simulation;
2. False Alarm (FA): when a risky event detection is returned but no landslide occurred. It is mainly caused by an high level of noise or by not dangerous event.
3. Missed Detection (MD): when a danger is occurred but the algorithm does not detect it.

Therefore, the goal of the employed offline mode was to increase as much as possible the CD probability before passing to the real-time simulations.

Consequently, the current Section will describe the processing steps applied in the algorithm, which are illustrated in the scheme reported in Figure 3.1.

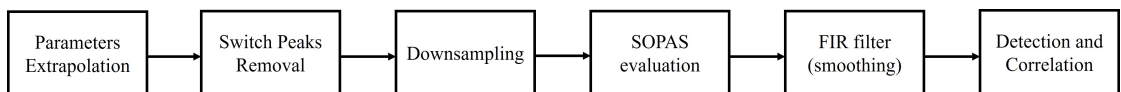


Figure 3.1: Post processing block scheme

After that, each block of the PP chain is explained, focusing on the operation executed and on the parameters definition.

- Parameters Extrapolation:

The first operation performed was the extraction of the Stokes parameters and of

their relative timestamps from the .bin file. What was obtained are the raw measurements of the polarimeter, through which the post-processing can start. An example of the extracted \vec{S} vector is illustrated in Figure 3.2a, where the raw data not processed of a 2-fiber simulation is showed. Moreover, it can be noticed that the extrapolated parameters perfectly matched the GUI oscilloscope view shown in Figure 2.13b and once again, the unwanted switching impact on the acquisitions (vertical lines) is extremely visible.

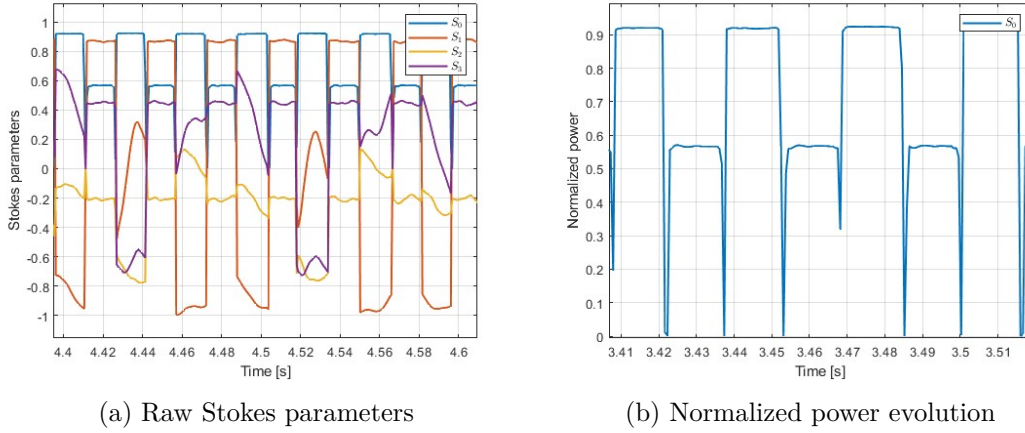


Figure 3.2: Stokes extrapolation

- Switch peaks removal:

More in details, the spurious marks in Figures 3.2a and 3.2b were produced by the optical switch commutations and represents the sharp variations of the Stokes vector inside the sensed fiber. Therefore, to properly process the four parameters behaviour, the commutation peaks had to be removed, because they did not behave to the optical signals SOP measurements.

Consequently, for the next operations, let's focus on the power behaviour plot showed in Figure 3.2b, thus on the Stokes parameter S_0 . Since the conveyed light was generated by a constant laser source, the optical power inside the probes after the splitter followed an unvaried trend for the entire experiment duration. However, the queried fibers had slightly different power levels, therefore, when the optical switch iterated, the sensed S_0 parameter moved to the other monitored fiber power value. Hence, the S_0 first derivative trend should be constant and almost zero for all the instants in which its trace was fixed, while it should generate a commutation peak when switches occurred. Consequently, the samples belonging to these peaks represent the switching instants and define exactly what should be removed from the acquisitions. The above described behaviour looks like very similar to the SOPAS evolution showed in image 2.13a, on which the black vertical lines defined the SOP speed of variations inside the queried fiber and once again, they were provoked by the commutation of the switch.

Figure 3.3 illustrates the power first derivative trend and the actual measurements time achieved for each fiber if the unwanted samples have been removed.

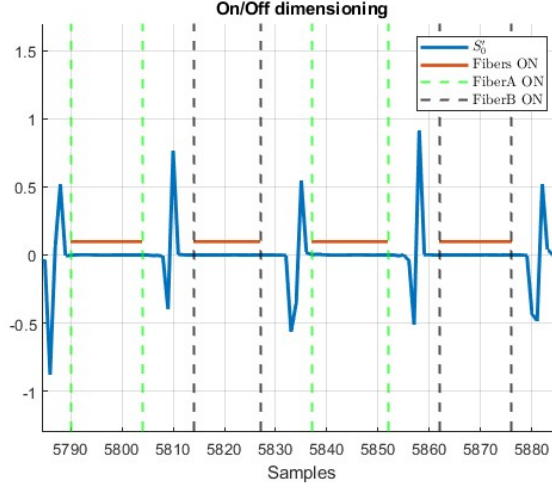


Figure 3.3: Derivative of the power and correct measurements periods

Especially, in the algorithm, the absolute value of the derivative was tracked, in order to detect also the negative summits. Therefore, the switch commutations were erased by eliminating the samples and the timestamps in the neighbourhood of the peaks in the \vec{S} vector. After that, if the setup employed worked correctly, the dotted lines showed in the Plots defined the actual measurements time on each fiber, which should be almost unvaried for the entire experiment and approximately equal to T_{sw} .

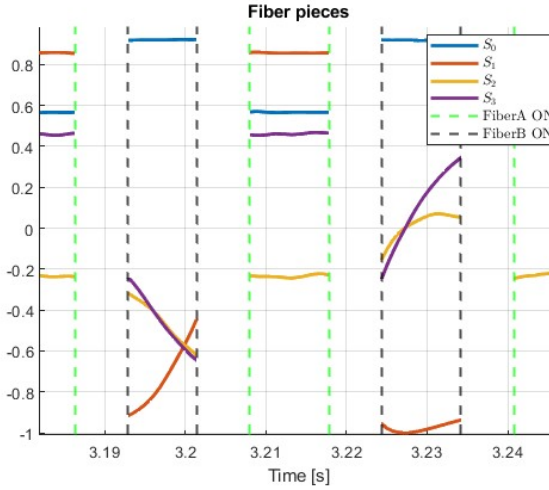


Figure 3.4: Stokes parameters after peaks removal

A zoomed example of the obtained processed traces is reported in Figure 3.4, on

which the spurious marks in the Stokes parameters were correctly removed.

Observation 3 Both images 3.2a and 3.4 are referred to initial experiments performed to validate the actual correct functioning of the experimental setup. Therefore, the mechanical vibrations inserted in the system were manually generated without the employment of the downhill model, indeed the SOP variations look greatly clear. However, in the real simulations, the Stokes parameters didn't alter so clearly, consequently, it will be demonstrated that to monitor the SOP variation speed instead of the \vec{S} vector was a better solution.

- Downsampling:

Up to now, the performed processing steps were applied on the parameters directly acquired by the polarimeter, so with a sampling frequency that has been set in advance and controlled by the ATE parameter in the GUI ($f_s = 6.103kS/s$). However, as specified in Section 2.4, the events in the spectrogram plot (Fig.2.14) can be sampled at much smaller frequencies without losing information about the events. Therefore, the optical switching speed was set to 200 Hz in order to guarantee at least one sample per fiber every 10 ms (so 100 Hz per optical path). As a consequence, in the post processing operations, the sampling rate was reduced by averaging all the Stokes parameters and the timestamps that belonged to the same measurement slot (orange lines in Figure 3.3). In this way, for every iteration of the switch, one sample representing the averaged \vec{S} vector behaviour in that slot was obtained, and the resulting processing sampling speed matched the optical switch one. For sake of clarity, Figure 3.5 summarizes the impact of the processing steps executed until now on the Stokes parameters, therefore extrapolation, peaks removal and down-sampling.

The plots highlight a simulation on which one fiber was shaken approximately for 7 seconds. The interpolation (i.e. Matlab spline() command) operation reported in the third image was needed only to illustrate the behaviour of the smoothed parameters in a continuous pattern, but it wasn't actually employed in the code.

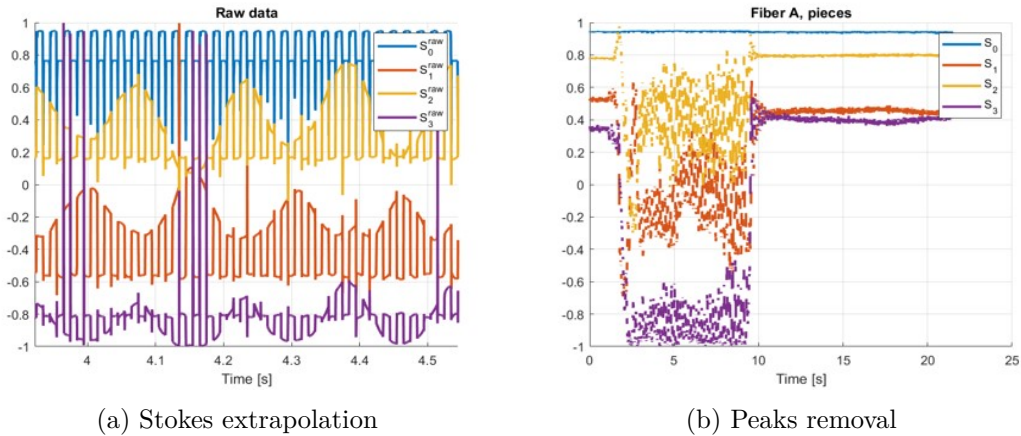
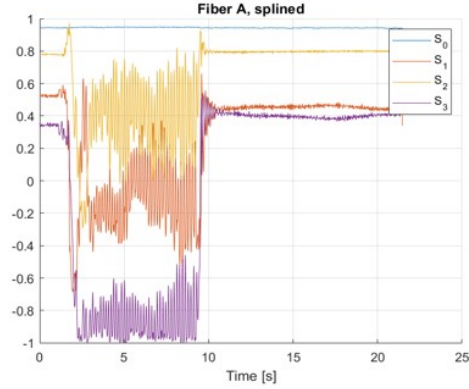


Figure 3.5: Processing steps



(c) Interpolated downsampling

Figure 3.5: Processing steps

- SOPAS evaluation:

As already described in [13], the analysis of the Stokes parameters to detect dangerous events turned out to be complex. The first reason was due to the three dimensional nature of the parameters (S_0 was not needed to track the fibers SOP variations), therefore finding an algorithm that represented the \vec{S} vector on the Poincaré sphere became tricky. The second cause was related to the parameters response when an external source of vibration was generated. Indeed, it was experimentally demonstrated that the variation of the SOP on the Stokes was not always clear and sometimes weak, independently on the generated events on the fibers.

An example of their evolution in a real experiment is reported in Figure 3.6:

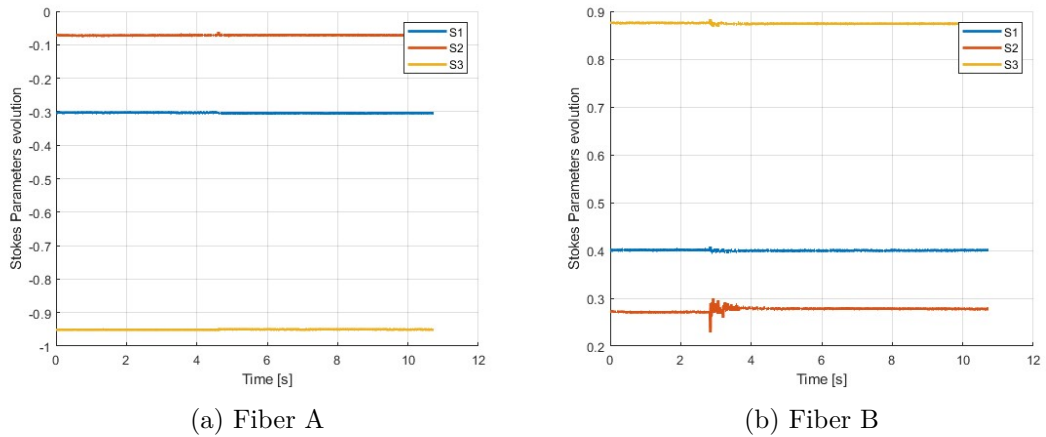


Figure 3.6: Evolution of the Stokes parameters S_1, S_2 and S_3

It is clear that the only parameter that showed some variations on its state was S_2 ,

even if it was greatly slight in fiber A. For this reason, instead of implementing an algorithm that monitored the \vec{S} parameters individually, the angular speed of the polarization state variations (SOPAS) was analysed, and it was computed following Equation 3.1.

$$\begin{aligned} \Delta\theta(k) &= \arccos \left(\frac{(\vec{S}^k, \vec{S}^{k-1})}{\|\vec{S}^k\| \|\vec{S}^{k-1}\|} \right) = \\ &= \arccos \left(\frac{(S_1^k \cdot S_1^{k-1}) + (S_2^k \cdot S_2^{k-1}) + (S_3^k \cdot S_3^{k-1})}{\sqrt{(S_1^k)^2 + (S_2^k)^2 + (S_3^k)^2} \cdot \sqrt{(S_1^{k-1})^2 + (S_2^{k-1})^2 + (S_3^{k-1})^2}} \right) \end{aligned} \quad (3.1)$$

where \vec{S}^k is the Stokes vector containing the parameters S_1, S_2 and S_3 belonging to the k -th sample of the experiment, while \vec{S}^{k-1} represents the preceding sample acquired from the same fiber. The obtained parameter represents the angle difference (in radians) between two consecutive SOPs on the sphere, therefore by dividing $\Delta\theta(k)$ for the sampling time it was obtained the variation speed achieved to cover that angle.

$$\omega(k) = \left| \frac{\Delta\theta(k)}{T_s} \right| \quad (3.2)$$

Equations 3.1 and 3.2 illustrate how the SOPAS parameter was obtained in the algorithm, in which it is always expressed in *rad/s*. Since the equations are valid on the single fiber measurements, $T_s = 1/f_s$ is the actual period that passes between two measurements on the same optical path, therefore it is the sampling time per fiber. After that, the three dimensional problem was transformed into a simpler single dimension speed computation, indeed, as it is described in the next Sections, the new parameter showed the key feature of being much more sensible to the SOP variations. Therefore, from now on, the sensing operations will be focused on the sample by sample monitoring of the SOPAS parameter.

- Smoothing:

This block of the post processing chain aims to reduce the SOP angular speed oscillations and to decrease as much as possible the noise floor. It simply consisted in a mathematical moving average operation. Thus, shifting one sample of the evaluated SOPAS at a time, the buffer representing the signal window was filled and the average of the loaded samples was returned. After that, the window was shifted of one element and the average was again given back. The buffer size was represented by a parameter called T_{mov} which defines the delay introduced by the buffering operation in time. As for the SOPAS computation, the average procedure was applied independently on each fiber, in order to not join the evaluations coming from different sources.

Therefore, the total number of evaluations per fiber needed to fill the signal window was defined in the Equation 3.3:

$$M = \lfloor T_{mov} \cdot f_s \rfloor \quad (3.3)$$

Where f_s is again imposed as the post processing sampling speed per probe and therefore equal to 100 Hz (if two probes has been sensed), while T_{mov} was expressed in seconds. Of course, the round operation was needed because the buffer size is defined by an integer value. The performed operation can be thought as a Finite Impulse Response filter (FIR) with length M and coefficients (b_0, \dots, b_M) all equal to $1/M$. Figure 3.7 illustrates the filter scheme.

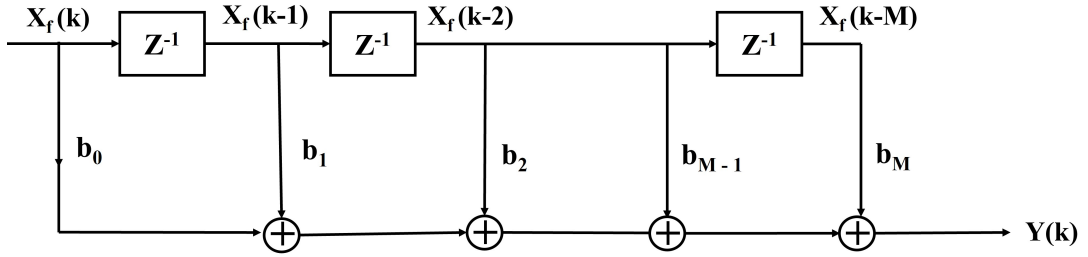
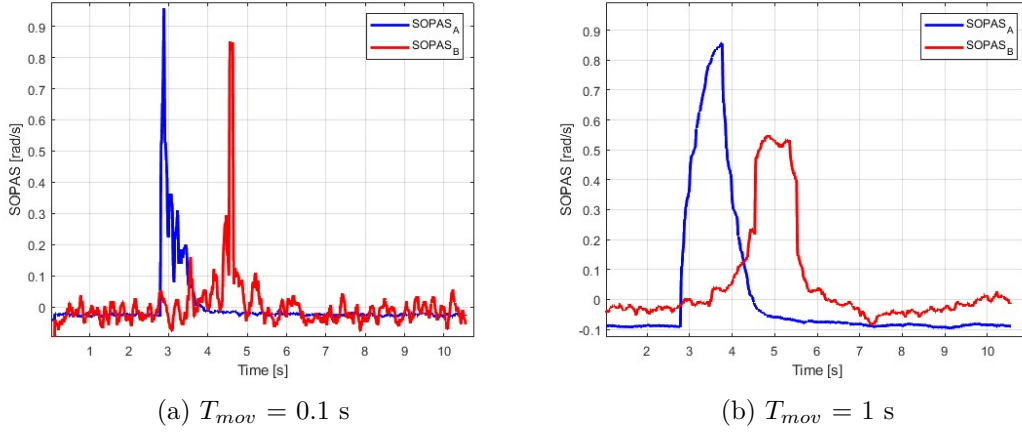


Figure 3.7: FIR filter Scheme

Notice that the buffer $X_f = (\omega(k), \dots, \omega(k-M))$ contains the last M previous SOPAS evaluations acquired from the same fiber.

Moreover, dependently on the T_{mov} parameter, system performances changed. For instance, a larger T_{mov} produced more reliable detection, because increasing the average operation reduced the signals oscillations and the resulting noise floor, consequently the resulting SOPAS threshold was easier to be set. However, if the window was too large, the introduced delay could be a problem in a real-time experiment and the smoothing operation can miss some small, but still dangerous, events.

An example of the impact of the T_{mov} parameter is illustrated in Figure 3.8. The reported plots exhibit a 2-fiber simulation performed on the reduced scale mountain slide model show in Figure 3.14, therefore the mechanical vibration were generated by the real objects listed in Figure 2.5. As expected, the more averaged traces returned a more smoothed and clear trend and the dangerous limit was easily assigned. Nevertheless, the image with the bigger smoothing window (the right one) show a shift of the fibers SOPAS main peaks toward the right in the time axes, because averaging slightly decreases the accuracy. For this reason, a trade-off between accuracy and reliability was needed to set the proper window length. In the simulations, the buffer size was most of the time set between 10 and 100 samples, introducing an equivalent delay of 0.1 to 1 seconds.


 Figure 3.8: T_{mov} impact on the normalized SOPAS evolution

- Detection and Correlation:

Lastly, system performances have been evaluated dependently on the parameters processed up to now. The detection of an event has been managed as a threshold problem, therefore, sample by sample, if the filtered SOPAS ($\bar{\omega}(k)$) exceeded the set threshold ($\bar{\omega}(k) > \omega_{th}$), a risky occurrence will be considered. In order to enhance as much as possible the system outcomes, a careful study on ω_{th} must be done. For instance, an high ω_{th} reduces the possibility to generate alarms due to the noise (so reduces FA), but it can increase the misses due to its high condition. On the contrary, a low threshold value decreases the MD probability, but can erroneously increase the occurrence of risky events. Again, a trade off was needed to maximize processing performances. In addition, the possibility of sensing two fibers (at least) simultaneously allowed to generate an improved system able to detect and recognize non-dangerous events (e.g. animals walking, tree falling, etc.), that were triggered by mechanical vibrations occurred near a single monitored area. More precisely, an alarm message was actually displayed if two or more fibers sensed the same event inside a predefined time slot of some tens of seconds. This is the key point of the work and also the reason why the optical switch was introduced in the system. Indeed, if the event was sensed from only one optical path inside the set time period, it implied that the occurrence was not risky for the Thesis purposes and no warning message was displayed, consequently, the events counter was reset and the tracking stage was started again. For sake of clarity, Figure 3.9 illustrates a simulation where the dangerous occurrence was sensed by one fiber only, therefore the event was classified as not risky and no warnings were generated. Notice that the FA example was produced manually without the employment of the mountain model, therefore the obtained SOPAS amplitudes were not comparable with the values returned with the reduced scale landslide simulations.

Finally, the cross correlation between the normalized SOPAS evolution of each fiber

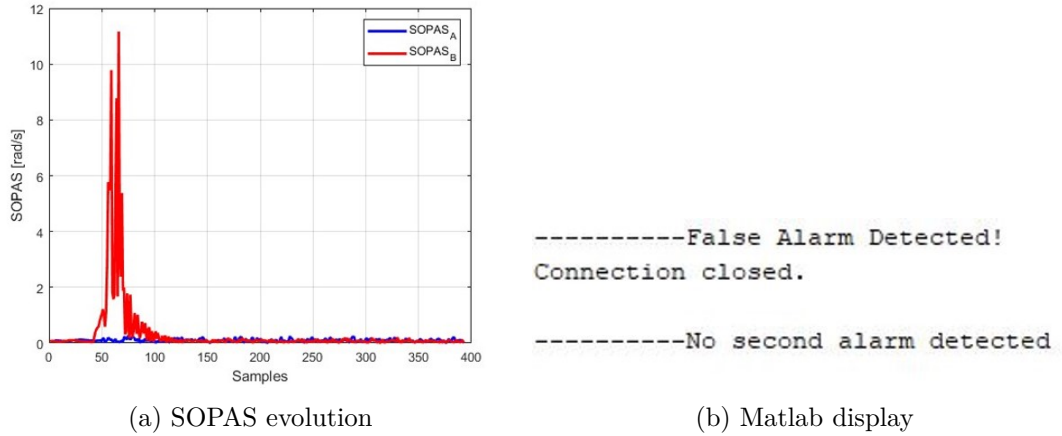


Figure 3.9: Example of a non-dangerous event, $T_{mov}=0.1 s$

has been evaluated. As it will be described in section 3.2, normalization was needed because sometimes the simulated models did not provide the same level of sensing and the evaluations returned different peaks amplitude on the same event. The convolution has the dual purpose to compute the distance in time between the sensed occurrence and to compute the resulting rolling speed of the rockfall. An example of the cross correlation on the SOPAS trends between two fibers is illustrated in Figure 3.10.

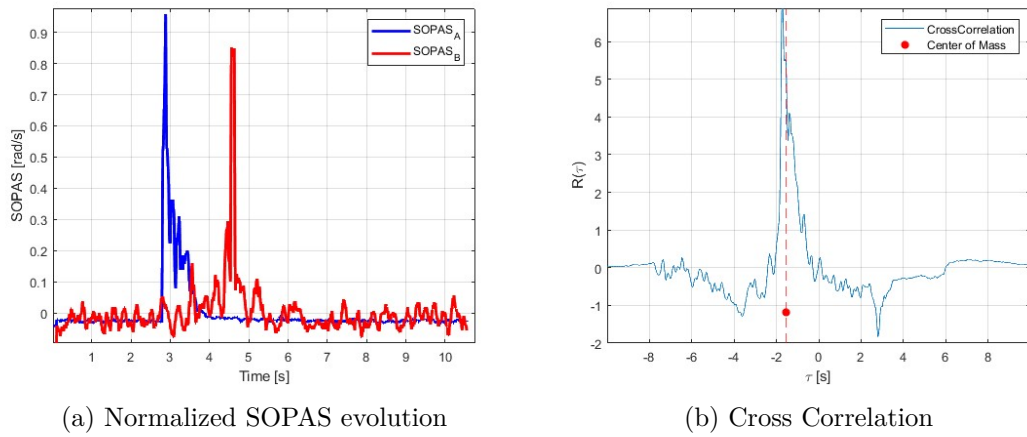


Figure 3.10: Post processing results, $T_{mov} = 0.1 s$

The reported red dot represents the centroid or the barycenter of the cross correlation main peak and its position on the x-axis (X_c) defines the time that the event took to cross two fibers. For sake of clarity, the formulas employed to compute the centroid

position are illustrated in Equations 3.4 and 3.5:

$$X_c = \frac{\int_{X_p} x \cdot f(x) dx}{\int_{X_p} f(x) dx} \quad (3.4)$$

$$Y_c = \frac{\int_{R_p} y \cdot f(y) dy}{\int_{X_p} f(x) dx} \quad (3.5)$$

where X_p and R_p represent the cross correlation main peak sets of samples on the x-axis and on the y-axis, while the equations denominator represents the peak Area on which the geometric center of mass computation was applied. Notice that, in the algorithm, the digital approximation of the integral was employed through the trapezoidal integration method with unitary spacing. As matter of fact, the left plot shown in figure 3.10 displays two main peaks shifted of approximately 2 seconds each other, consequently the centroid position on the time axis in the right plot perfectly validate the expected sensed delay on the fibers. The actual goal of the operation was to characterize the ongoing occurrence by computing the event falling speed, however, it has to be reminded that, to generate a warning, at least two probes must have sensed the same event inside the same time slot, otherwise no alarms and evaluations were returned. Obviously, the velocity has been computed knowing the optical paths distance and following the perfectly known formula showed in Equation 3.6:

$$v = \frac{s}{t} \left[\frac{m}{s} \right] \quad (3.6)$$

Observation 4 The algorithm behaves as a function of the two main parameters T_{mov} and ω_{th} . Indeed, the two parameters are strictly correlated, because the more the SOPAS signals are smoothed the more their peaks intensity will be reduced and the system threshold could miss some events detection. As proof of this concept, Figure 3.11 illustrates the single events detection maps obtained for each of the dangerous occurrence simulated on the reduced scale model. Notice that the showed results were all obtained by the T3 fibers configuration.

The figures reproduce the overall detection performances obtained as a function of the w_{th} and T_{mov} parameters. Consequently the green areas represent correct detection evaluations while the red areas represent the unwanted outcomes, therefore missed detection and false alarms. More precisely, the red area under the green one is mostly caused by FAs, because the threshold value is so low that the noise oscillations triggered an alarm as well. On the contrary, the unsafe upper zone is characterized by MD due the high values of threshold and average. Moreover, it is visible that the size of the safe areas increased with the intensity of the events, while it shrinks with the increase of T_{mov} and the reduce of w_{th} , because the averaging window increased as well and the SOPAS trends were slightly more lowered. Notice that the reported detection maps were obtained by sampling at a f_s different from the one employed on the current Thesis, therefore the showed T_{mov} and w_{th} parameters were not used as starting data-sets of the next experiments because not perfectly suitable with the work purposes.

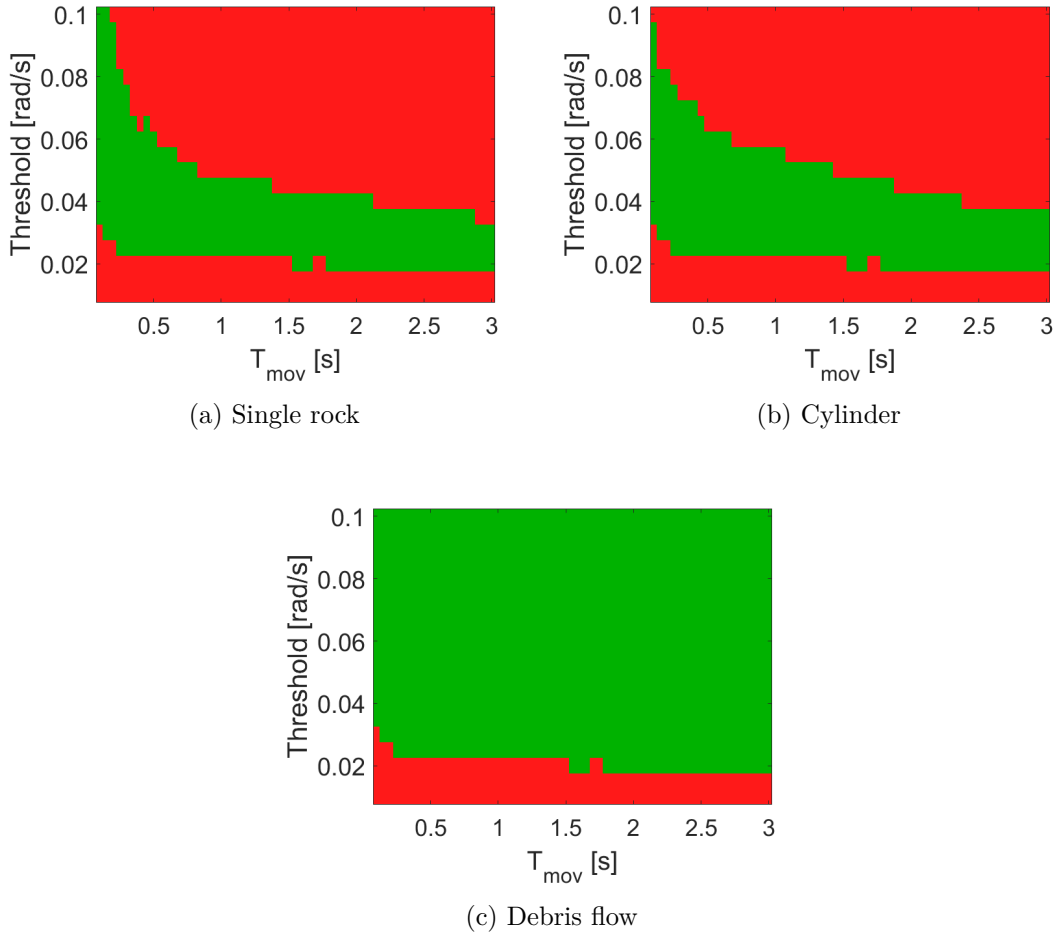


Figure 3.11: T3 events detection maps (Pictures taken from [13])

3.2 Two-Fiber Detection System

After having explained all the performed DSP operations, some real simulations on the downhill side model are reported and commented. The two-fibers setup aimed to return an initial validation of what executed until now and especially to compute the downfall speed of the generated events. In the reduced scale system (Fig.2.3), two different positions of the mountain slide were accounted, therefore the experiments were executed by monitoring the fiber rings arranged on the top and on the bottom of the model (Z_s and Z_i) at the same depth. The three events generated (SR, C, DF) were rolled down from the top of the structure and blocked once that they overcame the monitored areas. Since the fibers were installed 2 meters apart, the expectations were to obtain two similar SOPAS trends separated by the amount of time needed by the risky occurrence to cross the space between the covered areas. The first simulations were performed on the Z_1 fibers and the results are reported in Figure 3.12.

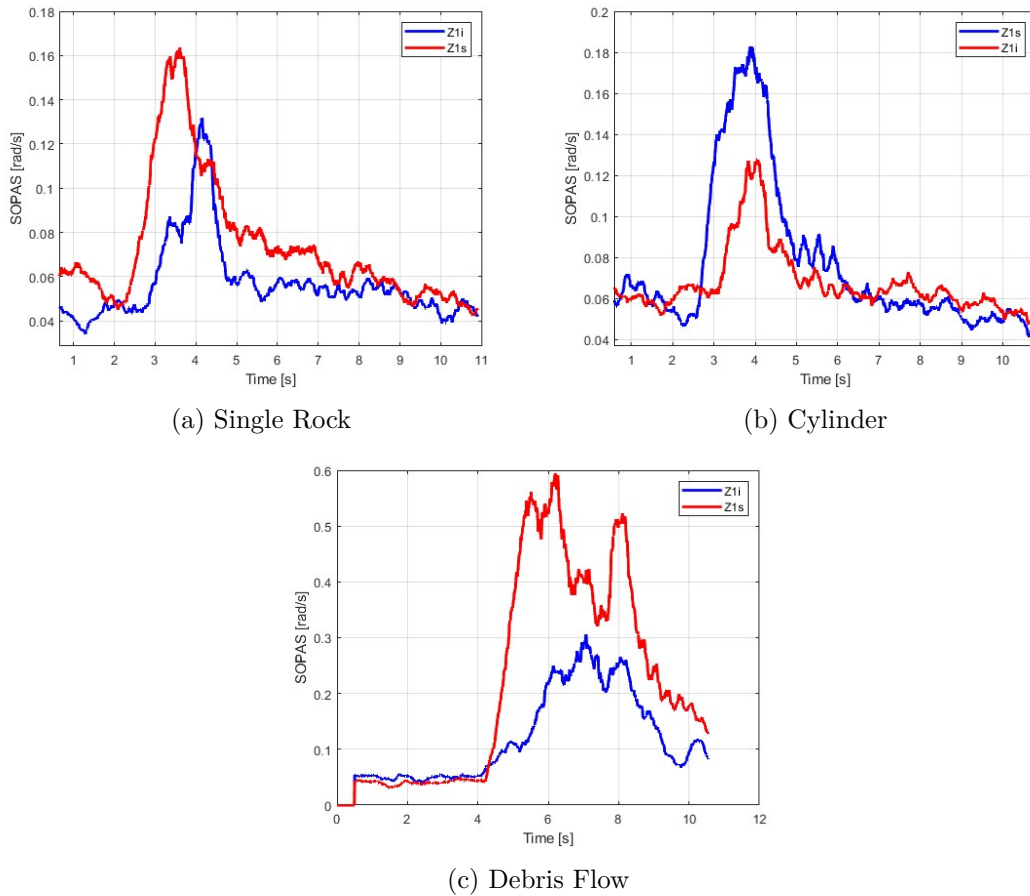


Figure 3.12: Events SOPAS: Z1s and Z1i, $T_{mov}=0.5 s$

All the simulations were able to correctly detect the dangerous events, but the results didn't fully correspond the expectations and what obtained was not always clear. Nevertheless, the observations extrapolated are below reported:

1. both the trends showed common peaks at almost the same time instant. For instance, in the top right image (single rock) when the red line was at its summit also the blue one exhibited a spike. There seems to be a common events perceived by both;
2. the marks seemed to rise and fall simultaneously, especially in the cylinder and in the debris simulations;
3. the first curve to move was also the last that to get the rest condition;
4. one of the two SOPAS evolution was always bigger than the other, even if they have been evaluated at the same depth;
5. the duration of the sensed events depended on the generated source of vibrations, therefore the debris flow lasted more and had an higher peak amplitude with respect

to the single rock simulation.

The third observation was highly unexpected and one possible answer could be encountered in the fourth one, while the first two of them stated almost the same reflection. The same results has been obtained in other simulations, that are not here reported to not be repetitive, but can be found in Appendix A. As a consequence, it was thought that the introduced mechanical vibrations triggered both the fibers at the same time, bringing to an unwanted system performance. To demonstrate it, in Figure 3.13 are reported two simulations in which the event was stopped before it reached the second fiber or it was started from the middle of the ramp in order to cross over only the last fiber ring of the model.

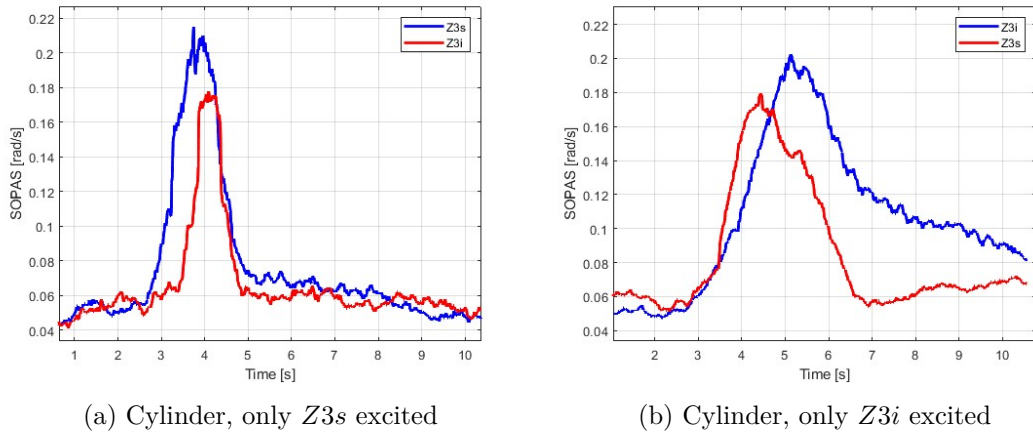


Figure 3.13: SOPAS evolution on single fibers: $T_{mov}=0.5 s$

From the images, only one peak should be evident in the SOPAS trend, because the events have been directly generated on single sections of the model. However, both the fibers sensed the cylinder and an alarm message was returned instead of returning a false alarm. It is now clear that the two fibers interfered one each other and that the system did not allow independent evaluations from the different sections of the model.

3.2.1 New Downhill Model and obtained results

In order to overcome the system intrinsic vibrations impairments, a new experimental mountain model was employed. The goal was to produce simulations on which the fibers evaluations didn't interfere each other, in order to monitor sections of the model that generated independent results. Therefore, a small ramp was inserted in the system and it was placed above the previous one (Fig.2.3), being careful to not connect them in some way. The new slide was 1 m long and 0.4 m wide, with an inclination slightly higher than the previous one. The only fiber present was arranged in a serpentine layout in order to cover the entire structure, however, it was not buried inside the soil, but it was only covered by a soft material that aimed to attenuate impacts. The new setup based on the already present structure plus the small ramp is illustrated in Picture 3.14.

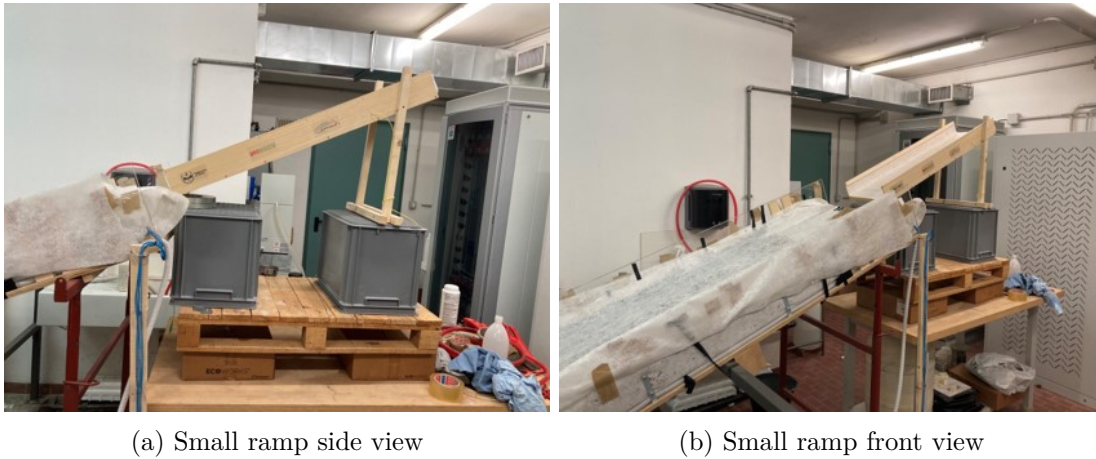


Figure 3.14: New downhill Model

Notice that all the plots inserted in Section 3.1 referred to outcomes obtained with the just described new setup. Before analyzing the processing results with the new configuration, some consideration are introduced:

- the obtained arrangement did not match perfectly the behaviour of a real gully because, of course, the monitored sections of a mountain are not totally independent, even if the probes are positioned far from each other. However, it was thought that the new configuration was more reliable and realistic than the previous one, on which the fibers have been erroneously triggered simultaneously by the same event.
- the soft layer that covered the small ramp was clearly not effective as the layer of the real model was, therefore only single rock events (SR) have been simulated on it and as a consequence only the most superficial (Z3) fibers configuration of the big slide were used.
- the optical paths monitored in the next simulations were the one inside the new structure (called Tm) and the deepest bottom ring pattern of the previously used

model ($Z3i$). In this way, the expected SOPAS trends should be independent each other.

Therefore, the working conditions of the new model and the resulting fibers independence were tested by exciting individually both the ramps, so the outcomes are reported in Figure 3.15.

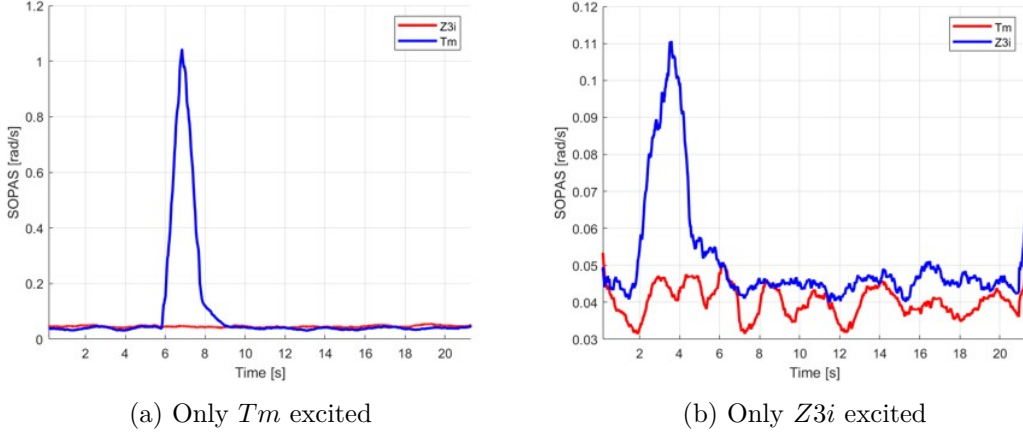


Figure 3.15: SOPAS trends, $T_{mov}=1 s$

From the images two main reflections stood out: the first was that the two sensed optical signals did not have any common event in their SOPAS trend, so they were successfully independent. The results were even more clear if compared with the plots illustrated in Figure 3.15, on which both the trends shared peaks when the top or the bottom sections of the big model were stressed. The second thought was that the peaks levels of the illustrated SOPAS were, as expected, clearly not equal, even if both the fibers have sensed the same single rock event. The reason behind this strange behaviour was the soft material that covered the fiber inside the small ramp, therefore the simulations on Tm were much more sensitive to mechanical vibrations with respect to the other path. Consequently, the solution employed was to normalize their trends in the computation of the correlation, in order to generate peaks with almost the same amplitude. The normalization was applied on both the fibers SOPAS evaluations using the formula illustrated in Equation 3.7¹ and some examples of its impact are shown in Figures 3.16 and 3.17.

$$\omega_{A,norm} = \frac{\omega_A - \bar{\omega}_A}{\max(\omega_A)} \quad (3.7)$$

Notice that the equation was inserted only to compute the correlations plot, therefore the detection algorithm has been employed on the not normalized SOPAS values. However,

¹'A' stands for fiberA

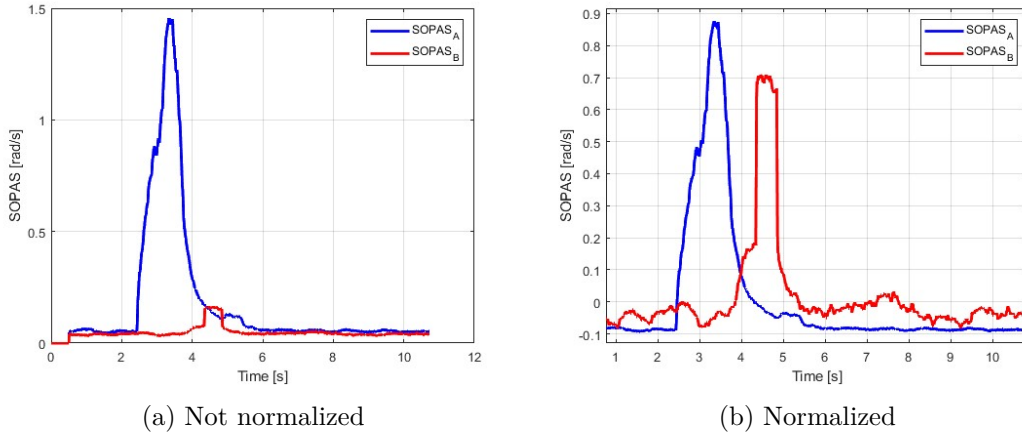


Figure 3.16: SOPAS evolution, $T_{mov}=0.5 s$

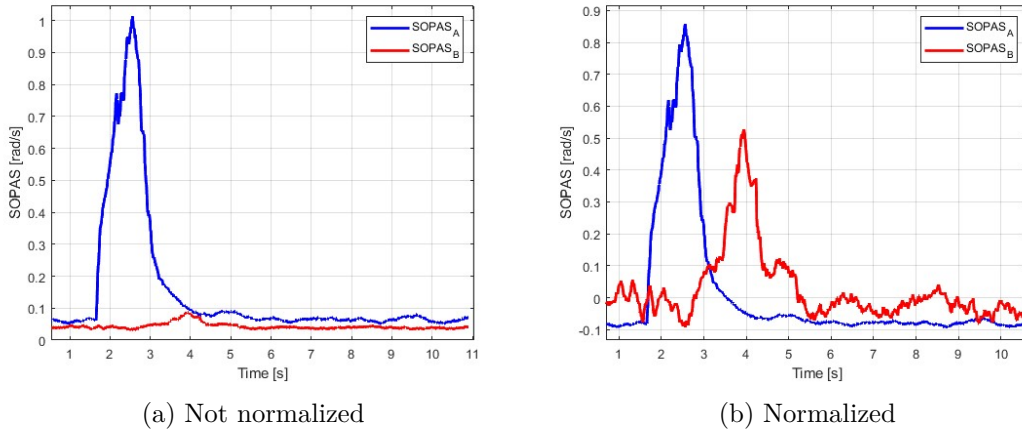


Figure 3.17: SOPAS evolution, $T_{mov}=0.5 s$

the operation introduced some small shifts in the computation of the final parameters and the simulations accuracy slightly decreases.

In addition, before performing the real detection tests, the fibers noise floor level was monitored in order to detect its maximum amplitude and to properly select the required SOPAS threshold to be used to correctly generate the alarms. To do it, a long acquisition was simulated, More precisely it lasted approximately 80 s and no event was generated (look Fig.3.18), in this way the displayed angular speed variations were provoked by the noise only.

Finally, the performances of the system were validated inserting also a 10 km spool of SMF on one of the two optical paths, in order to test a real implementation of the fibers on a wide monitored area and to prove the insensitivity of the system to the fiber length. The

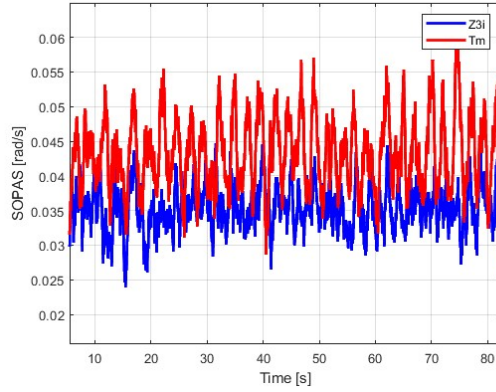


Figure 3.18: Fibers noise floor, $T_{mov}=0.5 s$

actual setup is summarized briefly in Figure 3.19, considering that the blue line crossed the tiny and independent ramp instead of the top area of the previously used model.

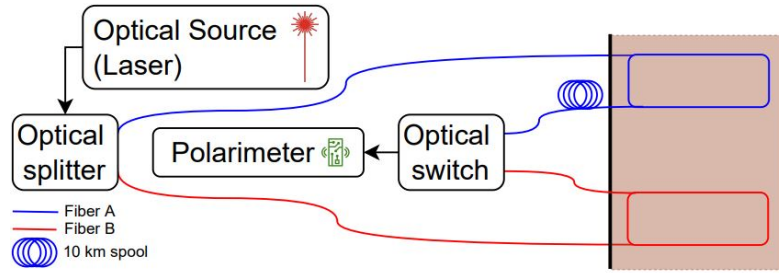
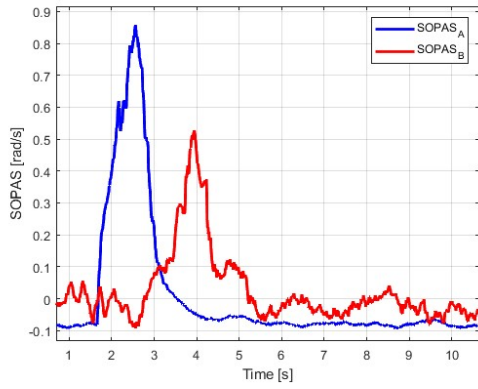


Figure 3.19: Simplified setup of the two-fibers system

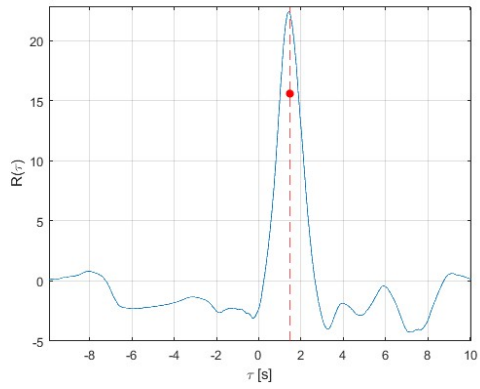
Therefore, in Figure 3.20 and in Table 3.2 are reported the outcomes of some final simulations performed on the two-fiber detection system with independent models. Thanks to the normalization, the cross correlation plots showed a clear peak slightly shifted to the right from the zero value in the x-axis, while the red dots represent their center of mass, which is the time that the SR took to cross the 3 m distance that separate the monitored fibers. The images refer to the test number 1,5,7 in the Table 3.2 and it can be noticed that the SOPAS traces are consistently delayed by values that coincide with the centroids evaluations in the correlation plots. Moreover, the slight variations of the computed estimates have been produced by the different shapes and paths of the single rocks during the simulations.

In the end, the obtained parameters returned an average delay of 1.41 s, at a consequently speed of 2.13 m/s (in average).

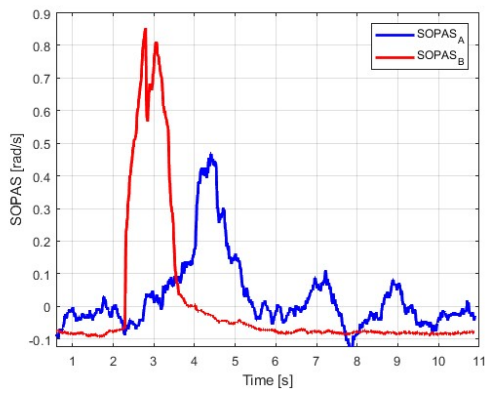
To conclude, the purpose of the simulation was reached successfully, therefore when the fibers sensed the same event the algorithm returned correctly an alarm message and the



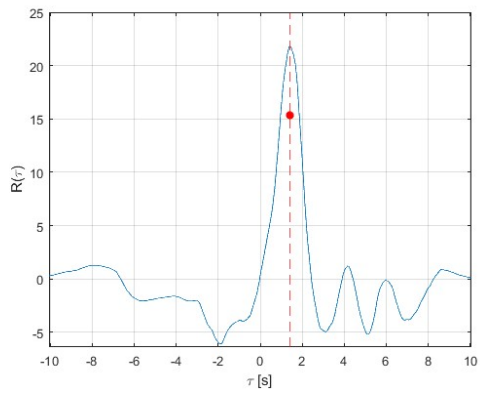
(a) Normalized SOPAS



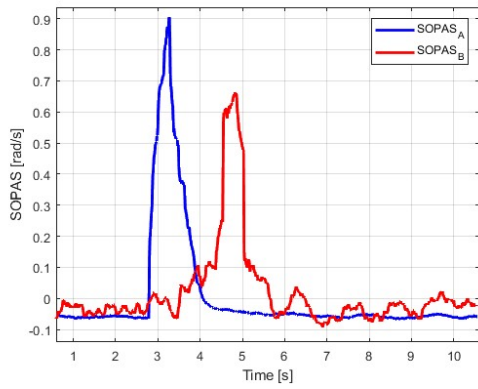
(b) Norm. cross correlation and its centroid



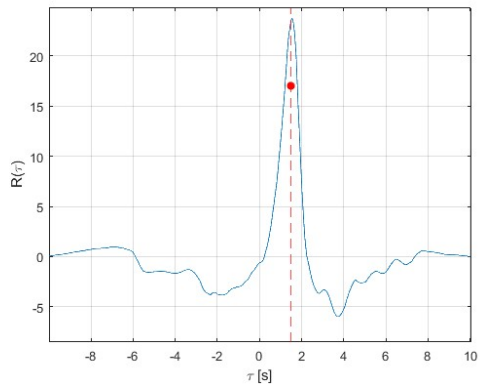
(c) Normalized SOPAS



(d) Norm. cross correlation and its centroid



(e) Normalized SOPAS



(f) Norm. cross correlation and its centroid

Figure 3.20: Offline experiments: $\omega_{th}=0.08 \text{ rad/s}$, $T_{mov}=0.5 \text{ s}$

estimates needed to characterize the the occurrence. Otherwise, if no events or not-dangerous ones occurred, no actions were displayed.

Test	Delay [s]	Speed [m/s]
1	1.465	2.046
2	1.327	2.260
3	1.363	2.199
4	1.629	1.840
5	1.408	2.129
6	1.272	2.357
7	1.470	2.039

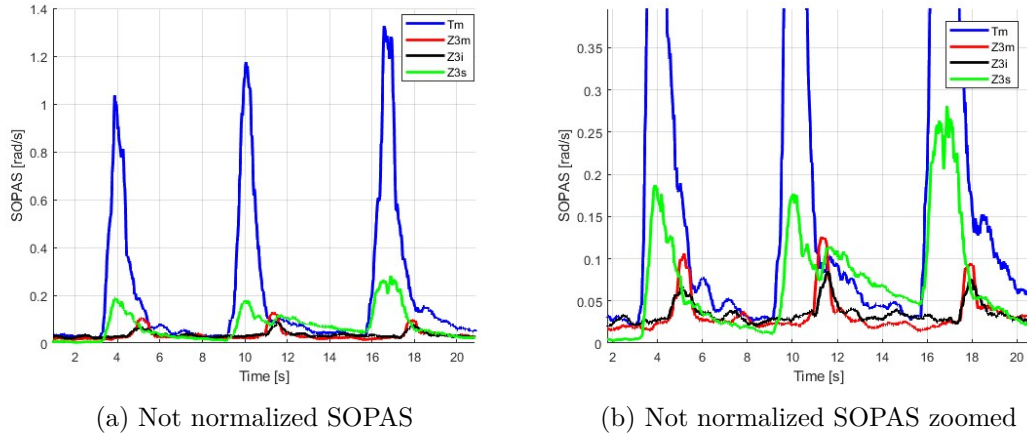
Table 3.2: Delay and speed evaluations

3.3 4-Fibers Implementation

Finally, some acquisition on a 4-fibers detection system were tested. The goal now was not to enhance the detection algorithm and its estimate, because it was already done, but to demonstrate by a new point of view the impairments introduced by the 3 m model on the SOPAS evaluations.

The experiments performed consisted in some longer acquisitions (~ 20 s) on which 3 single rocks events were generated and delayed by 5 s each. In addition, all the fibers present in the final setup were monitored, therefore the one inside the small ramp Tm and the ones inside the long ramp, Zs , Zm and Zi . Obviously, due to the SR occurrence, the Z3 optical pattern configurations were used, in order to sense motions at 1 cm deep in the large model. Remark that, to generate four optical paths, a cascade of two splitter was inserted after the one already present in the two-fibers system (look Figure 2.29).

Then, Figure 3.21 shows the obtained 4-fibers SOPAS evolution in time:


 Figure 3.21: 4-fibers SOPAS evolution $T_{mov}=0.2$ s

Notice that the T_{mov} parameter has been slightly reduced in order to guarantee a better visualization of the outcomes inside the plots. Consequently, the four traces trends are

perfectly visible in the pictures, and the Tm fiber on the small ramp sensed much higher peaks of the SOP variation speed with respect to the other three sensors, that showed similar and consistent evaluations. As expected, the $Z3s$ ring on top of the long model did not produce a perfect 'bell' shape SOPAS as the small ramp did, but something coherent with the fibers arrangement and therefore its behaviour decreased smoothly along the slide as soon as the vibration source moved out from the monitored section. Furthermore, for all the three SR simulations, the fibers $Z3m$ and $Z3i$ sensed each event simultaneously, highlighting again that the optical paths along the long ramp interfered each other. Lastly, the normalized cross correlations of the fibers $Z3s$, $Z3m$ and $Z3i$ with Tm was analysed, with the purpose of computing the time distances between the buried probes with the one installed on the small ramp. The outcomes are reported in Figure 3.22.

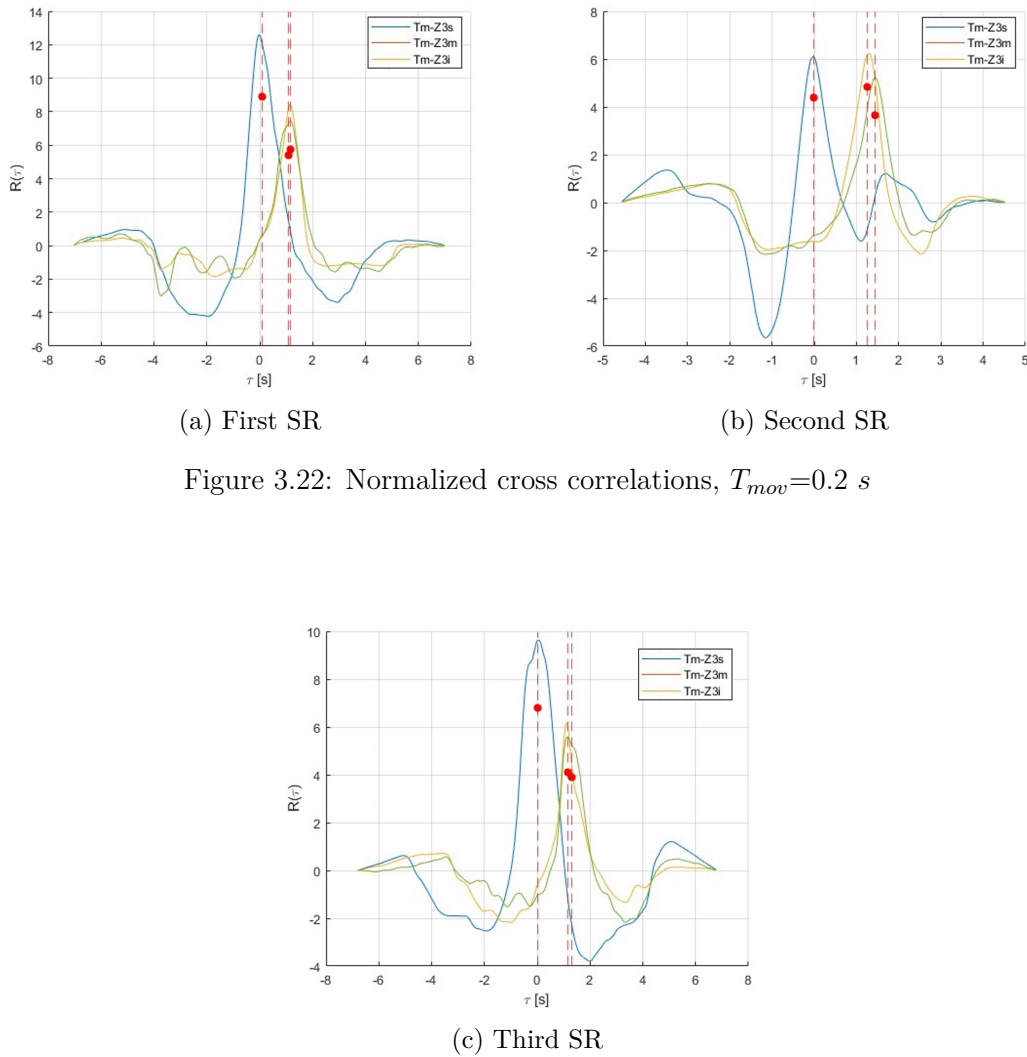


Figure 3.22: Normalized cross correlations, $T_{mov}=0.2 s$

Figure 3.22: Normalized cross correlations, $T_{mov}=0.2 s$

The three plots showed very similar results, especially the middle and the bottom fibers on the long model returned centroids at the same positions on the x-axis, stating that they actually sensed the same event at almost the same instant. Moreover, the correlation between Tm and $Z3s$ gave back a zero delay evaluation on all the three SR events, demonstrating that the normalization operation introduced small impairments in the final parameters estimation when the fiber delay is very small.

3.4 Summary and conclusions

In conclusion, the developed post processing algorithm worked correctly and the probability of false alarm generated by non dangerous event should be almost erased with the employment of two (or more) fibers in the sensing system. Therefore an alarm message was generated when a dangerous event ($\bar{\omega} > \omega_{th}$) was sensed on both the optical paths. This condition enabled also the possibility to characterize and localize the events by estimating which fiber sensed the rockfall firstly and by computing at which speed the occurrence was happening. Moreover, the application of an optical switch allowed a reduction of the cost by reusing the expensive components, for instance the optical laser and the polarimeter. As matter of fact, all the obtained outcomes in the chapter are summed up in an article written for the OFC conference that unfortunately was not submitted.

Lastly, the impairments introduced by the normalization function are not a problem on real simulations, because, contrary to what was simulated in the work, on a mountain gully the fibers are buried inside the same field and consequently they should sense the events with the same intensity.

Chapter 4

Real-Time implementation and related Measurements

Last but not least, after the initial parameters setting operation performed in Chapter 3, an in depth description of the final algorithm that will be actually employed in a real-time mountain scenario is provided. In the work, the real-time operations aimed to sense and process, with the same f_s of the offline algorithm, one measurement at a time, in order to generate an alarm message as fast as possible whenever a dangerous event was incurred. Therefore, contrary to the post-processing algorithm, the only latency introduced was due to DSP (mostly due to filtering), that must be as rapid as accurate. Next sessions will deal with the new processing block diagram employed, showing in detail the operation performed and the results obtained.

4.1 Algorithm employed and differences with the offline method

The main features of a real-time acquisition and the expected goals are:

1. Reliability: in a hazardous mountain environment, the faster is the evaluation of an alarm condition the safer will be the employed system.
2. Accuracy: it depends on the probability of false alarm or missed detection, which must be the lowest possible
3. Long activity period: the algorithm should be able to perfectly work for extremely long measurement periods, therefore an accurate analysis of the memory storage space occupied must be done.

The setup tested in the RT detection system was the one illustrated in Figure 2.28, therefore the optical switch solution with the operational amplifiers was employed. However, differently from the post-processing simulations, the switch commutations were controlled

through Matlab on the user PC, which every ~ 5 ms sent a different bits sequence in order to control the device and to alternate the sensed fiber with a switching rate of approximately 200Hz (as reported in Section 2.4). Moreover, the downhill model based on two independent ramps (Fig.3.14) was immediately used, and accordingly, the correlation outcomes were evaluated considering the normalized SOPAS, in order to properly compare on the same amplitude level the two ramps measurements. After having reported some initial considerations, the RT algorithm block scheme is illustrated in Figure 4.1 and described in the following steps:

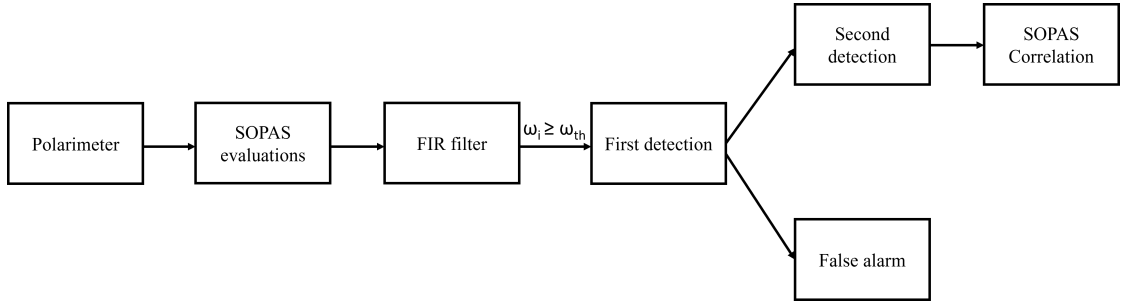


Figure 4.1: Real-time block scheme

1. Polarimeter:

The Stokes parameters extrapolation in the RT algorithm was performed through Matlab by reading the polarimeter internal register. Especially, there are three specific addresses that contains, sample by sample, the normalized values (on the Poincaré surface) of the S_1, S_2 and S_3 parameters. Therefore, every T_{sw} seconds, the probe fiber was switched, the reading operation was triggered, a measurement was acquired, and the processing operations started. This means that all the DSP was applied sample by sample. The obtained acquisitions should be very similar to the ones obtained in the PP algorithm after downsampling (in Section 3.1), therefore the processing operations are greatly reduced.

2. SOPAS Evaluation and FIR filter:

These blocks are the same of the previous configuration, therefore the Equations 3.1 and 3.2 and the filter operations were applied to obtain a smoothed SOPAS evolution with smooth window T_{mov} , i.e the delay introduced to perform the average operation. The evaluations obtained will be then compared with the defined threshold value for the detection of dangerous occurrences. Moreover, the algorithm allows a RT plot of the evaluated not normalized SOPAS and the results are shown in Figures 4.2 and 4.3, where each dot represents one SOPAS processed (smoothed) sample. Both the images illustrate an experiment on which two SR events were rolled down from the model five seconds apart. The experiment reported in Figure 4.2 was performed on the system with separated ramps (Fig.3.14), therefore fibers T_m and $Z3i$ were tested., Accordingly, for each SR simulation, two independent peaks of the SOPAS traces are perfectly visible. On the contrary, the test pictured in Figure 4.3 was

performed on the original 3 m long model, and the structure impairment due to the outcomes dependency of the $Z3s$ and $Z3i$ fibers is again highlighted. Moreover, the $Z3s$ fiber (red trace) is always the first to sense the event but also the last to capture it, due to the intrinsic mechanical vibrations generated by the model.

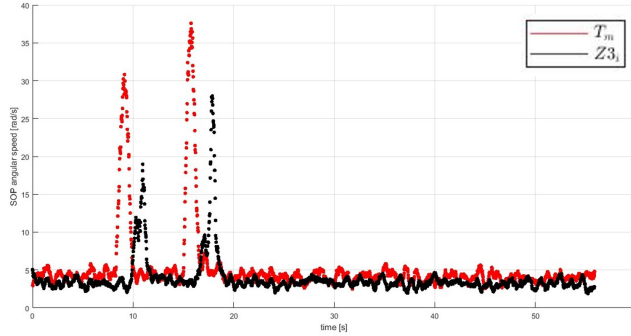


Figure 4.2: Experiment on Tm and $Z3i$ fibers, $T_{mov}=0.2 s$

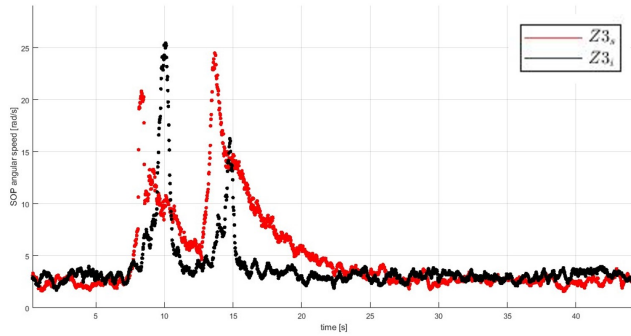


Figure 4.3: Experiment on $Z3s$ and $Z3i$ fibers, $T_{mov}=0.2 s$

The real time plots operation introduced a processing latency that overcame the time requirements, however it does not represent a limitation because in the actual application of the detection algorithm the images are never displayed during the measurements, but only when an alarm occurs and the switch speed is preserved. Consequently, the main outcome of these first RT experiments was the possibility to monitor and plot the trends of the SOP angular speeds just like in the offline method, therefore similar delay and speed outcomes are expected from the developed algorithm. The reported simulations lasted almost 60 seconds therefore did not incur in memory problems, nevertheless, if the system has to monitor a mountain gully for many days (or months), the SOPAS samples that the PC will store could be unbearable. Therefore, from now on, a limited number of evaluations will be stored, in order to not fill the PC Matlab memory but also to reproduce an accurate correlation of the SOPAS trends.

Finally, an experiment of the timing delay introduced by the real-time plots is reported in figure 4.4.

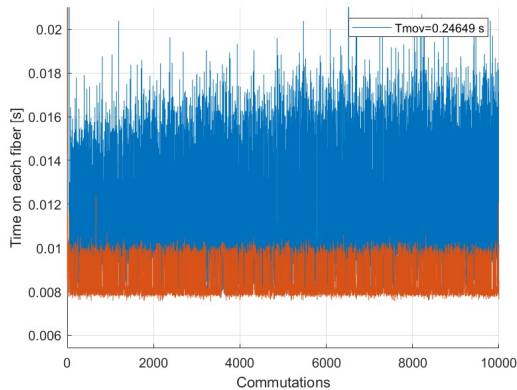


Figure 4.4: T_{sw} with and without RT plots

The picture illustrates in blue the timing required to process and switch the input fiber if also instantaneous plots were displayed, on the contrary, the orange trace represents the time requirements needed to process and iterate the sensed optical path without drowning any evaluation during the measurements. It is clear how the insertion of the graphs in the algorithm highly increased the mean and the standard deviation of T_{sw} , therefore the blue lines oscillates in a range much bigger than the orange ones.

3. First detection:

After filtering, the k -th smoothed SOPAS evaluation was compared with a defined threshold and if $\bar{\omega}_k > \omega_{th}$ a detection of a dangerous event occurred. In the previously described offline method, the experiments had a small time duration and the acquisitions were stored for the entire simulation, without incurring in problems due to the limited storing space. However, the RT algorithm can be employed for very long acquisition periods, and accordingly, an accurate analysis on the Matlab memory usage must be done. The goal was to avoid to store a large amount of evaluations that did not bring any information about the dangerous events, indeed, the sensing analysis were focused mostly on the acquisitions obtained after that a fiber sensed an event. However, to monitor entirely the events dynamic and to not deteriorate the cross correlation performances, an additional moving buffer of length T_{buff} was introduced to store M_{buff} samples immediately before that a fiber recognized an event as possible danger. The new small container size was declared in order to store some seconds of quite SOP before that an event incurred and accordingly aimed to maintain the correlation peak highly reliable. In this way, M_{buff} preliminary samples plus the measurements belonged to the dangerous event were stored and employed to perform the final computations. As well as the FIR filter, therefore when the buffer was filled it stored sample by sample each $\bar{\omega}_k$ by overwriting the oldest acquisitions,

until the first detection occurred. A clear plot of the above described operation is represented in Figure 4.5

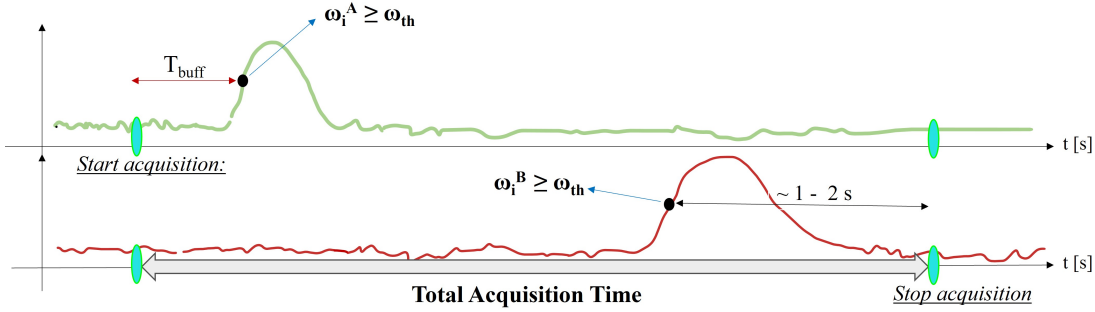


Figure 4.5: Final memory employment

In the image, a simplified example of the SOPAS traces obtained from a 2-fiber detection system and their total acquisition period are reported. More in details, the black dots represent the instants when the SOPAS evaluations obtained from the fibers SOPs pass the set threshold. Notice that, the just described processing block focuses on the instants immediately before that fiberA in Figure 4.5 sensed the event. In particular, it is visible that the storing operation started some seconds (T_{buff}) before that the event occurred on the first fiber. The following processing steps will describe in depth the remaining part of the image.

4. False alarm and second detection

Just like in the offline method, the false alarm and the second detection warning have been managed with a manually inserted timer. Therefore, after that the dangerous event was sensed for the first time, the timer started and once it finished two working possibilities have been defined:

- if the number of detection was still one, a false alarm was generated, the stored SOPAS samples were cleared and the detection counter was reset. Therefore a non dangerous event was detected and the algorithm restarted to monitor the simulated model.
- if the downstream fiber sensed the danger as well, an alarm message was displayed, but the storing operation was continued for a few seconds before processing the results, in order to properly acquire the entire occurrence evolution and to enhance the cross correlation evaluations. This final latency defined the real-time delay introduced by the algorithm in returning the outcomes (not the alarm, the warning message is returned instantaneously). Of course, the more time it saved samples the more accurate were the results. Again, a trade-off between accuracy and delay was needed and it was achieved with a further acquisition of approximately 1 - 2 s. The just described operation is shown in Figure 4.5, and it is visible that after the second detection, the storing operation continued for an additional time to properly monitor the sensed event.

In summary, to properly manage the memory limitations, instead of storing all the available SOPAS information, the RT algorithm acquired and processed only the SOPAS evaluations of the fibers from some instants before the event occurred to some after.

5. Cross correlation

When a dangerous event occurred, therefore when at least two detection were sensed, an alarm message was displayed and the cross correlation computations (rockfall delay and speed) were performed. As in the post-processing mode, the convolution was performed on the normalized SOPAS evaluations, due to the unbalanced sensing amplitude returned by the different ramps (Fig.3.14). Moreover, the time needed by the occurrence to cross two fibers was computed as the centroid of the latter operation, while the event rolling speed was obtained through Equation 3.6. To conclude, the reliability of the algorithm depended on the velocity of reaction with which this last step of the processing block returned an alarm and on the correctness of the results.

Observation 5 Until now, memory managements operations have been applied only on the SOPAS acquisitions. Especially, nothing more than the evaluations belonged to the sensed risky occurrence were stored, increasing the processing speed and avoiding to save a huge amount of data that did not contain any kind of useful information. However, the Stokes parameters (S_1, S_2 and S_3) acquired by reading the polarimeter registers, were stored in a matrix (S) of dimension $3 \times N_{samples}$, where $N_{samples}$ was the number of measurements performed in the experiment and it is enormous if the optical switch have to iterate at a rate of 200 Hz for multiple hours (remark, for each commutation of the optical device a measurement was acquired). Therefore, following Equation 4.1, it is possible to compute the number of saved samples per each Stokes parameter.

$$N_{samples} = t_{tot} \cdot f_{sw} \quad (4.1)$$

For instance, if the experiment lasted 1 day, the matrix contained more than $17 \cdot 10^6$ samples per row. Consequently, memory limitation operation were performed on the Stokes extrapolation as well and a new parameter was introduced (N_{rep}). The method employed consisted in overwriting the S matrix multiple times, in order to allocate in advance a small portion of the available memory and to maintain it fixed with the evolution of the experiment. In such a way, the reading operation from the polarimeter registers will be executed $N_{samples} \cdot N_{rep}$ times, but the employed storage space is dependent only on the first parameter in the just reported formula.

Nevertheless, before overwriting the matrix, the latest measurement per fiber, so \vec{S}^{k-1} in Equation 3.1, was shifted in the first position of the matrix, in order to provide to the next SOPAS evaluation all the required elements (\vec{S}^k and \vec{S}^{k-1}). Figure 4.6 show exactly what was described and performed to limit the memory occupancy in the algorithm.

In particular, the image illustrates a 2-fibers simulation on which N_{rep} was equal to 3, therefore the allocated space was overwritten three times. Moreover, it is visible that the

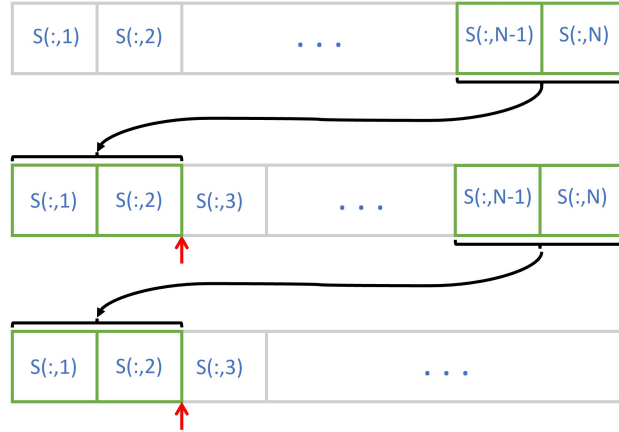


Figure 4.6: Stokes parameters memory management

latest elements stored in the matrix contain the last measurements of $fiber_A$ and $fiber_B$ and accordingly, they are shifted in the first positions of the matrix itself. In this way, the new acquisition can be stored starting from the red arrow, therefore from the first cell just after the shifted ones, and a new SOPAS evaluation can be immediately returned. In addition, to validate the results, Tables 4.1 and 4.2 illustrate two experiments on which the time evolution of the storage space in Matlab was monitored.

Experiment A	Memory occupation [MB]
After Reboot	2416
After 8 min	2893
After 10 min	2893

Table 4.1: Experiment A - Storage space occupation in time

From the first Table, it is visible that after the platform reboot and the matrix initialization the memory occupation didn't change in time, therefore the expected space limitations were actually applied and the algorithm could iterate as much as desired. Furthermore, the second chart reported the storage space occupied at the end of the simulation, therefore after approximately 10 minutes of acquisition. However, differently from Experiment A, in this analysis an event occurred and the SOPAS evaluation were stored as well as the S matrix. For this reason, the last term of Table 4.2 is slightly bigger than the one in Table 4.1. Finally, the requirements needed to perform real-time long acquisitions have been achieved though the devoted analysis on the variables memory management, even though the operation described in Figure 4.6 introduced a tiny delay in the developed algorithm. However, it was demonstrated that this latency did not produce any problems for the sensing purpose, being an event that occurred once any $N_{samples}$.

Experiment B	Memory occupation [MB]
After Reboot	2399
Var. Initialization	2840
End	2957

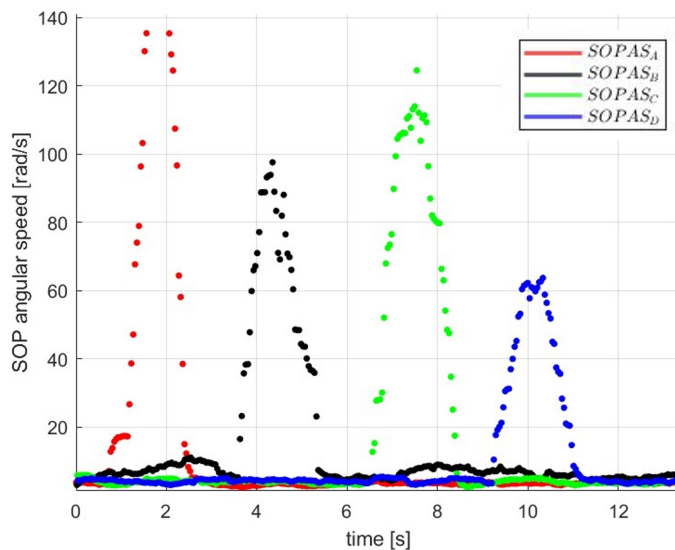
Table 4.2: Experiment B - Storage space occupation in time

4.2 4-fibers experiments

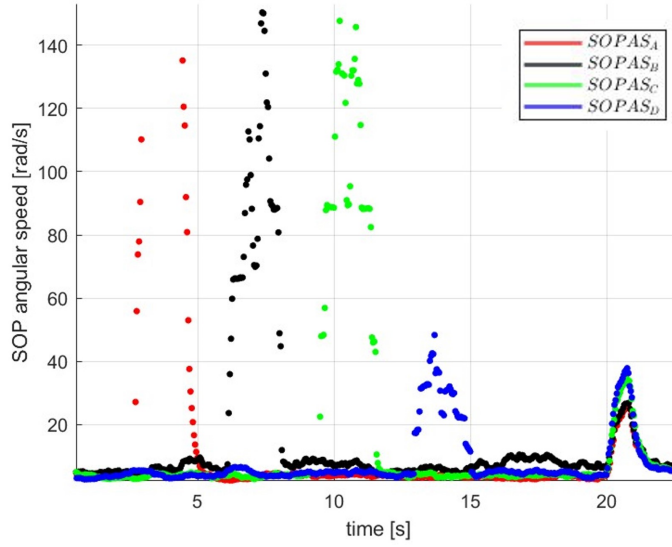
Before evaluating the results and the performances of the RT algorithm, the above described processing steps were simulated in a 4-fibers detection scenario as well.

The purpose of these experiments was to test the new developed method and to prove its correctness, and consequently, the mechanical vibrations introduced on the optical paths were generated manually without the employment of the 2 ramps model previously used. Notice that, in order to correctly monitor the available input ports of the optical switch, the experimental arrangement illustrated in Figure 2.29 was again employed.

The obtained SOPAS traces are illustrated in Figures 4.7 and 4.8. In the plots, a propagation of an event on the sensed fibers was simulated, moreover, each evaluation of the SOP angular speed after the smoothing step (FIR filter) of the processing block was instantaneously displayed, therefore dotted lines were returned instead of continuous ones.


 Figure 4.7: A - RT 4-fibers SOPAS plot, $T_{sw}=10$ ms

From the images it is clearly visible the evolution of the event on the optical cables and which fiber out of the available one was shaken, consequently, when a SOPAS trend moves the others remained approximately fixed, confirming the exactness of the algorithm. In

Figure 4.8: B - RT 4-fibers SOPAS plot, $T_{sw}=10 \text{ ms}$

addition, Figure 4.8 illustrates a common peak at approximately 20 seconds in the time axis. In this case, the SOPAS traces behaved again correctly, because differently from the previous reported peaks, the last one was generated so that all the optical sensors sensed it in the same instant. Remark that, in the RT setup, the configuration with the electrical amplifier was used and the minimum achieved T_{sw} was about 8 ms. However, if one measurement out of four belonged to the same fiber, the actual sampling rate per probe became approximately of 31 Hz. Therefore, the reported plots are an other validation of the spectrogram in Figure 2.14 in Section 2.4, where it was stated that monitoring the system at a low rate does not lose information about the incoming event. Indeed, in the example just described, the common vibration at the end of the simulation was equally sensed by all the employed optical fibers.

4.3 RT evaluations with the developed GUI

The last step of the work focused on the develop of a graphic user interface able to provide an easy method to set the algorithm parameters (e.g. T_{mov} and ω_{th}) and to display the final SOPAS traces, correlation plot and the delay and speed outcomes. To do it, again the Matlab platform was employed and the obtained application is reported in Figure 4.9.

The GUI image is composed by toggles, buttons, empty variables and charts and it's divided in two parts: the upper half of the application is characterized by all the inputs parameters that should be defined before the experiment, while the bottom half represents the outcomes, therefore the plots and the evaluations. This results will be displayed once that a dangerous event is actually sensed. After that, the next lines are devoted to an in depth description of all the working possibilities offered by the graphic interface and to a

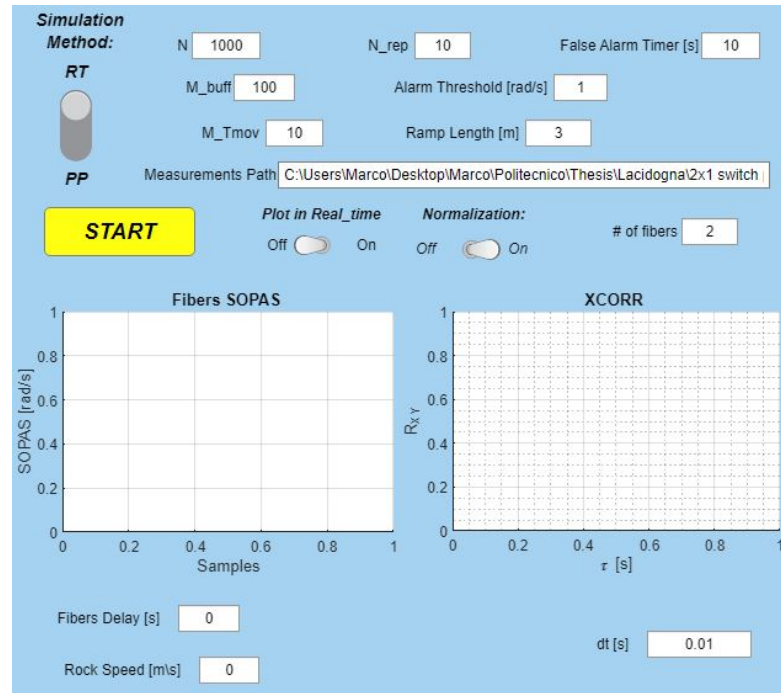


Figure 4.9: Graphic user interface

remark of the set parameters.

- Start: It is a button, after it was pushed the acquisition started following the set up conditions and values;
- Toggles: They are switches and select one out of two picks. In the application multiple toggles are defined:
 1. Simulation method: it allows to choose the working mode of the algorithm, therefore either the offline or the real-time methods. The first allows to analyse and process an already acquired measurement, instead the latter begins a new acquisition as soon as the start button was pressed;
 2. Plot in Real-Time: it defines the possibility to display instantaneously the smoothed evaluations of the SOPAS computed during the experiment. Of course, a RT monitoring of the sensed traces allows to better visualize the actual SOP inside the fibers, however it introduce a tiny delay. Consequently, this toggle was set to active for prove of concepts experiments, but in a real monitoring system the plots are not displayed, in order to guarantee the fastest sampling speed and accordingly the most reliable alarm generation;
 3. Normalization: this step was already dealt with during the previous chapters and it performs the mathematical operation illustrated in Equation 3.7 on the SOPAS evaluations. It was applied in order to compare on the same amplitude

level the fibers evaluations coming from different sections of the mountain slide model;

- Empty variables:
 1. N and N_{rep} : the first defines $N_{samples}$, therefore the space allocated in the Matlab memory needed to store the polarimeter measurements, while the second defines how many times the storage slot should be overwritten to avoid further allocation of the available space. Moreover, they together characterize the number of iterations performed by the optical switch and consequently the total acquisition time;
 2. False alarm timer: after the risky event was sensed by the first fiber, a timer was started, and if no other optical sensors have detected the occurrence inside the defined time range a false alarm message was displayed, because there were no object rolling down of the mountain slide and an occasional non-dangerous event occurred;
 3. Buffers lengths: M_{buff} characterizes the amount of information stored before a detection, the higher it is, the more accurate will be the cross correlation plot but the higher is the storage occupancy. While $M_{T_{mov}}$ describes the SOPAS averaging operation, therefore coincides with the length in samples of the applied FIR filter;
 4. Alarm threshold: it corresponds to ω_{th} and defines the limit value above which an event is dangerous;
 5. Measurements path: it is employed for the post-processing operations and consists in the .bin file that contains the measurement to be processed;
 6. Ramp length: it is the distance between the monitored optical paths. In the experiments, it was the distance between fiber Tm and $Z3i$. This parameter will be useful to compute the landslide rolling speed through Equation 3.6;
 7. Number of fibers: it is the amount of optical sensors employed in the system, the developed algorithm and the experiment arrangement changed dependently on this parameter.

Finally, the charts in the application illustrate the SOPAS evolution in time and their cross correlation trend. Below them, the delay that the event takes to cross at least two fibers and the resulting rolling speed will be displayed as fast as possible.

After the description of the employed application, RT experiments based on a 2-fibers detection system were simulated and the outcomes are reported in Table 4.3. The reported chart is clearly consistent with the expectations if compared to the evaluations obtained with the offline method and reported in Table 3.2. Just like the previous experiments, only SR events were simulated, in order to not damage the fiber on the small ramp at the top of the model (look at Figure 3.14), because it was not protected by the soil except for a thin layer of geotextile. Moreover, the slight variations of the computed speeds were dependent on the different shapes and paths of the rocks employed.

Test	Delay [s]	Speed [m/s]
1	1.26	2.38
2	1.60	1.88
3	1.34	2.24
4	1.56	1.92
5	1.03	2.91
6	1.3	2.31

Table 4.3: Delay and speed evaluations

Therefore, the evaluated estimates returned an average delay of 1.34 s, and a resulting speed of 2.23 m/s (in average). These results are perfectly consistent with the 1.41 s latency and the 2.13 m/s speed estimated obtained from the offline experiments. At last, since the experiments were filmed, some snapshots of the user’s PC display are reported. Consequently, in Figures 4.10, 4.11 and 4.12 are illustrated the developed GUI and the real time SOPAS evolution at the end of the simulations, therefore when the dangerous event was properly detected. The left plot of the application and the RT graph coincide, with the difference that, on the GUI, the normalization toggle was active and the evaluated traces were comparable on similar amplitude levels. More precisely, the charts refers on the y-axis to the fibers SOPAS trends in *rad/s* and on the x-axis to the time in *seconds*. Moreover, the same images differs in the amount of noise floor displayed, indeed, in the user interface, memory management operations were applied and the stored SOP angular speed trends started some instants before the first event was detected. In other words, the SOPAS information saved and displayed in the GUI was independent from the RT experiment duration and the resulting amount of noise information dealt with.



Figure 4.10: Experiment A - GUI and RT plots

In addition, it has to be noticed that the RT plots were displayed outside the application because the communication between the GUI and Matlab was too slow if compared with

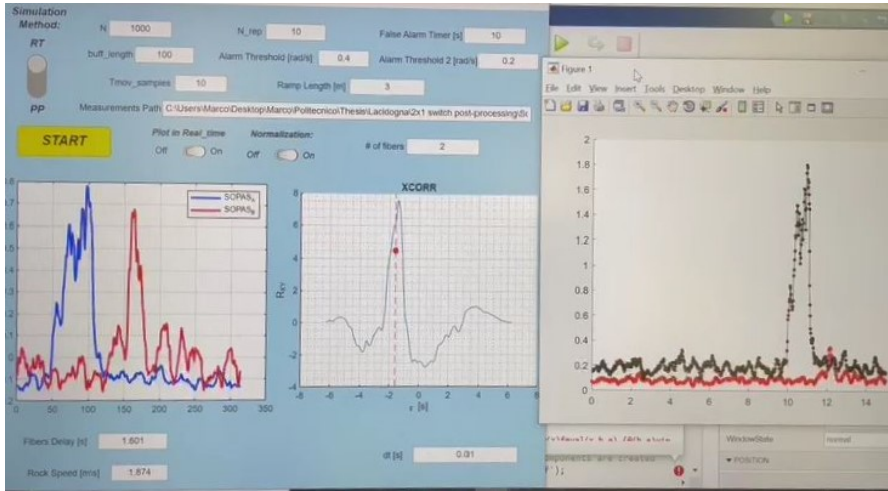


Figure 4.11: Experiment B - GUI and RT plots

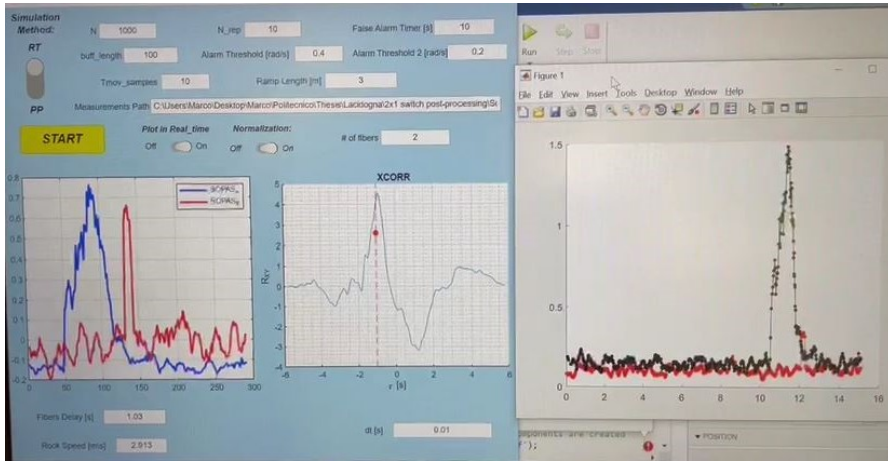


Figure 4.12: Experiment C - GUI and RT plots

the requested optical switching speed. To conclude, the cross correlation plot is displayed simultaneously with the other plot of the GUI at the end of the experiments and its trend appears similar the ones illustrated in Figure 3.20 in Section 3.2.1. For sake of clarity, the main input parameters set before the simulations are shown in Table 4.4. The main target achieved in the final experiments was the time taken by the GUI (therefore the RT algorithm) to return the reported charts and evaluations that characterized the occurring event. This delay was approximately of 2 seconds, therefore it made the developed interface highly reliable because it allowed a fast real-time alarm generation, limited only by some processing operation that aimed to increase the accuracy of the estimated rockfall time and speed.

FA Timer[s]	M_{buff}	$M_{T_{mov}}$	ω_{th}^1 [rad/s]	ω_{th}^2 [rad/s]	Ramp Length[m]
10	100	10	0.4	0.2	3

Table 4.4: RT input parameters

Chapter 5

Conclusions and future developments

Besides being an ultra-high capacity transmission medium, this Thesis proved that the optical fiber is an excellent sensor of mechanical stresses as well. The actual evidence of the employed algorithm correct functioning is indeed represented by the developed GUI shown in Figure 5.1, where both the RT plots and the resulting computations of the dangerous ongoing event are displayed. In particular, the latter results were computed only if a dangerous occurrence was detected by at least two fibers, otherwise the algorithm continued monitoring the quite state of the fiber SOP.

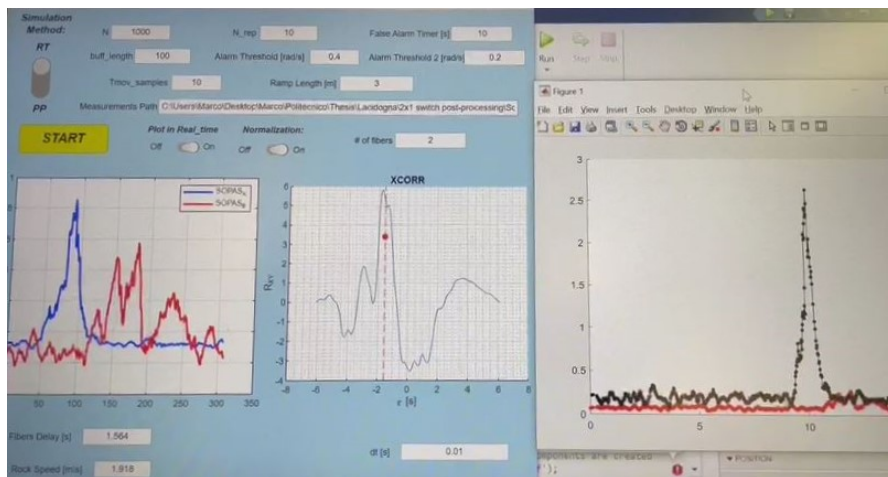


Figure 5.1: GUI and RT plots

Consequently, the advantages and the enhancements of the proposed Thesis, compared to the existing technologies, include:

- the possibility, thanks to the application of the optical fibers, to both monitor a vast geographical area and to employ the interrogator part of the setup at very far distances from the sensed section. The experiments performed in Section 3.2.1 in Chapter 3 were obtained indeed with a 10 km spool of SMF, proving the insensitivity of the system to the distance between sensors and user emplacement. The only limitations induced by the fiber length could be the attenuation on the optical cable, nevertheless the sensitivity of the polarimeter is very low (up to -35 dB), making it impossible for the distances employed to get to an under-range condition.
- the real-time algorithm actually worked and the ongoing vent measurements were displayed with a delay of a few seconds (1-2 s) with respect to the alarm detection. This latency was mainly introduced by the filtering operation in the DSP algorithm and, considering the events real timing constants involved in a mountain scenario, it allows a prompt reaction on the in danger area.
- Accuracy: the experiments returned approximately the same centroid position on the time axis, therefore the time that the rock takes to roll down between the two fibers was correctly estimated. In particular, Figure 5.2 concatenates in a unique 3D plot the correlations curves obtained by processing of five SRs events. The correlation peaks are clear and narrow, allowing an accurate estimate of the fibers time delay.

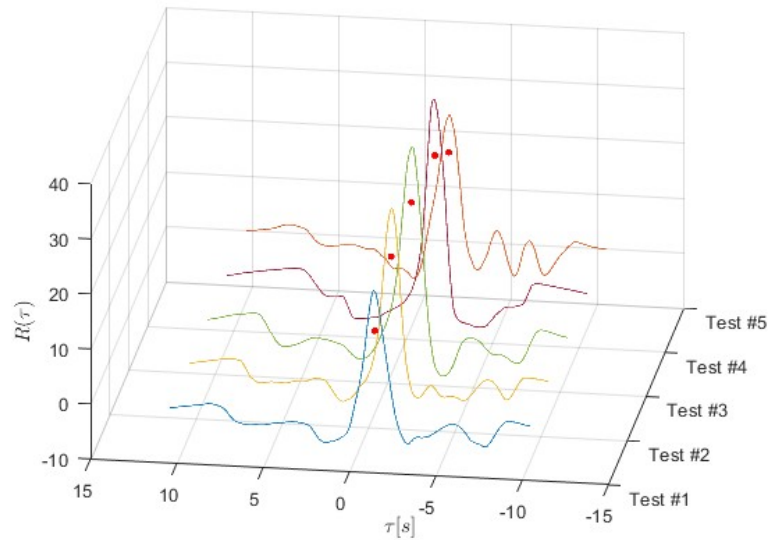


Figure 5.2: Cross correlation curves and centroids between SOPAS on Tm and $Z3i$ for five SR events

- Sensitivity: the developed reduced scale setup was sensitive to all the events tested, from the single rock to the debris flow, and at all the different depths experimented, therefore it will be certainly able to detect also the much more intense real event of the mountain scenario.

- Reliability: the system with one fiber only was intrinsically prone to false alarm generation if a non-dangerous event happened near the probe optical path. Therefore, the implementation of the optical switch and of at least two sensors allowed to obtain more informations about the ongoing event (i.e. events speed and tracking) and to remove the false alarms by generating a warning only when the event was sensed by two fibers.
- Cost-effectiveness: The implementation of the optical switch allowed to share the same costly hardware along multiple optical fiber sensors.
- Lighter data management: a low sampling frequency and the optimized processing algorithm, allowed to reduce the amount of data to be stored and processed, enabling also the employment of the system in endless sensing applications.
- Localization: the evaluated time and speed estimates allowed to characterize in real-time the dynamics of the ongoing dangerous event. This allowed to describe roughly the spatial distribution of the events with reduced costs if compared to the distributed OFSs system introduced in Chapter 1.

However, in addition to this good results, some limits of the work have to be reported. In particular, the reduced scale model is different from an actual deployment of the system in a real large scale gully. In fact, in real world situation, the rockfall events would be much longer in time (tens of seconds at least) and much stronger in intensity. Consequently, the obtained SOPAS evaluation may not follow the classic "bell" shape analysed in the Thesis, but it may return a trend similar to what is pictured in Figure 5.3.

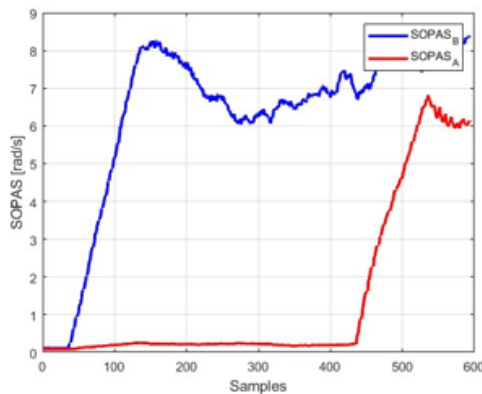


Figure 5.3: Assumed real SOPAS trends

Notice that, the just reported example was not tested in a real mountain environment, therefore the mechanical vibrations were simulated by touching heavily the probe fibers for a duration of tens of seconds. As reported in Chapter 4, the reported SOPAS trends were computed up to some seconds after an alarm was generated, and the resulting correlation computations were estimated on them. However, due to the events long duration, the evaluated SOPAS traces took time to reach the quite state, therefore to show a descendant

behaviour, and the obtained correlation curves were no more easily analysed and the DSP point of view became more critical. A proper solution may be to highly extend the acquisition time, despite of the system real-time warning generation reliability, that may become no more suitable for the desired purposes. Consequently, a good starting point for a successive possible work could be an analysis of a real mountain scenario through the simulations of events roughly similar to real rockfalls or debris flow.

Overall, the analysis performed returned excellent results in term of reliability and cost-effectiveness. In addition, the OFSs technology is a research field in constant expansion and full of unexplored scenarios, therefore I think that the outcomes obtained in this Thesis may be still greatly improved, with the target of developing a low-cost system able to correctly map the spatial distribution of the sensed measurand along the fiber, bringing benefits to all the people which life is constantly jeopardized by unexpected and threatening geotechnical events in a mountain environment.

Appendix A

PP SOPAS evaluation

Appendix B

RT SOPAS evaluation

Appendix C

Real Time Algorithm: Matlab Script

```
1 clear;
2 close all;
3 clc;
4
5 addpath('Utilities\');
6 addpath('Utilities\COM\');
7 addpath('Utilities\MEX\');
8 addpath('Utilities\MEX_2\');
9
10 addpath('..\2x1 switch post-processing\Scripts');
11
12 % Real time reading is performed through one by one address reading, but
13 % one single if
14
15 %% Polarimeter set-up
16 %PM1000_2 -> USB 3.0
17 %PM1000 -> USB 2.0
18
19 % PM = PM1000_2;
20 PM = PM1000;
21 % PM.close;
22
23 % make sure these two connect to two different PM1000, fw>=1083:
24 PM.init;
25
26 % Setup
27 PM_OFF=512; %PM offset
28 S1_OFF=25; % polarimeter registers
29 S2_OFF=26;
30 S3_OFF=27;
31
32 %% NI_cDAQ_9178_Control2022
```

```

33 daqDgt = daq("ni");
34 chs = addoutput(daqDgt, "cDAQ1Mod5", "Port0/Line0:7", "Digital");
35 daqDgt.Channels;
36
37 pins1 = [0 1 1 0 0 0 0 0]; % P1
38 % pins2 = [1 0 0 1 0 0 0 0]; % P2
39 pins3 = [0 1 0 1 0 0 0 0]; % P3
40 % pins4 = [1 0 1 0 0 0 0 0]; % P4
41 % pins_res= [0 0 0 0 0 0 0 0]; % Reset
42 pins_vect=[pins1;pins3];
43 write(daqDgt, pins1);
44
45 %% Plots Initialization
46 % figure;
47 % h(1) = animatedline('Marker', '.', 'LineStyle', 'none', 'MarkerSize', 12);
48 % h(1).Color = 'red';
49 % % title(['SOP angular speed evolution of fiber A - T_{mov} = ',
50 %         num2str(Tmov), 's']);
51 %
52 % % figure(2);
53 % h(2) = animatedline('Marker', '.', 'LineStyle', 'none', 'MarkerSize', 12);
54 % h(2).Color = 'black';
55 % xlabel('time [s]');
56 % ylabel('SOP angular speed [rad/s]');
57 % grid on;
58
59 %% Parameters
60 Tmov_samples=20; % samples of moving average
61 N=1e3; % number of commutations of the switch per simulation
62 N_rep=10; % define how many simulations we will perform, it is
63 % needed for long acquisitions
64 t=0;
65 time=NaN(1,N); % vector of switching periods
66 alarm=0; % alarm counter
67 started=0; % start moving average flag, becomes to 1 when buffer is
68 % filled
69 th=1; % SOPAS threshold to get an alarm
70 N_fibers=2; % # of fibers tested
71 dt=0.01*N_fibers;
72 Timer1=0; % timer for FALSE ALARMS
73 S=NaN(3,N); % vector of the stokes parameters (does not save S0)
74 angle_smoothed=zeros(1,N); % vector of useful SOPAS
75 buffer=NaN(1,Tmov_samples); % buffer containing the moving average
76 buff=NaN(1,100); % buffer pre-detection, needed to add some noise
77 % to the SOPAS saved and enhance the accuracy of the correlaion
78 stop=0; % flag that defines when we stop the acquisition, it
79 % turn to one when 2 alarms has been acquired
80 A=[]; %needed to save the SOPAS every time we overwrite his
81 % vector to not fill the MATLAB memory
82
83 %% Sopas Computation
84 t0=tic;
85 for j=1:N_rep

```

```

80 % if j>1, the S parameters will be stored from index 1+N_fibers, so
    S will always have the previous samples
81 if j==1
82     k=0;
83 else
84     k=N_fibers;
85 end
86 for n=1+k:N
87     t1=tic;
88     S(1,n)=(PM1000.read(PM_OFF+S1_OFF)-2^15)/2^15;
89     S(2,n)=(PM1000.read(PM_OFF+S2_OFF)-2^15)/2^15;
90     S(3,n)=(PM1000.read(PM_OFF+S3_OFF)-2^15)/2^15;
91 %     S(:,n) = PM1000.getStokes(1);
92     if n > N_fibers
93         angle = acos((dot(S(1,n), S(1,n - N_fibers))+ dot(S(2,n)
, S(2,n - N_fibers)) + dot(S(3,n), S(3,n - N_fibers)))/dot(sqrt(S
(1,n)^2 + S(2,n)^2 + S(3,n)^2), sqrt(S(1,n - N_fibers)^2 + S(2,n -
N_fibers)^2 + S(3,n - N_fibers)^2)));
94         angle = angle/dt;
95         if (n == N_fibers*Tmov_samples+1) && (started == 0)
96             buffer(n-N_fibers) = abs(angle);
97             %moving average can start
98             smoothed_out = sum(buffer(1:N_fibers:end))/
Tmov_samples;
99             started = 1;
100            time_offset = toc(t0);
101            buff=circshift(buff,-1);
102            buff(end)= smoothed_out;
103         elseif (started == 0)
104             %still not reached Tmov_samples. Moving average FIR
cannot start
105             buffer(n-N_fibers) = abs(angle);
106             buff=circshift(buff,-1);
107             buff(end)= abs(angle);
108         elseif (started == 1)
109             %moving average is started in continuous time
110             buffer(:) = circshift(buffer(:), -1); % Shift
positions of elements circularly.
111             buffer(end) = abs(angle);
112             smoothed_out = sum(buffer(1:N_fibers:end))/
Tmov_samples;
113             if (alarm==0)
114                 buff=circshift(buff,-1);
115                 buff(end)=smoothed_out;
116                 if (smoothed_out > th)
117                     alarm=alarm+1;
118                     angle_smoothed(n) = smoothed_out;
119                     T1=tic;
120                     ind1=mod(n,2);
121                 end
122             elseif (alarm == 1)
123                 angle_smoothed(n) = smoothed_out;
124                 Timer1=toc(T1);

```

```

125         if (Timer1 > 10) && (alarm==1)
126             alarm=0;
127             disp('-----False Alarm Detected!');
128             angle_smoothed=zeros(1,N);           %
reset angle_smoothed and A
129             A=[];
130             Timer1=0;
131             elseif (smoothed_out > th) && (mod(n,2)~=
ind1) % mod(n,2)=ind2
132                 ind2=mod(n,2);
133                 alarm=alarm+1;
134             end
135             elseif (alarm==2)
136 %                 if (smoothed_out < th) && (mod(n,2)==ind2)
137                     angle_smoothed(n) = smoothed_out;
138                     [angle_smoothed,n]=
ContinuousAcquisitionFunc_RT_v2(n,S,angle_smoothed,N_fibers,dt,
PM1000,daqDgt,pins_vect,buffer,Tmov_samples);
139                     stop=1;
140                     break;
141 %                 else
142 %                     angle_smoothed(n) = abs(angle);
143 %                 end
144             end
145         end
146     end
147     ind=mod(n,2)+1; % identify which fiber we will acquire
148     pins=pins_vect(ind,:);
149     write(daqDgt, pins);
150     pauses(0.002);
151     time(n)=toc(t1);
152     end
153     S=circshift(S,N_fibers,2); % move to the right the columns of S of
N_fibers steps.
154     A=[A angle_smoothed(angle_smoothed>0)]; % fill A in order to
save angle_smoothed and overwrite it.
155     angle_smoothed=zeros(1,N); % clear angle smoothed and overwrite
it.
156     if (stop==1) && (N_rep>1)
157         break;
158     end
159 end
160
161 PM.close;
162 daqreset;
163
164 % A=[A angle_smoothed(angle_smoothed>0)];
165 angle_smoothed=[buff(1:end-1) A];
166 SOPASfbA = angle_smoothed(1:2:end);
167 SOPASfbB = angle_smoothed(2:2:end);
168
169 if alarm == 2
170     %% Plots

```

```

171 figure;
172 plot((SOPASfbB-mean(SOPASfbB))/max(SOPASfbB),'b','LineWidth',2);
173 hold on;
174 plot((SOPASfbA-mean(SOPASfbA))/max(SOPASfbA),'r','LineWidth',2);
175 xlabel("Samples");
176 ylabel("SOPAS [rad/s]");
177 legend("SOPAS_A", "SOPAS_B");
178 grid on;
179
180 %% Correlations
181 R=xcorr((SOPASfbB-mean(SOPASfbB))/max(SOPASfbB),(SOPASfbA-mean(
SOPASfbA))/max(SOPASfbA));
182 axisR=(-length(R)/2:length(R)/2-1)*2*dt;
183 figure;plot(axisR,R);
184 hold on;
185
186 %% Center of mass
187 locs=find(R>max(R)/3);
188 xc = trapz(axisR(locs),axisR(locs).*R(locs)) ./ trapz(axisR(locs),R(
locs));
189 yc = trapz(R(locs),axisR(locs).*R(locs)) ./ trapz(R(locs),axisR(locs
));
190
191 plot(xc,yc,'r*','LineWidth',2)
192 xline(xc,'--r');
193 ylabel("R(\tau)");
194 xlabel("\tau [s]");
195 grid on;
196
197 ramp_length=3; % [m]
198 Rock_Speed=ramp_length/abs(xc); % [m/s]
199
200 disp(sprintf('\n-----The fiber delay is: %f s',abs(xc)));
201 disp(sprintf('\n-----The Rock Speed is: %f m/s',Rock_Speed));
202 else
203
204     disp(sprintf('\n-----No second alarm detected'));
205
206 end
207
208 figure;
209 hold on;
210 plot(1:length(time),time);
211 xlabel('Commutations');ylabel('Time on each fiber [s]');
212 legend(['Tmov=',num2str(time_offset/N_fibers),' s']);
213 grid on;
214 mean(time(~isnan(time(100:end))))
215 std(time(~isnan(time(100:end))))

```

```

1 function [angle_smoothed,n]=ContinuousAcquisitionFunc_RT_v2(n,S,
   angle_smoothed,N_fibers,dt,PM1000_2,daqDgt,pins_vect,buffer,
   Tmov_samples)
2
3 % same as ContinuousAcquisitionFunc_RT, but perform the moving average
4 T=0;
5 t=tic;
6 while ((T<3) && (n<=length(S)))
7     ind=mod(n,2)+1; % identify which fiber we are acquiring
8     pins=pins_vect(ind,:);
9     write(daqDgt, pins);
10    pauses(0.002);
11    n=n+1;
12    S(1,n)=(PM1000_2.read(512+25)-2^15)/2^15;
13    S(2,n)=(PM1000_2.read(512+26)-2^15)/2^15;
14    S(3,n)=(PM1000_2.read(512+27)-2^15)/2^15;
15    angle = acos((dot(S(1,n), S(1,n - N_fibers))+ dot(S(2,n), S(2,n -
   N_fibers)) + dot(S(3,n), S(3,n - N_fibers)))/dot(sqrt(S(1,n)^2 + S
   (2,n)^2 + S(3,n)^2), sqrt(S(1,n - N_fibers)^2 + S(2,n - N_fibers)^2
   + S(3,n - N_fibers)^2)));
16    angle = angle/dt;
17    buffer(:) = circshift(buffer(:), -1); % Shift positions of elements
   circularly.
18    buffer(end) = abs(angle);
19    smoothed_out = sum(buffer(1:N_fibers:end))/Tmov_samples;
20    angle_smoothed(n) = smoothed_out;
21    T=toc(t);
22 end

```

Bibliography

- [1] Mauro Boreggio, Martino Bernard, and Carlo Gregoretti. «Evaluating the Differences of Gridding Techniques for Digital Elevation Models Generation and Their Influence on the Modeling of Stony Debris Flows Routing: A Case Study From Rovina di Cancia Basin (North-Eastern Italian Alps)». In: *Frontiers in Earth Science* 6 (2018). ISSN: 2296-6463. DOI: [10.3389/feart.2018.00089](https://doi.org/10.3389/feart.2018.00089). URL: <https://www.frontiersin.org/articles/10.3389/feart.2018.00089>.
- [2] Rudi Bratovich et al. «Surveillance of Metropolitan Anthropogenic Activities by WDM 10G Optical Data Channels». In: *2022 European Conference on Optical Communication (ECOC)*. 2022, pp. 1–4.
- [3] Mattia Cantono et al. «Optical Network Sensing: Opportunities and Challenges». In: *2022 Optical Fiber Communications Conference and Exhibition (OFC)*. 2022, pp. 1–3.
- [4] Po-Chun Chen et al. «Measurement of linear birefringence and diattenuation properties of optical samples using polarimeter and Stokes parameters». In: *Opt. Express* 17.18 (Aug. 2009), pp. 15860–15884. DOI: [10.1364/OE.17.015860](https://doi.org/10.1364/OE.17.015860). URL: <https://opg.optica.org/oe/abstract.cfm?URI=oe-17-18-15860>.
- [5] Zhenyang Ding et al. «Distributed measurements of external force induced local birefringence in spun highly birefringent optical fibers using polarimetric OFDR». In: *Opt. Express* 27.2 (Jan. 2019), pp. 951–964. DOI: [10.1364/OE.27.000951](https://doi.org/10.1364/OE.27.000951). URL: <https://opg.optica.org/oe/abstract.cfm?URI=oe-27-2-951>.
- [6] FOSCO. *Stokes Polarization Parameters*. 2012. URL: <https://www.fiberoptics4sale.com/blogs/wave-optics/102492742-stokes-polarization-parameters>.
- [7] FOSCO. *Whar is birefringence and beat length?* 2012. URL: <https://www.fiberoptics4sale.com/blogs/wave-optics/102492742-stokes-polarization-parameters>.
- [8] A.H. Hartog. *An Introduction to Distributed Optical Fibre Sensors*. Series in Fiber Optic Sensors. CRC Press, 2017. ISBN: 9781351645300. URL: <https://books.google.it/books?id=7TY1DwAAQBAJ>.
- [9] Guangyao Liu. «Polarization waves». In: *University of California* (2021). URL: [https://batch.libretexts.org/print/url=https://eng.libretexts.org/Bookshelves/Materials_Science/Supplemental_Modules_\(Materials_Science\)/Optical_Properties/Polarization_of_Waves.pdf](https://batch.libretexts.org/print/url=https://eng.libretexts.org/Bookshelves/Materials_Science/Supplemental_Modules_(Materials_Science)/Optical_Properties/Polarization_of_Waves.pdf).

- [10] Antonio Mecozzi et al. «Polarization sensing using submarine optical cables». In: *Optica* 8.6 (June 2021), pp. 788–795. DOI: [10.1364/OPTICA.424307](https://doi.org/10.1364/OPTICA.424307). URL: <https://opg.optica.org/optica/abstract.cfm?URI=optica-8-6-788>.
- [11] Novoptel. *PM1000 Polarimeter*. Novoptel, 2011. URL: https://www.novoptel.de/Polarimeter/Polarimeter_PM1000_en.php.
- [12] Rüdiger Paschotta. «Polarization-maintaining fibers». In: *RP Photonics Encyclopedia* 1. edition (Oct. 2008). URL: https://www.rp-photonics.com/polarization_maintaining_fibers.html.
- [13] S. Pellegrini. «Landslide monitoring using optical fiber sensing based on polarization». Politecnico di Torino, Apr. 2022.
- [14] Peiliang Qi et al. «Simultaneously characterized Stokes parameters of a lightwave utilizing the tensor polarization holography theory». In: *Opt. Express* 30.26 (Dec. 2022), pp. 47264–47279. DOI: [10.1364/OE.472855](https://doi.org/10.1364/OE.472855). URL: <https://opg.optica.org/oe/abstract.cfm?URI=oe-30-26-47264>.
- [15] Simon Ramo. *Fields and Waves in Communication Electronics*. Ed. by Jhon Wiley. 3rd ed. 1994. ISBN: 978-0-471-58551-0.
- [16] Marcelo A. Soto et al. «Distributed phase birefringence measurements based on polarization correlation in phase-sensitive optical time-domain reflectometers». In: *Opt. Express* 23.19 (Sept. 2015), pp. 24923–24936. DOI: [10.1364/OE.23.024923](https://doi.org/10.1364/OE.23.024923). URL: <https://opg.optica.org/oe/abstract.cfm?URI=oe-23-19-24923>.
- [17] SAMM Teknologi. *What is Optical Switching?* Mar. 2021. URL: <https://telecom.samm.com/optical-switching>.
- [18] Wei Wang et al. «Poincaré sphere representation for the anisotropy of phase singularities and its applications to optical vortex metrology for fluid mechanical analysis». In: *Opt. Express* 15.17 (Aug. 2007), pp. 11008–11019. DOI: [10.1364/OE.15.011008](https://doi.org/10.1364/OE.15.011008). URL: <https://opg.optica.org/oe/abstract.cfm?URI=oe-15-17-11008>.